Color Propagation in Cold and Hot Matter

Jorge Andrés López López

Tesis para optar al grado de Doctor en Ciencias mención Física
Universidad Técnica Federico Santa María

Abstract

The propagation of color traversing the nuclear medium is studied in medium energy semi-inclusive deep inelastic scattering in nuclei and in high energy lead-lead collisions, using existing published HERMES data and performing a measurement with the ATLAS detector at the LHC respectively. Different aspects are analyzed. In the first part two related observables are combined and modeled using a new geometric model that describes both simultaneously. The model provides information on the transport coefficient and the color lifetime or production length in the cold medium produced in electron-nucleus scattering at medium energies. In the second part the measurement of the prompt and non-prompt J/ψ elliptic flow coefficient in lead-lead collisions with the ATLAS detector at the LHC is performed. This coefficient is an excellent observable linked to the color lifetime of charm and bottom quarks, probed by measuring the prompt and non-prompt J/ψ, in the hot dense medium created in high energy nucleus-nucleus collisions.

Declaration

This dissertation is the result of my own work, except where explicit reference is made to the work of others, and has not been submitted for another qualification to this or any other university.

Jorge Andrés López López

Acknowledgements

Of the many people who deserve thanks, some are particularly prominent, such as my supervisor, my family, friends and colleagues.

Without the support of Will Brooks this work would have not been possible nor my personal development as a scientist.

Contents

List of figures

List of tables

"Writing in English is the most ingenious torture ever devised for sins committed in previous lives."

— James Joyce

Chapter 1.

Space-time Analysis of siDIS on Nuclei

1.1. Introduction

Data from the highest energy scattering achieved to date continue to be successfully described by perturbative Quantum Chromo Dynamics (pQCD) [1]. The ideas of asymptotic freedom [2, 3] and factorization to separate hard processes from soft processes [4] have permitted calculations in next-to-next-to-leading order pQCD that provide agreement to high precision for numerous hard processes in TeV-scale proton-proton collisions. This is an impressive scientific success resulting from six decades of experimental and theoretical work. Further, theoretical and experimental advances in some parts of the soft sector have produced striking progress in such diverse areas as lattice QCD[5, 6], anti-de Sitter QCD correspondence [7, 8], effective field theory [9, 10], and two-particle correlations in collisions of hadronic systems [11, 12]. Over the next decade, breakthrough progress is expected in key areas such as understanding quark confinement in QCD [13].

A crucially important soft process which has seen little progress in quantitative dynamical understanding since the development of the Lund string model in the 1970's is that of hadronization, or quark fragmentation, despite the fact that this process occurs in every high-energy interaction producing hadronic final states. The hadronization process performs the dynamical enforcement of quark confinement, revealing the dynamical origins of this most fundamental property of QCD [14]. Now, prospects for new breakthroughs in our understanding of hadronization are much brighter due to the influx of new data on semi-inclusive deep inelastic scattering on nuclei (nSIDIS) with identified hadrons in the final state. As will be explained in the following, such data are uniquely suited to studies of hadronization dynamics.

In this section we analyze data taken by the HERMES Collaboration, the first-ever nSIDIS data having identified final-state hadrons [15, 16, 17]. We use a unique new approach that combines two related observables, the ***transverse momentum broadening*** and the ***hadron multiplicity ratio***, to estimate the ***color lifetime*** or ***production length*** by comparing data from nuclei of different sizes. We define color lifetime as the duration of time over which a propagating object persists in a color octet state. We explore the feasibility of extending the conclusions of this analysis beyond the struck quark to other quarks produced in the interaction. While we are aware of the potential connections of these studies to the hot matter formed in heavy ion

collisions, this work focuses only on fundamental processes in the cold matter of atomic nuclei at high x_{Bj}, and their extrapolation to the processes in vacuum.

Unlike the pQCD calculation of cross-sections as described above, the computation of observables related to the propagation of a quark or gluon through a strongly interacting medium is not yet at the stage of precise comparison to data. These studies contain elements of long-distance physics for which approximations limit the final precision, although much progress has been made. A number of reviews have appeared over the past fifteen years [18, 19, 20, 21]. Important quantities which appear in these studies include the transport coefficients $\hat{q}$ and $\hat{e}$, which relate to the transverse momentum broadening and the longitudinal energy loss of quarks and gluons in the system. Especially at lower energies, but also at higher energies, the lifetime of the propagating colored quark or gluon must be considered in order to make quantitative estimates of the transport coefficients and other relevant quantities.

Our model emphasizes geometric constraints and uses minimal dynamical assumptions, by design. The dynamical behavior, such as the unknown dependence of the color lifetime on the parameter $z_{\mathrm{h}} \equiv E_{\mathrm{h}}/\nu$ (where E_{h} is the energy of the hadron formed and ν is the energy transfer), is not prescribed by our model but rather emerges from the behavior of the fit in the various kinematic bins for three different nuclei. The model primarily consists of geometric elements. It uses the known density distributions of atomic nuclei to extract geometrical information on the color lifetime or production length, on the $\hat{q}$ transport coefficient, and on the ***pre-hadron*** inelastic interaction cross section in the medium. It also provides approximate information on the longitudinal energy loss, which is related to the $\hat{e}$ transport coefficient. These elements are discussed in more detail below. The aim of this work is to extract basic features of the interaction, while paving the way for more sophisticated theoretical calculations that will follow.

1.2. Space-time Picture of siDIS on Nuclei

It is sometimes asserted that the path-length traveled by the struck quark in a nuclear siDIS interaction is longer than the dimensions of any nucleus at sufficiently high energies [22]. This assumption is not strictly justified for all kinematic conditions, even at the highest energies.

In a simple approximation and for the struck quark case only, it is possible to derive an explicit formula for the production length from the Lund string model [23]as a function of z_{h} and other kinematic variables:

$$L_{\mathrm{p}}(z_{\mathrm{h}}, Q^2, \nu) = \frac{1}{2\kappa}\left(M_p + \nu\left(1 + \sqrt{\nu^2 + Q^2}\right) - 2\nu z_{\mathrm{h}}\right) \tag{1.1}$$

where κ is the string constant and M_p is the proton mass (see Appendix A.1 for an explicit derivation). In a more general extension which includes higher rank hadrons, Bialas *et al.* [24]

predicts:

$$L_{\mathrm{p}}(z_{\mathrm{h}}) \propto z_{\mathrm{h}} \frac{\log\left(1/z_{\mathrm{h}}^2\right) - 1 + z_{\mathrm{h}}^2}{1 - z_{\mathrm{h}}^2} \tag{1.2}$$

The $z_{\mathrm{h}} \to 1$ limit may be heuristically thought of as a consequence of energy conservation [**Boris**], since no gluons could have been emitted by a quark that carries 100% of the available energy, thus the hadron is formed very rapidly on average, and the color lifetime vanishes. The physical significance of the pathlength vanishing is that the entity interacting with the nucleus in that case is not partonic, *i.e.*, parton-level interactions cannot be responsible for the phenomena at the $z_{\mathrm{h}} \to 1$ limit, and by extension, the role played by parton-level interactions must decrease as this limit is approached. It should be noted that the behavior at high z_{h} mentioned above is reproduced in modeling of HERMES data and EMC data in the GiBUU model [25], that is, at high z_{h} there is a measure of hadron attenuation predicted even at EMC energies.

Although the string model is a classical model that does not contain explicit gluons, it builds in this behavior. The function shown in Eq. 1.1 is not used in our analysis, however, this function can be compared with what we derive from the HERMES data using our model; as will be shown in the following, we observe a behavior which is consistent with this function.

The path-length in the nuclear medium can be estimated experimentally using semi-inclusive nuclear DIS given the assumptions noted below.

1.2.1. Kinematic considerations

In the following we make the approximation of neglecting two-photon exchange [26] and higher-order processes, thus, a single virtual photon is emitted by the scattered lepton. In SIDIS for $x_{\mathrm{Bj}} > 0.1$, the process of quark pair production by the virtual photon is negligible [27]. Thus, the full energy and momentum of this virtual photon is absorbed by one valence quark. Because the energy and momentum of the virtual photon are measured using the scattered lepton, the quark's initial conditions are well known; this is a unique and powerful condition resulting from the use of electron scattering in specific kinematic conditions.

A virtual photon with an energy $E_\gamma = \nu \approx 10$ GeV has a lifetime of $1/E_\gamma \approx 0.02$ fm/c and thus it probes a longitudinal distance of ≈ 0.02 fm. If this virtual photon has a momentum $p_\gamma \approx 10$ GeV/c, it will similarly have a wavelength of ≈ 0.02 fm and thus can probe transverse areas of $\approx (0.02\ \mathrm{fm})^2$. Therefore, even allowing for additional factors of π, $\hbar$, etc., the fraction of the volume of the nucleon probed by such virtual photons is of the order of $10 - 100$ parts per million, and the interaction is point-like on the scale of nuclear dimensions. These considerations ensure that the hard interaction occurs at a very well-defined point within the nuclear volume for each event, without the complications of initial-state interactions that are present in, for example, hadron-beam scattering. This picture is implicitly assumed in our approach.

For a particle of mass m, momentum $\vec{p}$ and energy E:

$$m^2 = E^2 - p^2 \tag{1.3}$$

If the virtual photon has a four-momentum transfer of $Q = (\nu, \vec{q})$ then:

$$Q^2 = \nu^2 - q^2 \tag{1.4}$$

Thus, heuristically, and within the approximations given in the above paragraph, the virtual photon is identified as a particle with momentum q and energy ν. The struck valence quark immediately after the hard interaction thus has momentum q, energy ν, and mass $m_\gamma \equiv \sqrt{Q^2}$, neglecting its intrinsic momentum and mass. For quarks in a nucleus we also neglect Fermi momentum.

This allows the derivation of the initial velocity β and Lorentz factor γ of the struck quark as:

$$\beta \equiv \frac{q}{\nu} = \frac{\sqrt{\nu^2 - Q^2}}{\nu} \tag{1.5}$$

$$\gamma \equiv \frac{\nu}{m_\gamma} = \frac{\nu}{\sqrt{Q^2}} \tag{1.6}$$

These factors will be used later to extrapolate our results to the energies of other experiments.

1.2.2. Definition of characteristic times and lengths

We consider the struck quark moving away from the initial interaction point, traveling as a colored object that emits gluons, as in the perturbative picture of the process. After propagating a particular distance, a color singlet system forms from the struck quark and (in the case of a produced meson) an antiquark, where this $q\overline{q}$ pair is ultimately contained in the final-state meson. An additional concept is needed here, the ***pre-hadron***. This concept is inescapable since there is no reason that the color singlet should in general be instantly formed with the final state mass of a hadron. A system of size 1 fm should minimally require a time of the order of 1 fm/c to form in its rest frame, and longer if it is boosted to the lab frame. Thus, the ***formation length*** is non-zero, and the pre-hadron is able to interact with hadrons as it is forming, presumably with a reduced cross section.

We define one more length for convenience: the ***hadronic length***, as the path-length in the medium of the pre-hadron or hadron. This has no fundamental physics meaning, but it will facilitate the description of the model in the following text.

To reiterate the the foundational idea of the above space-time picture, we divide the process into two stages, which are equally valid in the vacuum process and in-medium. The first stage, of a propagating colored quark emitting gluons, is intuitively familiar from the analogous process in Quantum Electro-Dynamics (QED) of a struck charged electron emitting photons in the process

of rebuilding its truncated electric field [**Landau or Dokshitzer or Feynman**]. The second stage, the formation of the pre-hadron, is defined by the formation of a color singlet system that no longer emits gluons. The pre-hadron is a hadron in formation, and thus its mass and size may be different from the hadron that is eventually formed. In general the same description applies to color dipoles and to color-charged fragments from the target fragmentation kinematics.

Beyond the struck valence quark, there are other quarks and anti-quarks produced in the hadronization process. In the above picture, these higher-rank quarks and anti-quarks behave in the same way, but with a reduced color length on average, since their origination point is separated from the hard scattering point by some distance. Further, there are quarks and anti-quarks related to the residual system in the target fragmentation kinematics. Hadrons with $z_h > 0.5$ are expected to have a substantially higher probability of containing the struck quark, while hadrons with $z_h < 0.5$ are expected to be increasingly dominated by target fragmentation kinematics [**Berger ref?**]. This qualitatively predicts a decrease in color path-length for the lowest z values in the vacuum process which are dominated by target fragmentation.

We define the production length L_p as the distance needed to produce the color singlet system. The color lifetime τ_c is the this length divided by the average velocity of the quark. We define the formation length L_f as the additional distance required for the meson to completely form, *i.e.*, to attain its full mass, and the corresponding time as τ_f. With these definitions, the total time required to produce a fully formed meson starting from the hard interaction is $\tau_c + \tau_f$. In this work we are measuring L_p, and from it we can infer τ_c. We do not address τ_f; it is only mentioned here for clarity, since some authors use different conventions for these terms. A diagram sketching the deep-inelastic scattering process together with the corresponding length scales is shown in Fig. 1.1.

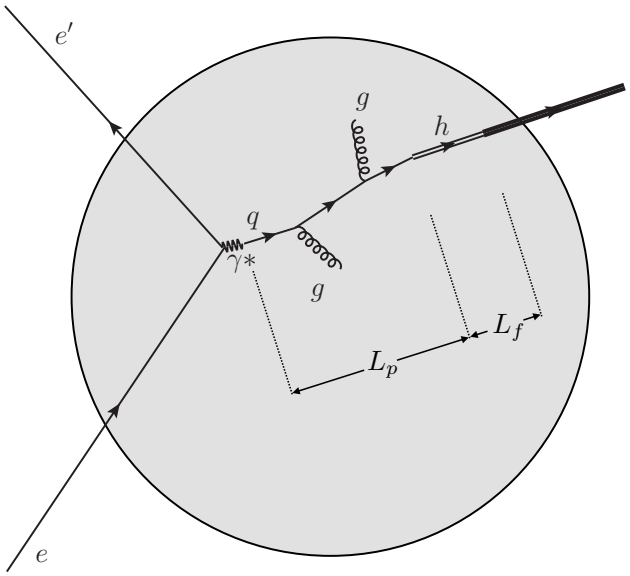

Figure 1.1.: A schematic diagram of the nSIDIS process illustrating the production length L_p and formation length L_f. At the energies considered in this work the longitudinal and transverse extents of the virtual photon are much less than 0.1 fm, therefore, those features of this diagram are not drawn to scale.

1.2.3. Process modifications due to the nuclear medium

In the nuclear medium, the above process has two additional features. First, the propagating object can interact elastically with the constituents of the medium, stimulating radiative energy loss through additional gluon emission, and inducing a small amount of collisional energy loss. This has the effect of reducing the quark energy, and broadening the transverse momentum distribution of the quark. As a consequence, the transverse momentum distribution of the produced hadron is also slightly broader, and the produced hadron has slightly less energy due to this partonic-level interaction with the medium.

The second feature due to the medium is that the produced pre-hadron can interact elastically and inelastically with the constituents of the medium. Because the local hadronic field of the pre-hadron is in formation, it can be supposed that its interaction cross section is smaller than that of the hadron that is ultimately formed. At the hadron energies relevant to this study, the inelastic cross section is much larger than the elastic scattering cross section and thus the main effect from the medium is for the pre-hadron to interact inelastically, producing more hadrons of lower energies than would be observed in the vacuum process. In terms of the z_h variable defined above, these hadrons tend to emerge at much lower z_h. In the vacuum process at the energies considered here, on average only a few hadrons are produced in a given event; an inelastic interaction with the nuclear medium typically produces a hadronic cascade [do we want a reference here? or intra-nuclear cascade?], thus on average the original value of z_h will be reduced by a factor of a few, shifting the spectrum to much lower z_h values for events where these interactions occur.

1.3. Experimental Observables

Two experimental observables are used simultaneously in this study: the transverse momentum broadening and the multiplicity ratio. The transverse momentum broadening experimental observable is defined as the shift in the mean value of the fully-corrected transverse momentum distribution of measured hadrons in a larger nucleus A relative to a smaller nucleus p:

$$\Delta p_T^2(Q^2, \nu, z_h) \equiv \left\langle p_T^2(Q^2, \nu, z_h) \right\rangle \Big|_A - \left\langle p_T^2(Q^2, \nu, z_h) \right\rangle \Big|_p \tag{1.7}$$

Unlike transverse momentum in collider kinematics, the transverse direction here is defined as being perpendicular to the virtual photon direction, not to the beam axis. This observable is sensitive to the parton level multiple scattering discussed above. This experimental observable is related to the quark-level broadening, Δk_T^2, which is not directly observable, but which by heuristic geometrical arguments is approximately given by:

$$\Delta p_T^2 \approx \Delta k_T^2 \cdot z_h^2 \tag{1.8}$$

In pQCD-based dipole models at high energy [**Mueller**, **others**], Δk_{T}^2 is proportional to the quark path-length L in the medium, with logarithmic corrections:

$$\Delta k_T^2 = \hat{q} L \left(1 + \frac{\alpha_{\mathrm{S}} N_{\mathrm{C}}}{8\pi} \log^2\left(\frac{L^2}{l_0^2}\right) + \ldots\right) \tag{1.9}$$

In Eq. 1.9, α_{S} is the strong coupling constant, N_{C} is the number of QCD colors, and l_0 characterizes the distance between scatters in the medium. Neglecting the logarithmic corrections, Δk_T^2 is proportional to the total radiative energy loss of a quark passing through a medium:

$$-\Delta E_q = \frac{\alpha_{\mathrm{S}}}{4} \Delta k_T^2 \cdot L = \frac{\alpha_{\mathrm{S}}}{4} \hat{q} \cdot L^2 \tag{1.10}$$

In the latter equation we have used the relation:

$$\Delta k_T^2 = \hat{q} L \tag{1.11}$$

The above equation solely concerns quantities related to the quark. However, for convenience we also define an analogous quantity, $\hat{q}_{\mathrm{h}}$, that mixes the hadron broadening with the quark path-length, because this quantity can be computed with less model dependence.

$$\Delta p_{\mathrm{T}}^2 = \hat{q}_{\mathrm{h}} L \approx \hat{q} L z_{\mathrm{h}}^2 \tag{1.12}$$

It should be carefully noted that the only experimental observable in the above Eqs. 1.8 - 1.12 is Δp_T^2. The other quantities Δk_T^2 and ΔE are connected to this observable through model approximations. In this work we do not use Eqs. 1.8-1.12. They are included here for context and to make clear which approximations are being employed, as discussed further below.

The second experimental observable, the hadronic multiplicity ratio, is defined as follows:

$$R_{\mathrm{M}}(Q^2, \nu, z_{\mathrm{h}}, p_T) \equiv \frac{N_{\mathrm{h}}(Q^2, \nu, z_{\mathrm{h}}, p_{\mathrm{T}}) \Big/ N_e(Q^2, \nu)\Big|_A}{N_{\mathrm{h}}(Q^2, \nu, z_{\mathrm{h}}, p_{\mathrm{T}}) \Big/ N_e(Q^2, \nu)\Big|_p} \tag{1.13}$$

This observable is equal to unity in the absence of all nuclear effects. In the pion data used in this study, R_{M} is generally less than unity, *i.e.*, suppression of hadron production is observed, however, in data for other hadrons measured by HERMES, both suppression and enhancement were observed.

1.4. Treatment of data

The number of z_{h} bins for the published HERMES data for the multiplicity ratio is different from the number of z_{h} bins in their p_{T} broadening data. Therefore, an interpolation was performed

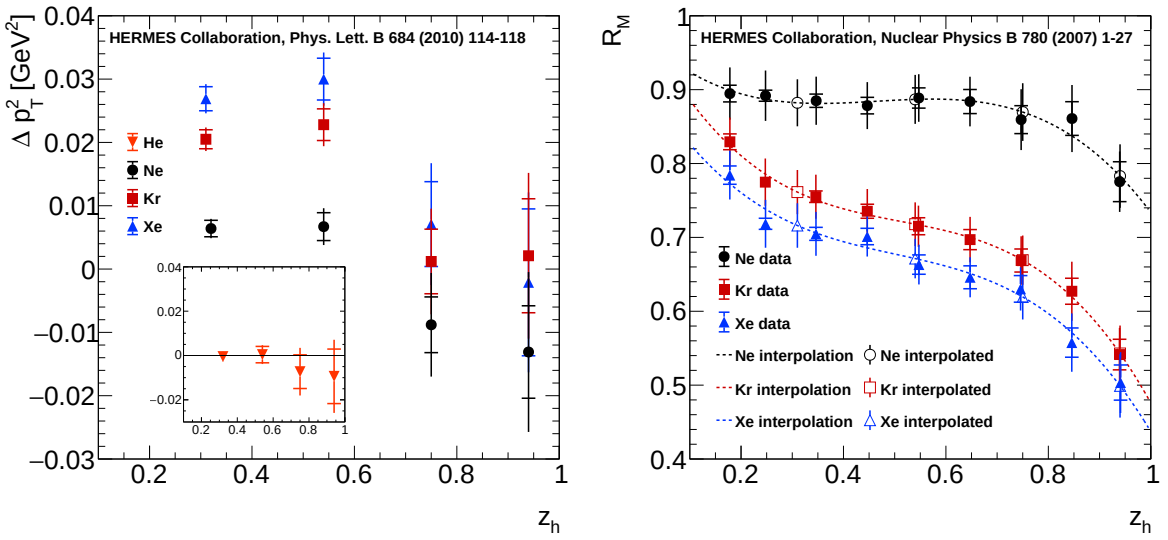

Figure 1.2.: Plots of the HERMES data for Δp_T^2 (left) and the multiplicity ratio (right) for positive pions. The lower panel also shows the interpolations used to match the multiplicity ratio binning to the binning shown in the upper panel. The average kinematic cuts for the transverse momentum broadening are $10.6 < \nu < 14.2$ GeV and $2.2 < Q^2 < 2.4$ GeV^2, whereas for the multiplicity ratio is in the range $11 < \nu < 14$ GeV.

of the multiplicity ratio as a function of z_h in order to obtain the values at the bins needed to compare to the p_T broadening data. The interpolation was performed using a third-order polynomial and the total uncertainties of the data points. The uncertainties of the interpolated data points were obtained using the same strategy, by using the same third-order polynomial, but fitting the centroids shifted up and down by their total uncertainties. The final interpolated uncertainty is compatible with the 99% confidence level interval of the first fit to the centroids of the data. A plot showing this interpolation is shown in Fig. 1.2.

One difficulty in using the HERMES data for deuterium as the reference nucleus for p_T broadening is that the centroid values for several nuclei at higher z_h are negative, although within the uncertainties they are consistent with zero and with small positive values. We observed that the same was true for the helium data from HERMES, which is shown in the inset in the upper panel of Fig. 1.2. In the model we are using it is not possible to generate negative values of p_T broadening. We used two methods to address this problem. First, we tried setting the negative centroid values to zero. This resulted in fits of good quality, but we found that this choice might underestimate the final uncertainties. Second, we took the helium data as being a baseline for the deuterium measurements and subtracted the helium centroids from the deuterium centroids. While this has the deleterious effect of increasing the experimental uncertainties, it has the positive effect that no arbitrary assignment to zero was required, and that in principle it removes a systematic shift to negative values that is unphysical in the terms of our model. We analyzed the data under the assumption of several different degrees of correlation between the deuterium uncertainties and the helium uncertainties for p_T broadening, and found the fit results were not sensitive to this correlation.

1.5. Model approach

1.5.1. Model description

The model used in this work contains parameters that are determined by a simultaneous fit to the HERMES data for transverse momentum broadening and multiplicity ratio in four bins in z_h, integrated over all other variables, for the nuclei neon, krypton, and xenon, using a combination of helium and deuterium as a baseline as described below. The baseline model (BL) has three parameters: the mean production length L_p, an effective hadronic interaction cross section σ, and a parameter q_0 related to the $\hat{q}$ transport coefficient. We also explored variants of the model, such as (1) incorporation of quark energy loss, (2) incorporation of the logarithmic corrections seen in Eq. 1.9, and (3) incorporation of a parameter that takes the effects of hadronic cascades into account. A summary of the model variants is shown in Table 1.1. Here we do not report on the results of the latter two. In the end, the most precise results were obtained by fixing the parameter for the effective hadronic interaction cross section at either of two plausible values. We report below on the baseline model and three variants of this model.

The model uses a realistic mass distribution [28] of the Woods-Saxon form to describe the three nuclei:

$$\rho(x, y, z) = \frac{\rho_0}{1 + \exp((r - c)/a)} \tag{1.14}$$

where $\rho_0 = 0.17$ nucleons/fm, $a = 0.5$ fm and c is computed numerically to give a nucleus with A nucleons.

The Monte Carlo technique is used to average over the initial positions of the struck quark in the nucleus, with an interaction probability weighting proportional to the density function. The distribution of production lengths l_p was modeled in two ways:

1. By a decaying exponential function with average L_p, and

Variant	Number of free parameters	Free parameters	Fixed parameters
BL	3	q_0, L_p and σ	-
BLE	4	q_0, L_p, σ and δz	-
BL30	2	q_0 and L_p	$\sigma = 30$ mb
BL40	2	q_0 and L_p	$\sigma = 40$ mb
BLE30	3	q_0, L_p, and δz	$\sigma = 30$ mb
BLE40	3	q_0, L_p, and δz	$\sigma = 40$ mb

Table 1.1.: Model variants.

2. By a constant value (delta function), such as $L_{\rm p} = l_{\rm p}$.

A straight-line trajectory of the struck quark was assumed, and the integral of density as a function of path-length was computed for the color length and for the hadron length. Transverse momentum broadening was taken to be proportional to this integral, weighted by the q_0 parameter, and suppression due to a hadronic interaction was taken to be proportional to a decaying exponential using the effective hadronic cross section and the hadron length.

It was initially assumed that the fit parameters are independent of which nucleus is considered, for example, that the intrinsic production length is independent of the path-length. This is a reasonable assumption since the transverse momentum broadening is observed to be extremely small compared to the momentum of the quark, thus, the medium-stimulated energy loss is also expected to be very small (see Eqs. 1.8 and 1.10 above). Therefore, to a very good approximation, the propagation of the quark through the medium is essentially unaffected by the medium and proceeds as it normally would in the vacuum. In a subsequent test we relaxed this assumption, as discussed below. Unlike the production length, the hadron length depends strongly on its path-length through the medium, since the inelastic cross section assures a path-length dependent interaction with the medium a significant fraction of the time.

Specifically, the form of the transverse momentum broadening calculation is given in the following equation:

$$\Delta p_{\rm T}^2 = \left\langle q_0 \int_{z_0}^{z_0+l_{\rm p}} \rho(x_0, y_0, z) {\rm d}z \right\rangle_{x_0,y_0,z_0,L_{\rm p}} \tag{1.15}$$

The form of the multiplicity ratio is given in the following equation:

$$R_{\rm M} = \left\langle \exp\left(-\sigma \int_{z_0+l_{\rm p}}^{z_{\rm max}} \rho(x_0, y_0, z) {\rm d}z \right) \right\rangle_{x_0,y_0,z_0,L_{\rm p}} \tag{1.16}$$

where (x_0, y_0, z_0) is the interaction point [a], and q_0 is a transport coefficient like connected with the usual transport coefficient as:

$$\hat{q} = q_0 \left\langle \frac{1}{l_{\rm p}} \int_{z_0}^{z_0+l_{\rm p}} \rho(x_0, y_0, z) {\rm d}z \right\rangle_{x_0,y_0,z_0,L_{\rm p}} \tag{1.17}$$

The fit of these two quantities is performed using ***MINUIT*** [29] in one $z_{\rm h}$ bin at a time for all of the nuclei. The minimization function is a combined χ^2 function defined by the transverse momentum broadening and multiplicity ratio data:

$$\chi^2(q_0, L_{\rm p}, \sigma) = \left(\frac{\text{data} - \text{model}}{\text{uncertainties}} \right)^2 \Bigg|_{\Delta p_{\rm T}^2} + \left(\frac{\text{data} - \text{model}}{\text{uncertainties}} \right)^2 \Bigg|_{R_{\rm M}} \tag{1.18}$$

[a] The interaction point is thrown using a uniform distribution within the size of the nucleus A and weighted by the nuclear density

The power of the fit of the multiplicity ratio and the p_{T} broadening for all of the nuclei to identify the important physics features of the data comes from the simultaneous nature of the fit. For example, for fixed q_0 in a specific event, a longer production length l_p necessarily produces a shorter hadron length l_{h}. This will be visible in the fit as more broadening and less hadron attenuation in a given bin in z_{h}. Because these observables have a very specific variation for the three heavier nuclei, the fit is strongly constrained.

The main aim of this work is to estimate the production length. The strongest constraint on this quantity is the shape of the distribution of p_{T} broadening vs. $A^{1/3}$. In the case that the production length is much longer than the diameter of the largest nucleus, in this model this distribution simply becomes a linear function. However, if the production length is smaller than the diameter of the largest nucleus, it introduces a curvature and a reduction in this function. This is illustrated in Fig. 1.3 (left panel) for fixed production lengths, i.e., for each curve the production length is a single value that does not vary event-by-event. The effect of a production length distribution is shown in Fig. 1.3 (right panel). As can be seen from this figure, the curvature persists to much longer average values of the production length, and the broadening is reduced compared to the case of fixed production length. This is due to the decaying exponential functional form used in the model for the production length distribution, since for any mean value of the production length there will always be events where the production length is substantially shorter than the mean value. This suggests that there may be some experimental sensitivity to the form of the production length distribution that could be exploited in future experiments at higher energies, where the production times are time-dilated to larger values.

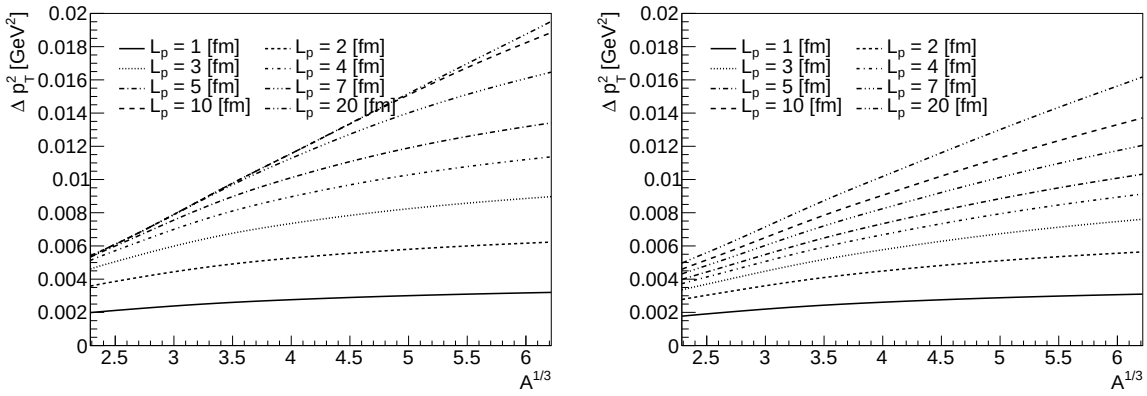

Figure 1.3.: Predictions of this model for p_{T} broadening vs. $A^{1/3}$ for values of the production length varying from smaller than the radius of any nucleus shown to larger than the diameter of any nucleus shown. The left panel shows the calculation assumes a fixed value of the production length for each line. The right panel shows the calculation assuming a *varying* value of the production length for each event, using a decaying exponential form. As can be seen, for production lengths which are smaller than the diameter of the largest nucleus, a curvature develops and the broadening is reduced in magnitude.

Further, if the production length is, in fact, described by a decaying exponential function, it means that even at the highest energies there will always be some contribution due to pre-hadrons interacting with the medium, because the events with $L_{\mathrm{p}} \approx 0$ will produce hadrons within the medium. On the other hand, this would also constitute a small violation of the QCD

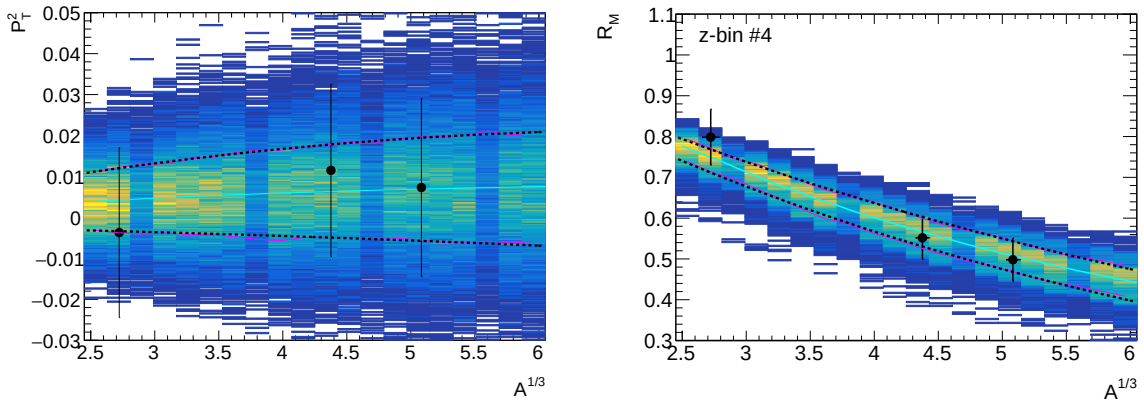

Figure 1.4.: Model function for Δp_{T}^2 (left) and R_{M} (right) resulting from the simultaneous fit for $z_{\mathrm{h}} = 0.94$, using the baseline model with two fit parameters at fixed pre-hadron cross-section. Superimposed, as a color map along the vertical axis, are the distribution of values computed using a Toy MC simulation for the determination of the model uncertainties. The dashed line represents the 68% confidence-level uncertainties obtained from gaussian fits in bins of $A^{1/3}$.

factorization theorem for this process, suggesting that the form found in nature may not be purely exponential for small values of the production length, to assure consistency with the factorization theorem.

1.5.2. Model uncertainties

The model uncertainties are determined using standard propagation of uncertainty techniques. A derivation of the model uncertainties is presented in Appendix A.2 for the transverse momentum broadening. For the multiplicity ratio it is not possible to determine its form analytically. Therefore, to evaluate the model uncertainties, Monte Carlo simulations were used.

Using the set of fitted parameters, namely q_0 and L_{p} for the two-free-parameter model variant (BL30), a Toy MC simulation is produced to obtain values of the transverse momentum broadening and multiplicity ratio as a function of $A^{1/3}$. Values of the parameters, q_0 and L_{p}, are thrown using a multivariate gaussian distribution with mean and covariance defined by the output of the fit. The thrown values are used to compute a distribution for the two studied observables.

An example of the computation of the model uncertainties are shown in Figure 1.4. The results for $z_{\mathrm{h}} = 0.94$ are presented here to describe the procedure to obtain the model uncertainties. For the transverse momentum broadening case, the black dashed lines are the theoretical uncertainties which are in agreement with the Toy MC uncertainties drawn in pink. The uncertainties are determined for each bin of $A^{1/3}$ using gaussian fits to the distribution of values obtained for the transverse momentum broadening or multiplicity ratio. The average value of the fitted gaussian is not used, but the standard deviation at 68% confidence level is used to define the model uncertainties. An example of the procedure is show in Figure 1.5.

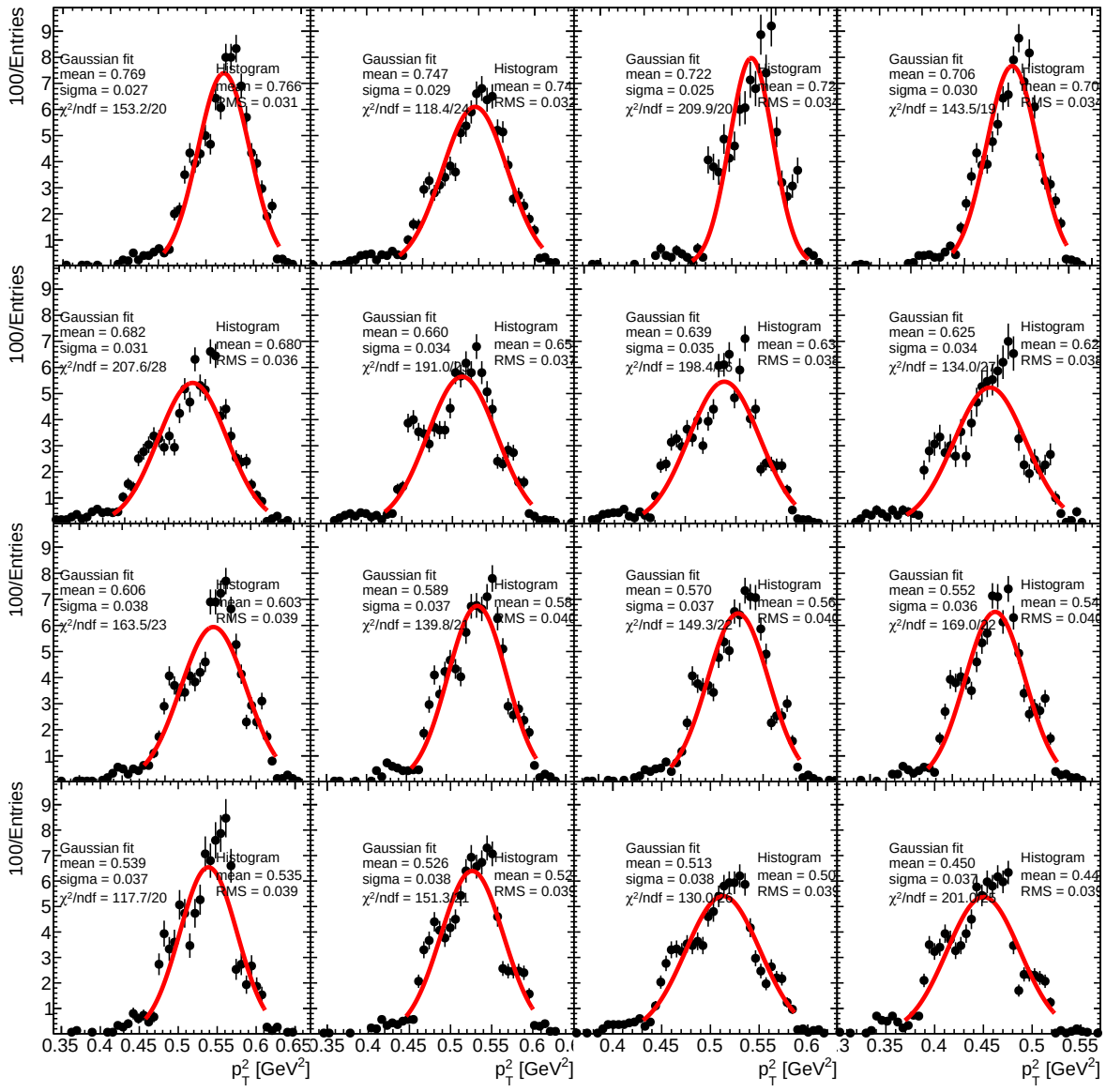

Figure 1.5.: Example of gaussian fits to the transverse momentum broadening distribution values in bins of $A^{1/3}$ used to determine the model uncertainties. The uncertainty for a given bin of $A^{1/3}$ is given by the standard deviation of the fitted gaussian at 66% confidence level.

1.6. Results and Discussion

Example results of the simultaneous fit to the data for the four z_h bins are shown in Figure 1.6 for the transverse momentum broadening and the multiplicity ratio.

Plots of the values of chi-squared per degree of freedom are shown in Fig. 1.11 for the six primary model variants, which are explained in Table 1.1. The best fit results overall are for the BL30 and BL40 variant, which have a maximum χ^2 per degree of freedom of approximately 1.2 at the lowest point in z_h. The lower fit quality for the lowest value of z_h could be due to the limitations of the assumptions of the model, which do not take into account the effect of hadronic cascades. Hadronic cascades will preferentially populate the low-z_h region of the multiplicity ratio, increasing the ratio due to bin migration from higher-z_h bins. We have confirmed that adding another parameter to the baseline model to take this into account produces satisfactory fits over the entire z_h region without adversely affecting the higher z_h fits. Including this parameter does not change the fit results for the three higher z_h bins, but it does improve the fit for the lowest bin in z_h, as expected.

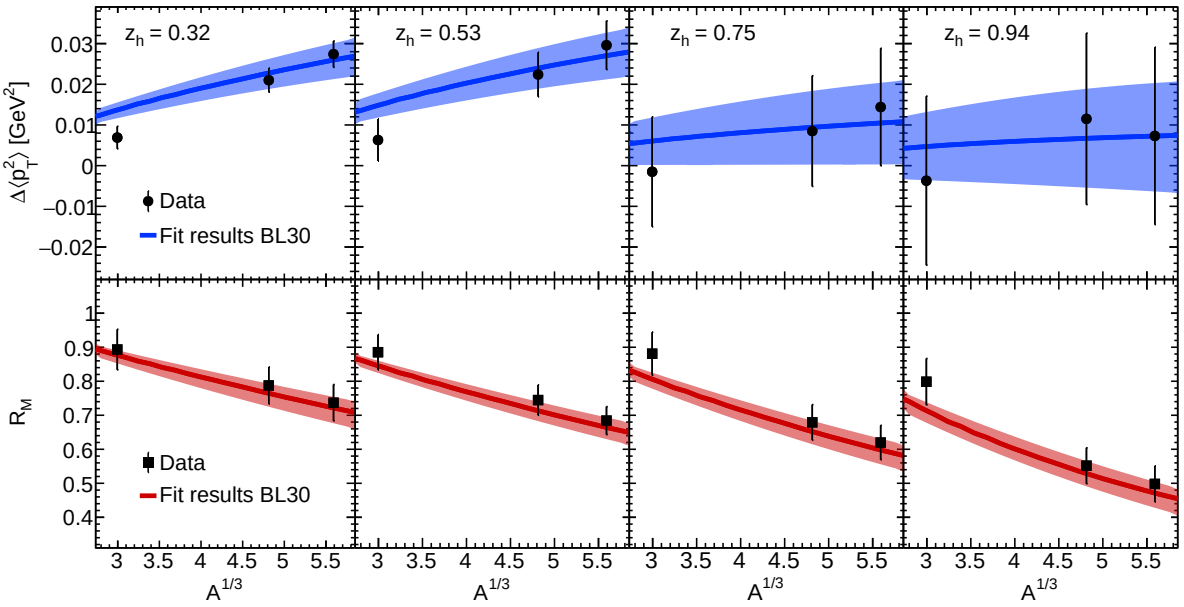

Figure 1.6.: Model function for Δp_T^2 (upper panels) and R_M (lower panels) resulting from the simultaneous fit, using the baseline model with two fit parameters at fixed pre-hadron cross-section. The four columns, from left to right, correspond to average values of z_h of 0.32, 0.53, 0.75, and 0.94, respectively.

In the following we report on the values of the fit parameters. First, the results of the fit parameters for the baseline models with and without energy loss for different degree of correlations of the helium background subtraction are presented. Then, the results of the fit parameters for different model variants are shown for the case of uncorrelated uncertainties between the helium and other nuclei.

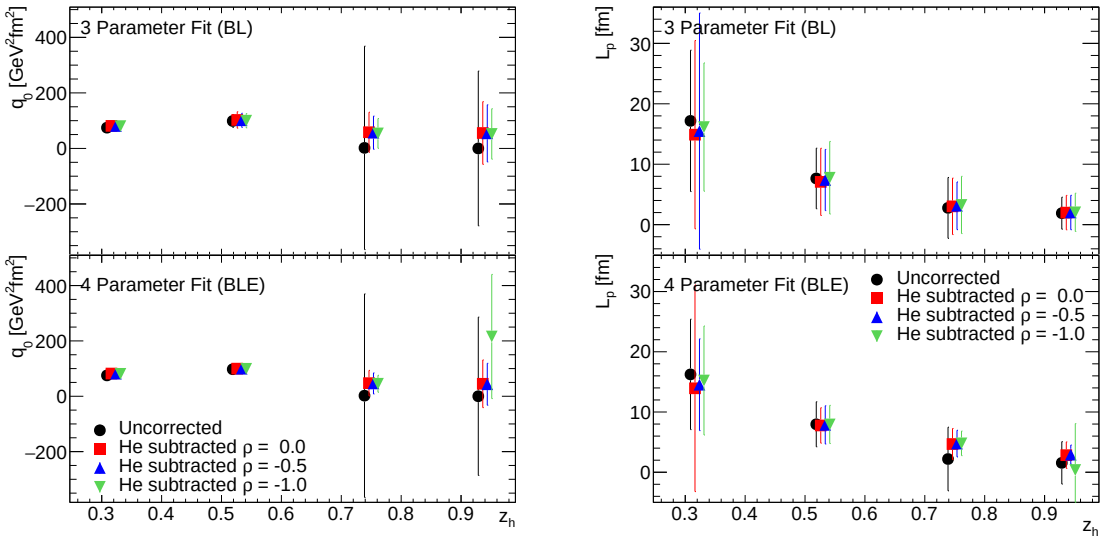

(a) Transport coefficient like parameter

(b) Production length

Figure 1.7.: Results of the fit parameters q_0 and L_p as a function of z_h for different degrees of correlation in the helium background subtraction for the model variants BL and BLE.

1.6.1. Fit parameters results for different degrees of correlation in the helium background subtraction

In the following the results for the fit parameters are shown for the case of the model variants BL and BLE, as defined in Table 1.1. The summary of all the fit parameters are shown in Figure 1.7 for the transport coefficient like and produciton and in Figure 1.8 for the pre-hadron–nucleon cross section and energy shift. In general it is shown that different degrees of correlations do not change the result and both model variants follow the same trend in all the parameters with bigger or smaller uncertainties.

The choice of a given degree of correlation is driven by the results of the χ^2 per degree of freedom observed for each case, as shown in Figure 1.9 where the best case or best scenario is for the case of uncorrelated uncertainties between the transverse momentum broadening measured in helium and other nuclei. This choice is more relevant only for the first z_h bin, where the values of the χ^2 per degree of freedom scatters more to values close to 3 for the case of a fully correlated case. This result also reveals that do not performing the removal of the helium affects the response of the model in the description of the data for the lowest z_h bin.

In following parts of the analysis the choice of uncorrelated d$\rho = 0$ is kept.

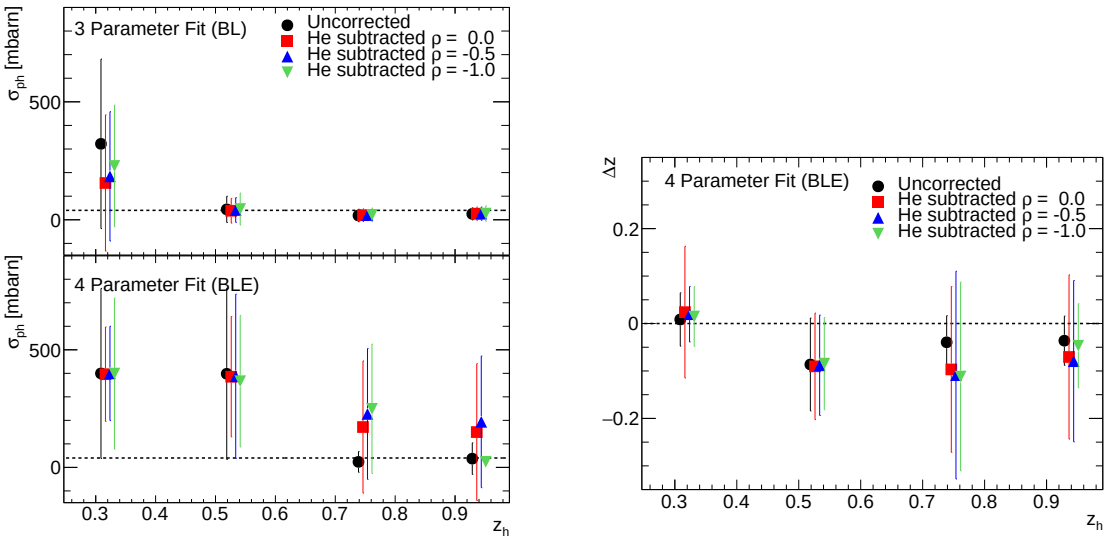

(a) Pre-hadron–nucleon cross section

(b) Energy shift

Figure 1.8.: Results of the fit parameters σ and δz as a function of z_{h} for different degrees of correlation in the helium background subtraction for the model variants BL and BLE.

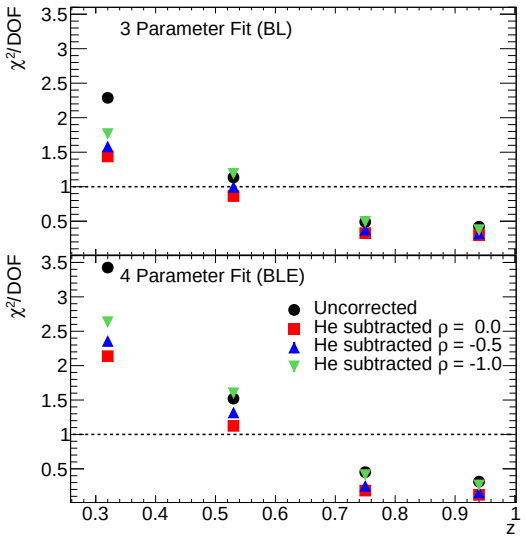

Figure 1.9.: Chi-squared per degree of freedom of the fit as a function of z_{h} for the model variants BL and BLE for different degree of correlation in the subtraction of the helium background from the transverse momentum broadening.

1.6.2. Fit parameter results for different model variants

The primary results of this work is the extraction of the production length and the transport coefficient. The fit results of different model variants are shown in Figure 1.10 where the transport-life coefficient, q_0, and the production length is shown as a function of the z_h variable.

For the transport coefficient like q_0 the results show that there is no defined trend as a function of z_h. Different model variants give similar results with all the point scattering around the same values and consistent with each other within uncertainties. The result for the transport coefficient $\hat{q}$ is shown in Section 1.6.5.

The dependence of the production length L_p on z_h that is similar in functional form to that given by the Lund string model as given in Eq. 1.1, and which has a magnitude ranging from 3 to 9 fm for the best-fitted variants BL30 and BL40. The magnitude of the L_p parameter to be robust to any variations in the model for $z_h > 0.5$, such as the model variants described above. It is primarily fixed by the curvature of the p_T broadening as a function of $A^{1/3}$.

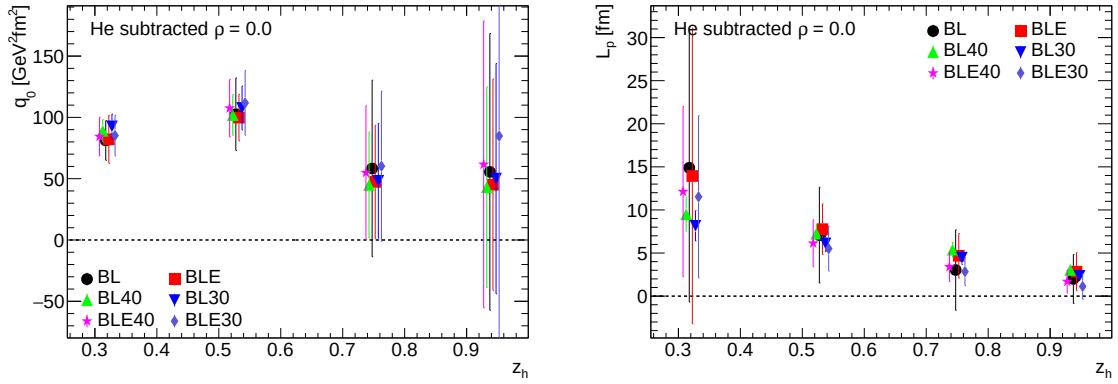

(a) Transport coefficient like parameter

(b) Production length

Figure 1.10.: Results of the fit parameters q_0 and L_p as a function of z_h for different model variants and the case of uncorrelated uncertainties for the helium subtraction.

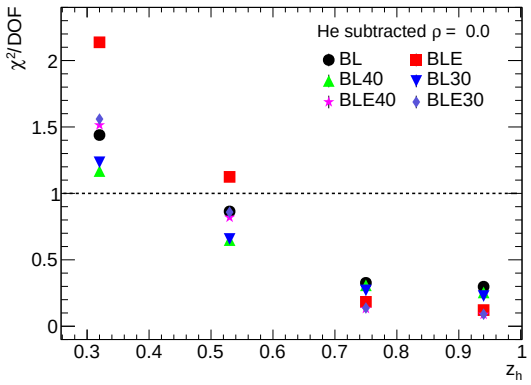

Figure 1.11.: χ^2 per degree of freedom of the fit as a function of z_h for different model variants and the case of uncorrelated uncertainties for the helium subtraction.

1.6.3. Test of nuclear size dependence of the production length

The choice of the distribution of the production length was assumed to be independent of the nuclear size for all model variants. The main assumption was to consider an exponential distribution of production lengths with average L_p. The case where a potential dependence on a power law of A is tested, by parametrizing the production length as:

$$L(A) = L_0 + c_1 A^{1/3} + c_2 A^{2/3} \tag{1.19}$$

Among the possible cases, the more successful results are the cases where $L_0 = 0$ and $c_1 = 0$, more specifically:

$$L(A) = c_1 A^{1/3} + c_2 A^{2/3} \quad \text{and} \quad L(A) = L_0 + c_2 A^{2/3}$$

The results of this test are shown in Figure 1.12. The main finding is a weak dependence on A due to the large uncertainties obtained. An interesting feature is the trend of the centroids which curve differently at low z_h.

The ratios shown in the lower panels of Figure 1.12 shown the relative difference with respect to the results in the case of $L(A) = L_0$ which correspond to the nominal model variant BL30 that has been already presented. Despite that the ratios seem to be consistent with no change within uncertainties, there is a systematic trend which could be further investigated with more data in the future.

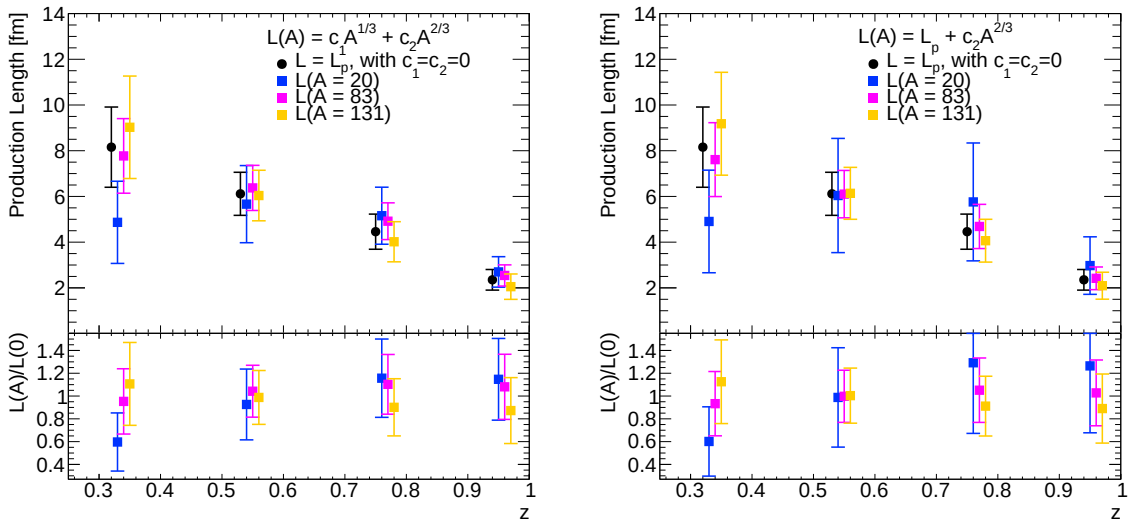

Figure 1.12.: Two cases to test the dependence on the nuclear size A for the production length modeled as $L_{\mathrm{p}}(A) = c_1 A^{1/3} + c_2 A^{2/3}$ (left panel) and $L_{\mathrm{p}}(A) = L_0 + c_2 A^{2/3}$ (right pannel). The ratios show the difference relative to the case where the production length is independent of the nuclear size.

1.6.4. Test of the Lund String Model

The fit results of the production length L_{p} as a function of z_{h} serve as a powerful tool to probe the dynamics derived from the Lund String Model for the simplest case of the struck quark. As defined in Eq. 1.1, a linear dependence on the variable z_{h} is expected.

The results for the model variant BL30 are shown in Figure 1.13 with a fit to this linear form, which is also a function of the kinematic variables Q^2 and ν. These variables are not constrained from this linear fit, but values are taken from experimental results of HERMES. The mass of the proton is taken to be the PDG proton mass. Therefore, the only free remaining parameter is κ, the Lund string constant. The result is:

$$\kappa = 0.98 \pm 0.09 \text{ GeV/fm} \tag{1.20}$$

This value is in agreement with the theoretical expected value of 1 GeV/fm for the cold nuclear environment of deep-inelastic scattering in nuclei at low energies, where the strings are not expected to melt [**Cite**].

It is also possible to test the results against a full form that includes higher rank hadrons, as defined in Eq. 1.2. This form has the issue of not containing any information about the kinematic variables since it is encapsulated in a scale parameter as:

$$L_{\mathrm{p}}(z_{\mathrm{h}}) = f(Q^2, \nu) \cdot z_{\mathrm{h}} \frac{\log\left(1/z_{\mathrm{h}}^2\right) - 1 + z_{\mathrm{h}}^2}{1 - z_{\mathrm{h}}^2},$$

where $f(Q^2, \nu)$ should contain terms connected with the linear form for the struck quark. The larger advantage of this form is that of allowing the production length to be zero in the limits of $z_h = 0$ and $z_h = 1$. The fit of the obtained production length L_p as a function of z_h to this form is shown in Figure 1.13. Due to the uncertainties the value of the χ^2 for both types of dependences are comparable and both describe well the data.

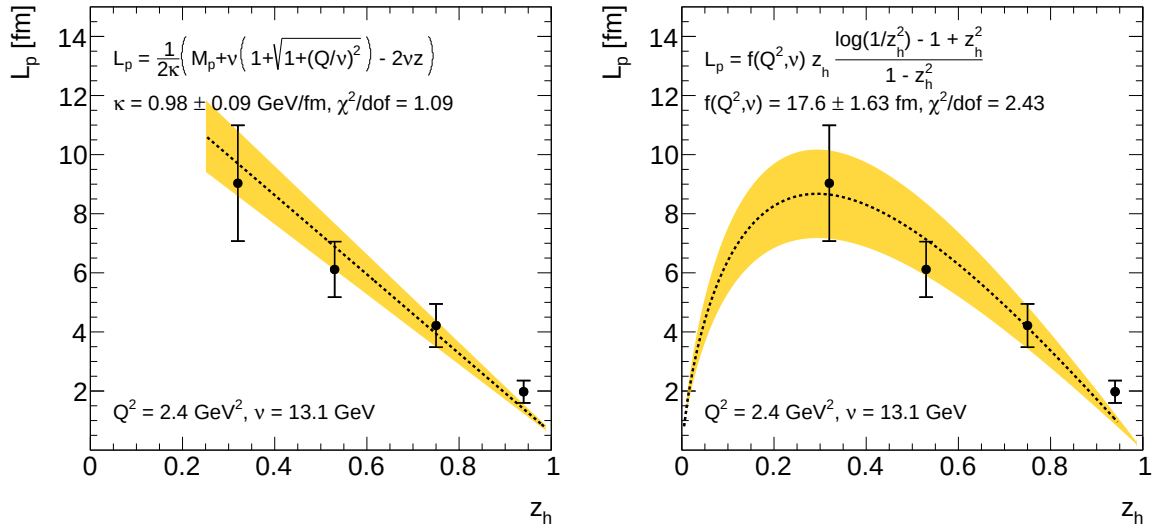

Figure 1.13.: Fit of the extracted values of the production length as a function of z_h to the linear form of the production length derived from the Lund String Model describing the struck quark only (left). A fit to a more complex form is also shown, which includes a description of higher rank hadrons (right). The band uncertainties correspond the 68% confidence intervals to this fits.

1.6.5. Transport coefficient

The transport coefficient $\hat{q}$ is derived from the transport coefficient like q_0, which is determined by the fit. Its value is obtained using the relationship shown in Eq. 1.17. This is qualitatively equivalent to:

$$\hat{q} = \frac{\Delta p_T^2}{L_p}$$

The results of the transport coefficient $\hat{q}$ are shown in Figure 1.14 as a function of z_h. Given that $\hat{q}$ depends on the average density times path length travelled by the quark, it has a dependence on the nuclear size A. Despite the apparent systematic trend to increase the value of $\hat{q}$ with increasing z_h, all the values are consistent with each other, within uncertainties. The average

values obtained for all three nuclei are:

$$\begin{aligned} \hat{q}(\mathrm{Ne}) &= 0.072 \pm 0.006\ \mathrm{GeV}^2/\mathrm{fm} \\ \hat{q}(\mathrm{Kr}) &= 0.120 \pm 0.010\ \mathrm{GeV}^2/\mathrm{fm} \\ \hat{q}(\mathrm{Xe}) &= 0.137 \pm 0.011\ \mathrm{GeV}^2/\mathrm{fm} \end{aligned}$$

This values are comparable with the predictions made for proton–lead collisions at LHC energies [30, 31] which predicts a value of:

$$\hat{q} = 0.075^{+0.015}_{-0.005}\ \mathrm{GeV}^2/\mathrm{fm}$$

This predicted value is shown in Figure 1.14 as a dashed line and a shadowed box to represent its uncertainty.

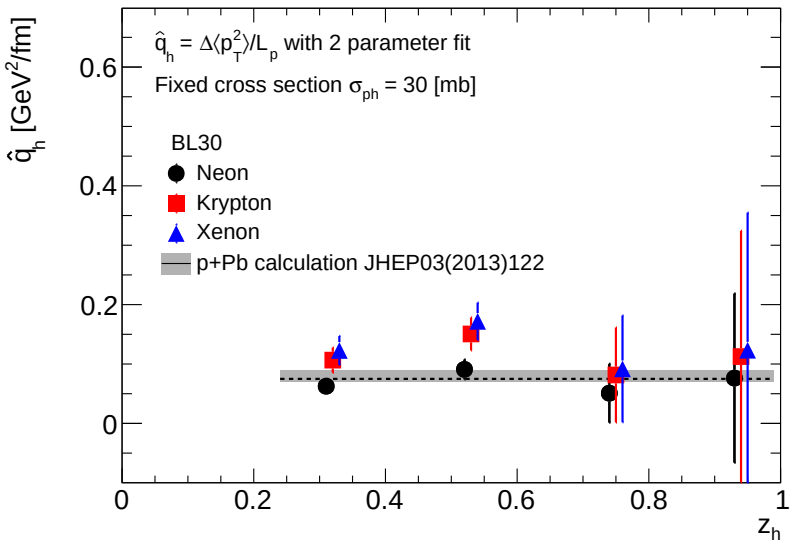

Figure 1.14.: The $\hat{q}$ transport coefficient as a function of z_h for different nuclei. The result is compared to a theoretical prediction for proton–lead collisions at the LHC shown in a shaded box.

1.6.6. Estimations for future experiments

It is possible to estimate the production lengths that should be observed in future experiments, such as the 12 GeV upgrade at Jefferson Lab and the proposed Electron Ion Collider. Some examples of the kinematic values for different experiments are presented in Table 1.2.

Using Eq. 1.1 for $\kappa = 1$ and varying the value of Q^2 and ν as expected for future kinematic conditions the values of the production length can be estimated. Another possible method to estimate the production length at different energies is to use a relativistic extrapolation of the measured production length, using the velocity β and Lorentz factor γ determined in Eqs. 1.5 and 1.6. Then assuming that the time intervals over which the colored quark propagates must

Experiment	Q^2 [GeV^2]	ν [GeV]
HERMES	2.4	10.8–14.5
CLAS	3	4
CLAS12	7	2.45
EIC	32.5	9.33
EIC	140	20.85

Table 1.2.: Some kinematic values for different experiments.

be equal in any reference frame, it is possible to write the relationship:

$$\left(\frac{1}{\gamma}\frac{L_\mathrm{p}}{\beta}\right)\Big|_{Q^2,\nu} = \left(\frac{1}{\gamma}\frac{L_\mathrm{p}}{\beta}\right)\Big|_{Q^2,\nu} \quad \text{as measured in HERMES} \tag{1.21}$$

The results of both kinds of estimations are shown in Figures 1.16 and 1.15 as a function of Q^2 and ν. In both cases the values are computed around a value of x-Bjorken around $x_\mathrm{Bj} = 0.2 \pm 0.1$ to look into a region of interest. This is shown as an envelope in both curves. The x-Bjorken envelope shows to be very narrow for the case of using the Lund String Model (LSM) extrapolation in the ν dependence. An interesting feature is the fast growing behavior of both curves, being the relativist extrapolation much more conservative with respect to the LSM extrapolation. The agreement between both methods improves with larger values of z_h, as expected for the assumptions made for the LSM model derivation, which assumes the case of the struck quark.

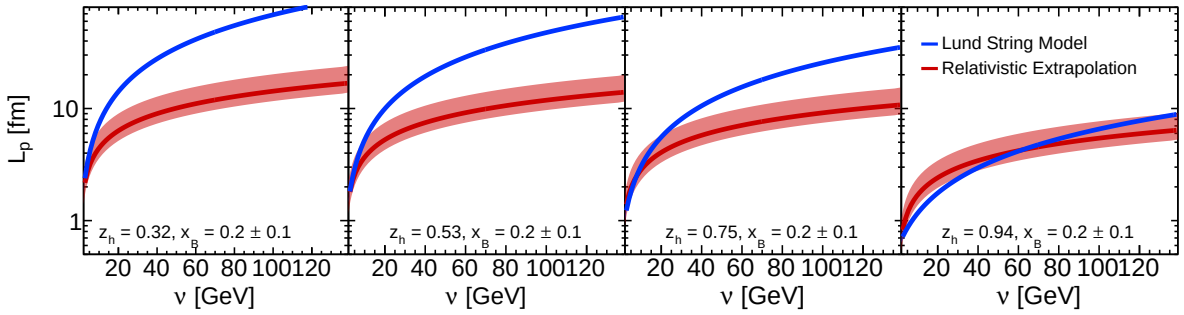

Figure 1.15.: Estimations of the production length as a function of the photon energy ν for different values of z_h. Uncertainty bands in the estimations are determined by varying the values of Bjorken-x $x_\mathrm{Bj} = 0.2 \pm 0.1$.

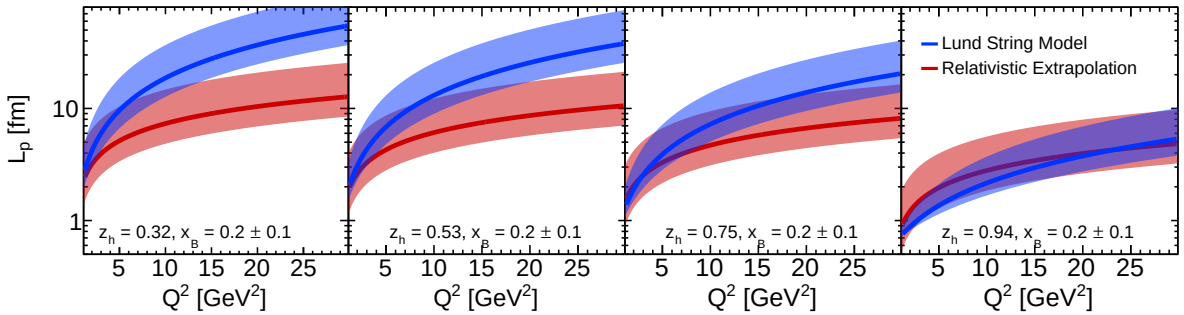

Figure 1.16.: Estimations of the production length as a function of the momentum transfer Q^2 for different values of z_h. Uncertainty bands in the estimations are determined by varying the values of Bjorken-x $x_{Bj} = 0.2 \pm 0.1$.

1.7. Summary

Using a simple geometric model that describes transverse momentum broadening and multiplicity ratios simultaneously, the characteristic production time and transport coefficient of π^+ are obtained using HERMES data, for the first time. No dynamical information is assumed; it emerges from fit. Many model variants are studied.

The production time or production length is found to range from 10 to 2 fm from the lowest to the highest z-bin. Its decreasing trend is in agreement with a functional form obtained from the Lund String Model for the struck quark in the simplest case. An extra fit of the obtained production length as a function of z_h to the Lund String Model allows to extract the Lund string constant, κ, and it is found to be consistent with its theoretical expected value.

The transport coefficient is found to be in the range of 0.072 to 0.137 GeV^2/fm. This value is compatible with theoretical predictions based on fits to Drell-Yan data from p+Pb collisions at the LHC.

Finally, the proposed approach allows to compute estimates of the production length at different energies. Two methods are available. The first one is based in the linear form derived from the Lund String Model, where the Q^2 and ν dependence is used for the estimates and the second is a relativist extrapolation which uses the Lorentz factor and initial velocity of the quark, expressed as a function of Q^2 and ν, to extrapolate the production length to different energies.

References

[1] ATLAS Collaboration. "Measurement of the inclusive jet cross-section in proton–proton collisions at $\sqrt{s}$ = 7 TeV using 4.5 fb^{-1} of data with the ATLAS detector". ***JHEP*** 02 (2015), p. 153. DOI: 10.1007/JHEP02(2015)153. arXiv: 1410.8857 [hep-ex]. Erratum: ***JHEP*** 09 (2015), p. 141. DOI: 10.1007/JHEP09(2015)141.

[2] David J. Gross and Frank Wilczek. "Ultraviolet Behavior of Nonabelian Gauge Theories". ***Phys. Rev. Lett.*** 30 (1973), pp. 1343–1346. DOI: 10.1103/PhysRevLett.30.1343.

[3] H. David Politzer. "Reliable Perturbative Results for Strong Interactions?" ***Phys. Rev. Lett.*** 30 (1973), pp. 1346–1349. DOI: 10.1103/PhysRevLett.30.1346.

[4] John C. Collins, Davison E. Soper, and George F. Sterman. "Factorization of Hard Processes in QCD". ***Adv. Ser. Direct. High Energy Phys.*** 5 (1989), pp. 1–91. DOI: 10.1142/9789814503266_0001. arXiv: hep-ph/0409313 [hep-ph].

[5] Raul A. Briceno et al. "The resonant $\pi^+\gamma \to \pi^+\pi^0$ amplitude from Quantum Chromodynamics". ***Phys. Rev. Lett.*** 115 (2015), p. 242001. DOI: 10.1103/PhysRevLett.115.242001. arXiv: 1507.06622 [hep-ph].

[6] Silas R. Beane et al. "Ab initio Calculation of the $np \to d\gamma$ Radiative Capture Process". ***Phys. Rev. Lett.*** 115.13 (2015), p. 132001. DOI: 10.1103/PhysRevLett.115.132001. arXiv: 1505.02422 [hep-lat].

[7] Thomas Gutsche et al. "Nucleon structure in a light-front quark model consistent with quark counting rules and data". ***Phys. Rev.*** D91 (2015), p. 054028. DOI: 10.1103/PhysRevD.91.054028. arXiv: 1411.1710 [hep-ph].

[8] Thomas Gutsche et al. "Nuclear physics in soft-wall AdS/QCD: Deuteron electromagnetic form factors". ***Phys. Rev.*** D91.11 (2015), p. 114001. DOI: 10.1103/PhysRevD.91.114001. arXiv: 1501.02738 [hep-ph].

[9] N. Barnea et al. "Effective Field Theory for Lattice Nuclei". ***Phys. Rev. Lett.*** 114.5 (2015), p. 052501. DOI: 10.1103/PhysRevLett.114.052501. arXiv: 1311.4966 [nucl-th].

[10] C. Ji, Ch. Elster, and D. R. Phillips. "^{6}He nucleus in halo effective field theory". ***Phys. Rev.*** C90.4 (2014), p. 044004. DOI: 10.1103/PhysRevC.90.044004. arXiv: 1405.2394 [nucl-th].

[11] ATLAS Collaboration. "Observation of Long-Range Elliptic Azimuthal Anisotropies in $\sqrt{s}$ = 13 and 2.76 TeV pp Collisions with the ATLAS Detector". ***Phys. Rev. Lett.*** 116 (2016), p. 172301. DOI: 10.1103/PhysRevLett.116.172301. arXiv: 1509.04776 [hep-ex].

[12] L. Adamczyk et al. "Measurement of elliptic flow of light nuclei at $\sqrt{s_{NN}}$ = 200, 62.4, 39, 27, 19.6, 11.5, and 7.7 GeV at the BNL Relativistic Heavy Ion Collider". ***Phys. Rev.*** C94.3 (2016), p. 034908. DOI: 10.1103/PhysRevC.94.034908. arXiv: 1601.07052 [nucl-ex].

[13] H. Al Ghoul et al. "First Results from The GlueX Experiment". ***AIP Conf. Proc.*** 1735 (2016), p. 020001. DOI: 10.1063/1.4949369. arXiv: 1512.03699 [nucl-ex].

[14] Tanja Horn and Craig D. Roberts. "The pion: an enigma within the Standard Model". ***J. Phys.*** G43.7 (2016), p. 073001. DOI: 10.1088/0954-3899/43/7/073001. arXiv: 1602.04016 [nucl-th].

[15] A. Airapetian et al. "Transverse momentum broadening of hadrons produced in semi-inclusive deep-inelastic scattering on nuclei". ***Phys. Lett.*** B684 (2010), pp. 114–118. DOI: 10.1016/j.physletb.2010.01.020. arXiv: 0906.2478 [hep-ex].

[16] A. Airapetian et al. "Hadronization in semi-inclusive deep-inelastic scattering on nuclei". ***Nucl. Phys.*** B780 (2007), pp. 1–27. DOI: 10.1016/j.nuclphysb.2007.06.004. arXiv: 0704.3270 [hep-ex].

[17] A. Airapetian et al. "Multidimensional Study of Hadronization in Nuclei". ***Eur. Phys. J.*** A47 (2011), p. 113. DOI: 10.1140/epja/i2011-11113-5. arXiv: 1107.3496 [hep-ex].

[18] R. Baier, D. Schiff, and B. G. Zakharov. "Energy loss in perturbative QCD". ***Ann. Rev. Nucl. Part. Sci.*** 50 (2000), pp. 37–69. DOI: 10.1146/annurev.nucl.50.1.37. arXiv: hep-ph/0002198 [hep-ph].

[19] S. Peigne and A. V. Smilga. "Energy losses in a hot plasma revisited". ***Phys. Usp.*** 52 (2009), pp. 659–685. DOI: 10.3367/UFNe.0179.200907a.0697. arXiv: 0810.5702 [hep-ph].

[20] A. Accardi et al. "Parton Propagation and Fragmentation in QCD Matter". ***Riv. Nuovo Cim.*** 32 (2010), pp. 439–553. DOI: 10.1393/ncr/i2009-10048-0. arXiv: 0907.3534 [nucl-th].

[21] A. Majumder and M. Van Leeuwen. "The Theory and Phenomenology of Perturbative QCD Based Jet Quenching". ***Prog. Part. Nucl. Phys.*** 66 (2011), pp. 41–92. DOI: 10.1016/j.ppnp.2010.09.001. arXiv: 1002.2206 [hep-ph].

[22] Enke Wang and Xin-Nian Wang. "Jet tomography of dense and nuclear matter". ***Phys. Rev. Lett.*** 89 (2002), p. 162301. DOI: 10.1103/PhysRevLett.89.162301. arXiv: hep-ph/0202105 [hep-ph].

[23] Bo Andersson et al. "Parton Fragmentation and String Dynamics". ***Phys. Rept.*** 97 (1983), pp. 31–145. DOI: 10.1016/0370-1573(83)90080-7.

[24] A. Bialas and M. Gyulassy. "Lund Model and an Outside - Inside Aspect of the Inside - Outside Cascade". ***Nucl. Phys.*** B291 (1987), p. 793. DOI: 10.1016/0550-3213(87)90496-2.

[25] K. Gallmeister and U. Mosel. "Time Dependent Hadronization via HERMES and EMC Data Consistency". ***Nucl. Phys.*** A801 (2008), pp. 68–79. DOI: 10.1016/j.nuclphysa.2007.12.009. arXiv: nucl-th/0701064 [nucl-th].

[26] D. Adikaram et al. "Towards a resolution of the proton form factor problem: new electron and positron scattering data". ***Phys. Rev. Lett.*** 114 (2015), p. 062003. DOI: 10.1103/PhysRevLett.114.062003. arXiv: 1411.6908 [nucl-ex].

[27] V. Del Duca, Stanley J. Brodsky, and Paul Hoyer. "The Space-time structure of deep inelastic lepton - hadron scattering". ***Phys. Rev.*** D46 (1992), pp. 931–943. DOI: 10.1103/PhysRevD.46.931.

[28] H. P. Blok and L. Lapikas. "A-dependence of hadronization in nuclei". ***Phys. Rev.*** C73 (2006), p. 038201. DOI: 10.1103/PhysRevC.73.038201. arXiv: nucl-th/0512024 [nucl-th].

[29] F. James and M. Roos. "Minuit: A System for Function Minimization and Analysis of the Parameter Errors and Correlations". ***Comput. Phys. Commun.*** 10 (1975), pp. 343–367. DOI: 10.1016/0010-4655(75)90039-9.

[30] Francois Arleo and Stephane Peigne. "Heavy-quarkonium suppression in p-A collisions from parton energy loss in cold QCD matter". ***JHEP*** 03 (2013), p. 122. DOI: 10.1007/JHEP03(2013)122. arXiv: 1212.0434 [hep-ph].

[31] Javier L. Albacete et al. "Predictions for Cold Nuclear Matter Effects in p+Pb Collisions at $\sqrt{s_{NN}} = 8.16$ TeV". ***Nucl. Phys.*** A972 (2018), pp. 18–85. DOI: 10.1016/j.nuclphysa.2017.11.015. arXiv: 1707.09973 [hep-ph].

Chapter 2.

Elliptic flow of J/ψ in Pb+Pb collisions with the ATLAS detector

2.1. Introduction

With the advent of lead-lead collisions at the centre-of-mass energy of 5.02 TeV per nucleon-nucleon pair, new opportunities open up for understanding the detailed properties of the hot dense plasma produced in such collisions. A special advantage of studies with quarkonia as a hard probe in the plasma is that the comparison of prompt and non-prompt J/ψ mesons elucidates the differences in the responses of the produced c-quark and b-quark systems. This is because the prompt mesons are $c\bar{c}$ systems produced within a short time after the collision while the non-prompt mesons come from decays of B-hadrons that are formed outside the medium [1]. Thus, the comparison of these two classes of J/ψ mesons probes the flavour dependence of the mechanisms of the interactions of heavy quarks with the medium. As shown in Fig. 2.1 and 2.2, ATLAS measurements of the attenuation of both prompt and non-prompt J/ψ mesons yields indicate very strong medium effects that are surprisingly similar in magnitude at this collision energy [2, 3].

A complementary and powerful probe into the heavy-quark flavour dependence of interaction mechanisms can be obtained by studying the azimuthal asymmetries of prompt and non-prompt quarkonia. Such studies [4, 5, 6] are especially useful in the transverse momentum range $9 < p_{\mathrm{T}} < 30$ GeV, investigated in this paper, since this range represents the transition region spanning from the lower p_{T} region, in which recombination processes are believed to play an important role [7, 8], to the higher p_{T} region in which other processes dominate [9, 10, 11]. The naive expectation in this range is that recombination processes will partially couple the produced J/ψ to the hydrodynamic flow of the hot medium, resulting in an enhancement of the observed azimuthal asymmetry at lower p_{T} relative to higher p_{T} [8, 11]. In this picture, a flavour-dependent enhancement of the azimuthal asymmetry of J/ψ at low p_{T} can be interpreted as a difference in the degree of recombination of c- and b-quarks, with the expectation that any flavour dependence will vanish at higher values of p_{T}. A recent transport model study suggests the sensitivity of charm quarks to hydrodynamic flow [12]. Additionally, a strong prompt J/ψ yield suppression in the final state medium should lead to an azimuthal asymmetry even in the high p_{T} region [11].

In non-central collisions, the overlap region of the colliding ions has an elliptical shape. The particle yield is influenced by this matter distribution, leading to the observation of an azimuthal anisotropy relative to the reaction plane as observed for charged hadrons [13, 14, 15, 16, 17]. The azimuthal distribution of particles is characterised by a Fourier expansion of the particle yield:

$$\frac{\mathrm{d}N}{\mathrm{d}\phi} \propto 1 + \sum_{n=1}^{\infty} 2v_n \cos[n(\phi - \Psi_n)], \tag{2.1}$$

where ϕ is the azimuthal angle of the particle relative to the detector, and Ψ_n is the n-th harmonic of reaction plane angle, which can be estimated using the event-plane method [18]. The v_n coefficients are also usually expressed as:

$$v_n = \langle \cos[n(\phi - \Psi_n)] \rangle. \tag{2.2}$$

These coefficients depends on the transverse momentum of particles, rapidity and collision centrality. The second order coefficient, v_2 is referred to as elliptic flow and its magnitude quantifies the yield modulation relative to the elliptical shape of the initial matter distribution. It can be related to the eccentricity of the collision [18]:

$$v_2 = \left\langle \left(\frac{p_x}{p_\mathrm{T}}\right)^2 - \left(\frac{p_y}{p_\mathrm{T}}\right)^2 \right\rangle \tag{2.3}$$

Interestingly the observed azimuthal asymmetry for prompt J/ψ is the same in central collisions as in non-central collisions [6]. This is in contradiction with the hydrodynamic-expected behaviour, which is confirmed by the results for charged hadrons where the anisotropies are more significant in semi-central collisions than in peripheral and central collisions. This observation is an intriguing one that may ultimately provide more insight into the origins of azimuthal asymmetries beyond a simple hydrodynamic picture. Further, there seems to be a surprising universality among many different probes, such as D-mesons and jets [19, 20], for which the v_2 values are very similar at high p_T. This paper provides v_2 measurements as a function of transverse momentum, rapidity and collision centrality for both prompt and non-prompt J/ψ in the dimuon decay channel, extending the covered kinematic range of recent results of the other LHC experiments [4, 5, 6].

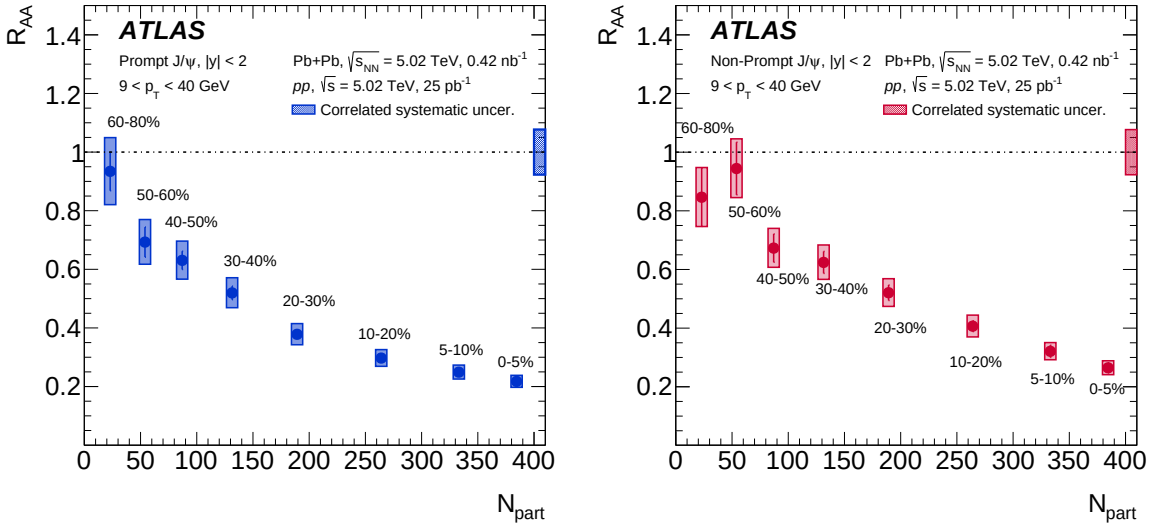

Figure 2.1.: The nuclear modification factor as a function of the number of participants, $\langle N_{\text{part}} \rangle$, for the prompt J/ψ (left) and non-prompt J/ψ (right) for $9 < p_{\text{T}} < 40$ GeVand for rapidity $|y| < 2$. The statistical uncertainty of each point is indicated by a narrow error bar. The error box plotted with each point represents the uncorrelated systematic uncertainty, while the shaded error box at $R_{\text{AA}} = 1$ represents correlated scale uncertainties. [2, 3].

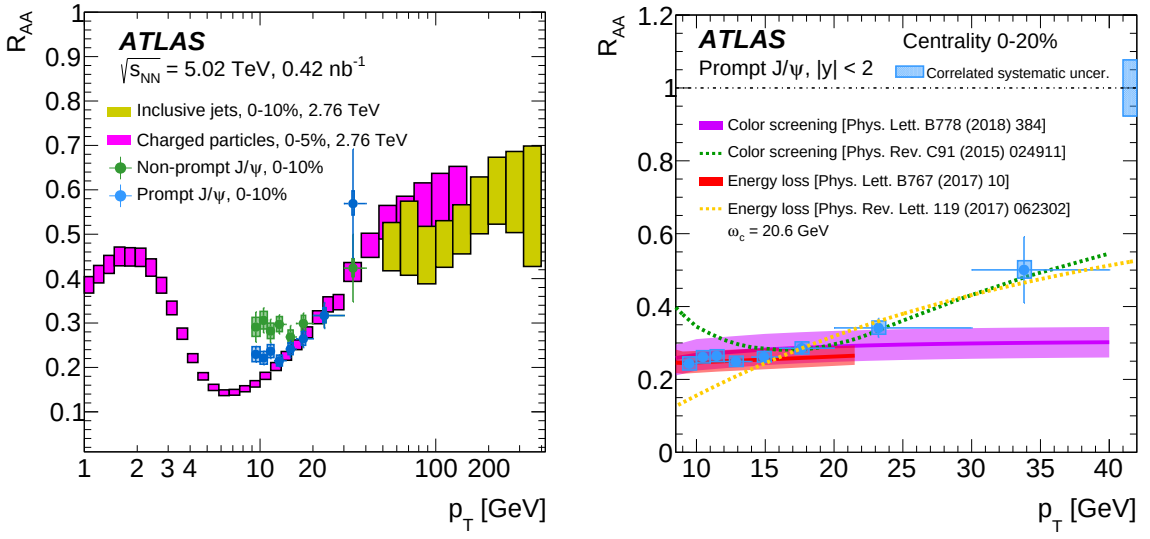

Figure 2.2.: (Left) Comparison of prompt and non-prompt J/ψ R_{AA} with the R_{AA} of charged particles [13]. (Right) Comparison of the R_{AA} for prompt J/ψ production with different theoretical models. The statistical uncertainty of each point is indicated by a narrow error bar. The error box plotted with each point represents the uncorrelated systematic uncertainty, while the shaded error box at $R_{\text{AA}} = 1$ represents correlated scale uncertainties [2].

2.2. ATLAS detector

The ATLAS detector [21] at the LHC covers nearly the entire solid angle around the collision point. Figure 2.3 gives an overview of the full detector. It consists of an inner tracking detector (ID) surrounded by a thin superconducting solenoid, electromagnetic and hadronic calorimeters, and a muon spectrometer (MS) incorporating three large superconducting toroid magnets.[a]

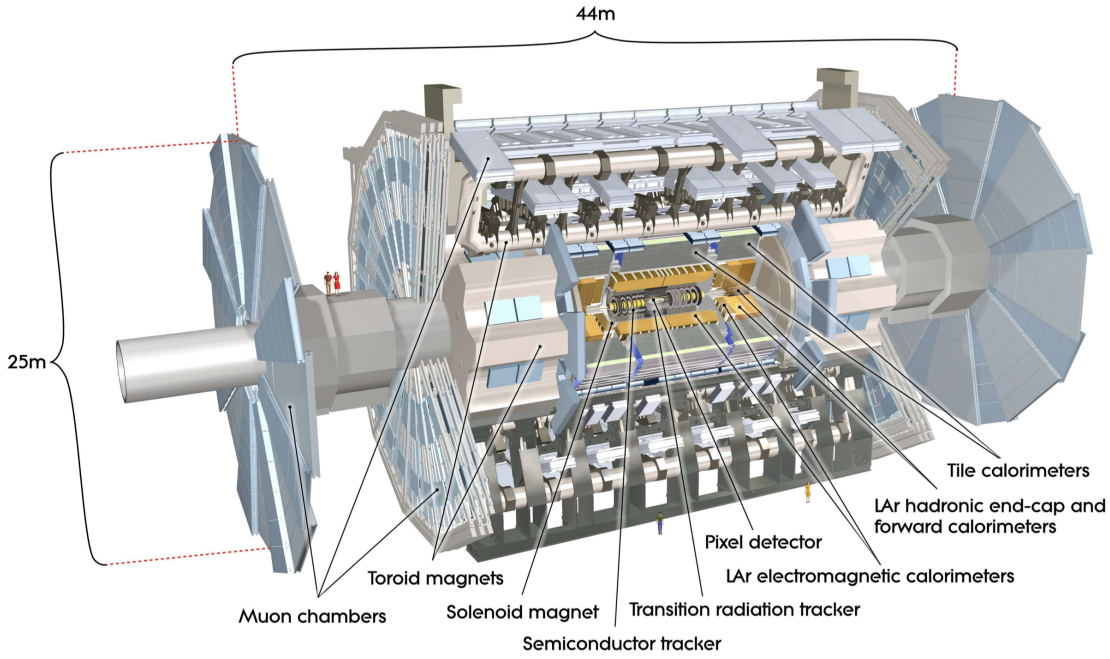

Figure 2.3.: Cut-away view of the ATLAS detector. The dimensions of the detector are 25 m in height and 44 m in length. The overall weight of the detector is approximately 7000 tonnes [21].

Inner detector

The inner detector is a very compact and sensitive tracking system. It measures the direction, momentum, and charge of charged particles. Figure 2.4 shown a cut-away view of the inner detector and its sub-systems. The high-granularity silicon pixel detector covers the interaction region and provides typically four measurements per track. It is followed by the silicon microstrip tracker which provides around eight two-dimensional measurement points per track. These silicon detectors are complemented by the transition radiation tracker (TRT), which

[a] ATLAS uses a right-handed coordinate system with its origin at the nominal interaction point in the centre of the detector and the z-axis along the beam pipe. The x-axis points from the interaction point to the centre of the LHC ring, and the y-axis points upwards. Cylindrical coordinates (r, ϕ) are used in the transverse plane, ϕ being the azimuthal angle around the z-axis. The pseudorapidity is defined in terms of the polar angle θ as $\eta = -\ln\tan(\theta/2)$.

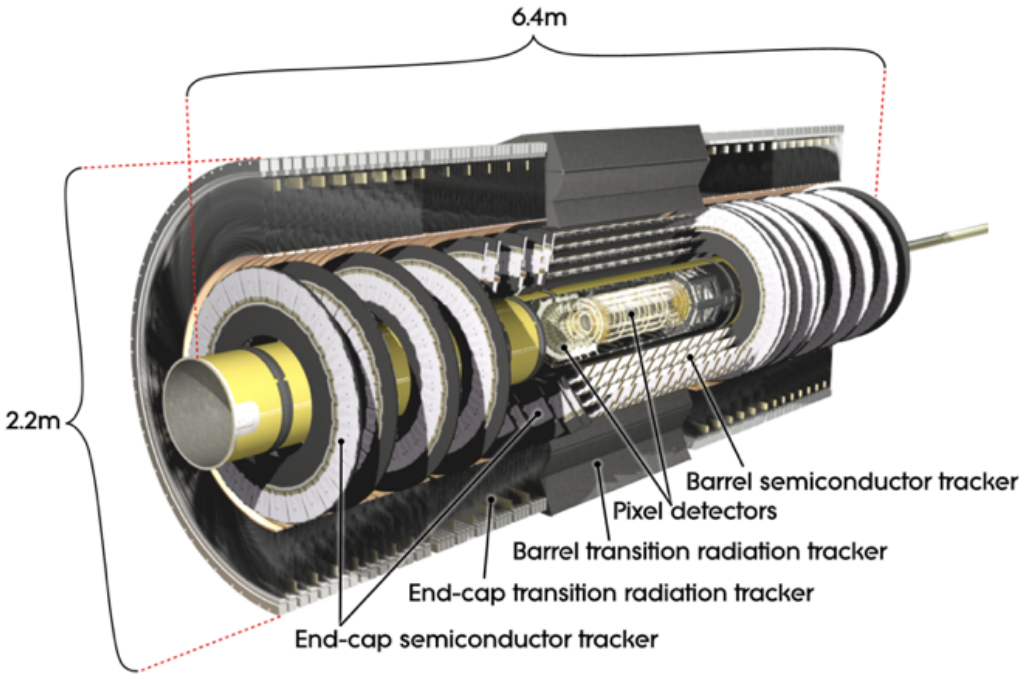

Figure 2.4.: Cut-away view of the ATLAS inner detector [21].

enables radially extended track reconstruction up to $|\eta| = 2.0$. The ID system is immersed in a 2 T axial magnetic field and provides charged particle tracking in the range $|\eta| < 2.5$.

Calorimeter

In Figure 2.5, a view of the calorimeter system is shown. This detector is designed to measure the energy loss of the particles that passes through. The calorimeter system covers the pseudorapidity range $|\eta| < 4.9$. Within the region $|\eta| < 3.2$, electromagnetic calorimetry is provided by barrel and endcap high-granularity lead/liquid-argon (LAr) electromagnetic calorimeters, with an additional thin LAr presampler covering $|\eta| < 1.8$, to correct for energy loss in material upstream of the calorimeters. Hadronic calorimetry is provided by the steel/scintillating-tile calorimeter, segmented into three barrel structures within $|\eta| < 1.7$, and two copper/LAr hadronic endcap calorimeters. The high $|\eta|$ region, $3.2 < |\eta| < 4.9$, is covered by forward copper/LAr and tungsten/LAr calorimeter (FCal) modules optimized for electromagnetic and hadronic measurements respectively.

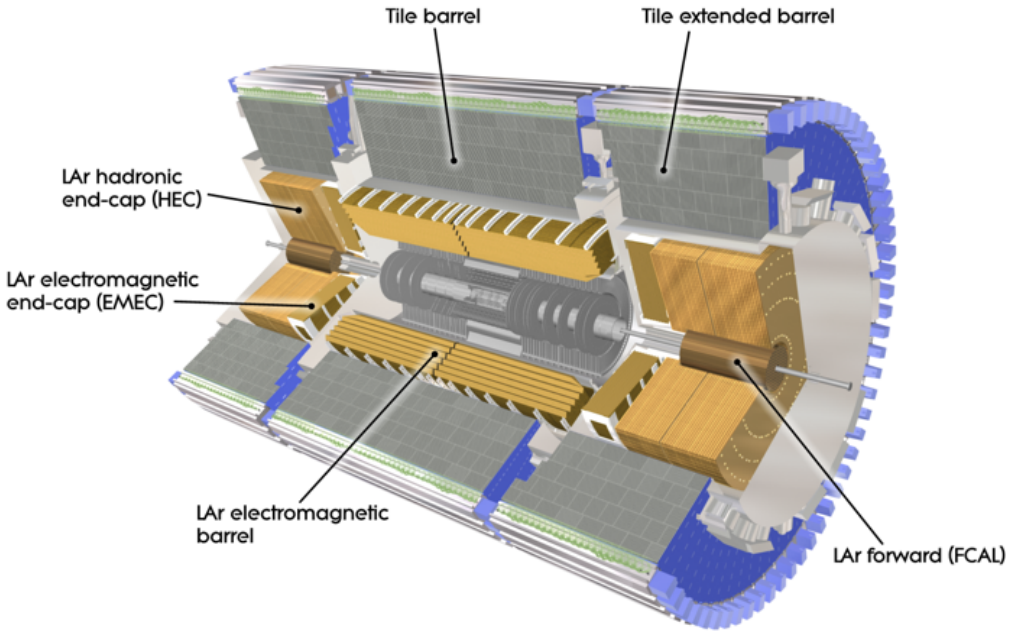

Figure 2.5.: Cut-away view of the ATLAS calorimeter system [21].

Muon spectrometer

The muon spectrometer comprises separate trigger and high-precision tracking chambers measuring the deflection of muons in a magnetic field generated by superconducting air-core toroids. The precision chamber system covers the region $|\eta| < 2.7$ with three layers of monitored drift tubes, complemented by cathode strip chambers in the forward region, where the background is highest. The muon trigger system covers the range $|\eta| < 2.4$ with resistive plate chambers in the barrel, and thin gap chambers in the endcap regions. Figure 2.6 shows the muon spectrometer system.

Zero degree calorimeter

In addition to the muon trigger, two triggers are used in Pb+Pb collisions to select minimum-bias events. These are based on the presence of a minimum amount of transverse energy in all sections of the calorimeter system ($|\eta| < 3.2$) or, for events which do not meet this condition, on the presence of energy deposits in both zero-degree calorimeters (ZDCs), which are primarily sensitive to spectator neutrons in the region $|\eta| > 8.3$.

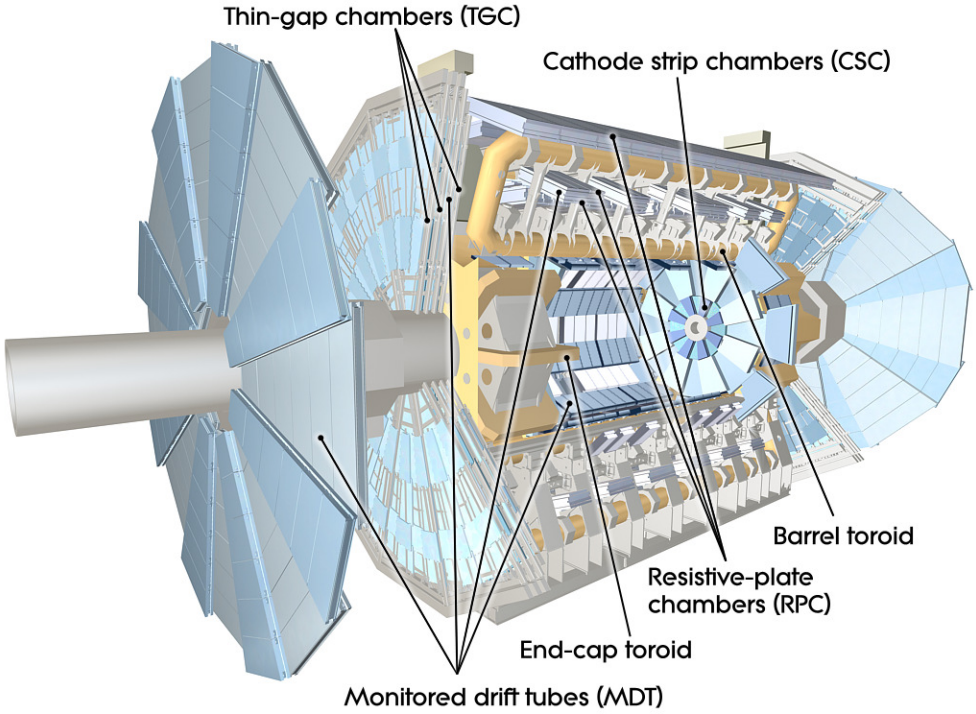

Figure 2.6.: Cut-away view of the ATLAS muon spectrometer system [21].

Trigger system

A two-level trigger system is used to select events [22]. The Level-1 trigger is implemented in hardware and uses a subset of detector information to reduce the event rate to a design value of at most 100 kHz. This is followed by a software-based trigger level which reduces the event rate to about 1 kHz.

2.3. Data and event selection

Data from Pb+Pb collisions at $\sqrt{s_{\text{NN}}} = 5.02$ TeV were recorded by the ATLAS experiment in 2015. Events were collected using a trigger requiring at least two muons, both with $p_{\text{T}}^{\mu} > 4$ GeV. This muon triggered dataset has an integrated luminosity of 0.42 nb^{-1}. In the offline analysis, reconstructed muons are required to satisfy the *tight* muon working point ignoring the TRT requirements [23], have $p_{\text{T}}^{\mu} > 4$ GeV, $|\eta| < 2.4$, and be matched to the muon reconstructed at the trigger level. In addition, muon pairs are required to have pair $p_{\text{T}} > 9$ GeV (in this work p_{T} refers as the transverse momentum of the dimuon system), rapidity $|y| < 2$ and be in the invariant mass range $2.6 < m_{\mu\mu} < 3.5$ GeV. In addition to the muon triggered event sample, a minimum-bias triggered event sample and Monte Carlo (MC) simulated event samples were used for studies of the detector performance. Minimum-bias events are selected by requiring that they pass at least one of the two minimum-bias triggers [2]. Prompt ($\mathrm{pp} \to J/\psi \to \mu\mu$) and non-prompt ($\mathrm{pp} \to \mathrm{b\bar{b}} \to J/\psi \to \mu\mu$) samples of J/ψ were produced using Pythia 8.212 for event generation and Photos for electromagnetic radiation corrections [24, 25]. The A14 set of tuned parameters [26] is used together with CTEQ6L1 parton distribution function set [27]. The response of the ATLAS detector was simulated using Geant4 [28, 29]. Simulated events are overlaid on a sample of minimum-bias Pb+Pb events produced with HIJING to replicate the high-multiplicity environment of heavy-ion collisions [30].

2.4. Centrality definition

To characterise the Pb+Pb collision geometry, events are classified into centrality intervals determined by the summed transverse energy deposited in the FCal, $\sum E_{\text{T}}^{\text{FCal}}$, in each event. Centrality intervals are defined according to successive percentiles of the $\sum E_{\text{T}}^{\text{FCal}}$ distribution ordered from the most central (the highest $\sum E_{\text{T}}^{\text{FCal}}$, the smallest impact parameter) to the most peripheral collisions (the lowest $\sum E_{\text{T}}^{\text{FCal}}$, the largest impact parameter). The average number of nucleons participating in the collision, $\langle N_{\text{part}} \rangle$, is calculated using a Glauber model analysis of the $\sum E_{\text{T}}^{\text{FCal}}$ distribution [31, 32]. The centrality intervals used in this analysis are quoted together with $\langle N_{\text{part}} \rangle$ in Table 2.1. Figure 2.7 shows the E_{T} distribution in minimum-bias events and the ranges which correspond to these centrality selections.

The centrality intervals are defined by values of $\sum E_{\text{T}}^{\text{FCal}}$. These intervals have an uncertainty associated primarily to the effect of trigger and event selection inefficiencies as well as backgrounds in the most peripheral $\sum E_{\text{T}}^{\text{FCal}}$ intervals [14, 33]. To test the sensitivity of the results to this uncertainty, modified centrality intervals are used. In table 2.2 the $\sum E_{\text{T}}^{\text{FCal}}$ cuts that define each centrality class are defined together with systematic variations.

Centrality	$\langle N_{\text{part}} \rangle$
0 – 20%	311.4 ± 2.6
20 – 40%	160.3 ± 2.7
40 – 60%	70.5 ± 2.2
0 – 60%	135.6 ± 2.0

Table 2.1.: The average number of participating nucleons, $\langle N_{\text{part}} \rangle$ values with their total uncertainties in each centrality interval used in this analysis.

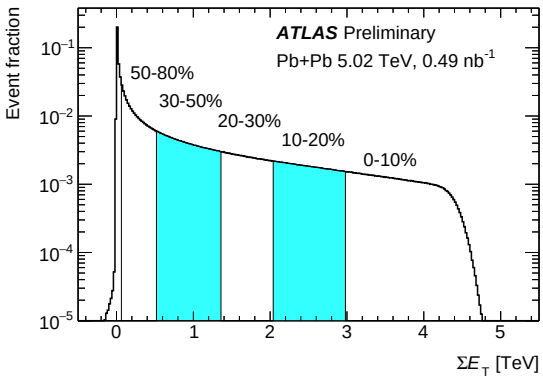

Figure 2.7.: Measure $\sum E_{\text{T}}^{\text{FCal}}$ distribution in minimum-bias Pb+Pb collisions at $\sqrt{s_{\text{NN}}}$ = 5.02 TeV. Alternated shaded and unshaded regions from the large E_{T}-end of the distribution denote increasing centrality intervals [14].

Centile	Sum E_{T} [TeV] (nominal)	Sum E_{T} [TeV] (down)	Sum E_{T} [TeV] (up)
80 %	0.063719	0.058527	0.069136
60 %	0.289595	0.276461	0.302826
40 %	0.87541	0.855791	0.894902
20 %	2.04651	2.0277	2.06495

Table 2.2.: Definition of centrality cuts as a function of E_{T}. Variations used for the definition of the limits of the centrality classes to evaluate systematic uncertainties are also shown.

2.5. Data analysis

The J/ψ v_2, the second order coefficient of the Fourier decomposition of the angular distribution, is estimated using the event-plane method [18]. The event-plane angle is estimated by its second order harmonic, Ψ_2, using the distribution of transverse energy deposited in the forward calorimeters. Similar methods are described in detail for previous azimuthal anisotropies analyses of charged hadrons with the ATLAS detector [13, 34, 14]. To reduce autocorrelations in the event-plane analysis, v_2 is measured by correlating J/ψ with positive (negative) pseudorapidity with the event-plane angle measured using the FCal in the negative (positive) η-region. The prompt and non-prompt J/ψ yields are obtained using two-dimensional fits of the invariant mass and pseudo-proper time. The azimuthal distributions of the prompt and non-prompt yields are fitted simultaneously to obtain the elliptic flow coefficients.

2.5.1. Event-plane method, calibration and resolution

The n-order harmonic of the event-plane angle is determined using measurements of transverse energy deposits in each FCal system positioned at $\eta > 3.2$ and $\eta < -3.2$. The flow vector is defined as:

$$\boldsymbol{q}_n = \sum_{i-\text{towers}} w_i(\cos(n\phi_i)\hat{\boldsymbol{x}} + \sin(n\phi_i)\hat{\boldsymbol{y}}), \tag{2.4}$$

where ϕ_i is the azimuthal coordinate of the i^{th} calorimeter tower and w_i is a weight that equals the transverse energy (E_{T}) deposited in the calorimeter tower. It is determined in both the positive and negative η-regions. Then event-plane angle is then determined as:

$$n\Psi_n = \tan^{-1}\left(\frac{\boldsymbol{q}_n \cdot \hat{\boldsymbol{y}}}{\boldsymbol{q}_n \cdot \hat{\boldsymbol{x}}}\right). \tag{2.5}$$

In this study we restrict to $n = 2$.

Event-plane calibration

Recentering To ensure the uniformity of the event-plane angle distribution, the raw flow vector is corrected by subtracting its mean value, obtained by averaging over all events in a given centrality interval, as:

$$\boldsymbol{q}_2 = \boldsymbol{q}_2^{\text{raw}} - \langle \boldsymbol{q}_2^{\text{raw}} \rangle. \tag{2.6}$$

These *calibration coefficients* are calculated for each side of the detector independently to account for potential differences. The value of components of $\boldsymbol{q}_2$ are shown in Figure 2.8 for a single run as a function of E_{T}. The values are taken as the average over E_{T}. The dependence observed at low E_{T}, corresponding approximately to the centrality class 60 – 80% is ignored,

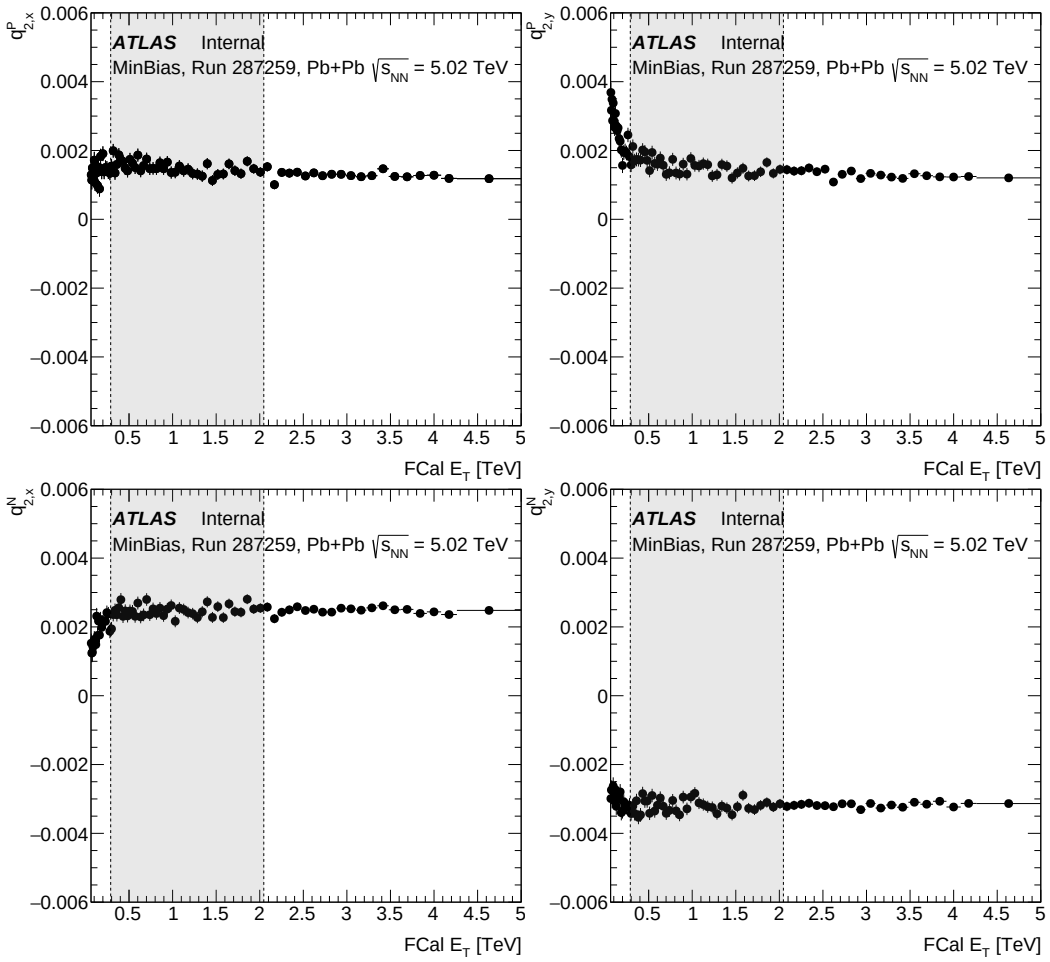

Figure 2.8.: Components of the elliptic flow vector, $\boldsymbol{q}_2$, for the positive (top) and negative (bottom) side of the detector measured for Run 287259. The shaded area represents the 20 – 60% centrality class used to evaluate the average of these coefficients on a narrower E_T range for assessing systematics. The nominal average is performed over the whole centrality interval.

but its effect is assessed as a systematic varation. The systematic variation considers averaging over E_T for the centrality class 20 – 60% (shown with a shaded area in Figure 2.8), removing the events from the low E_T region, and ignoring also the high E_T region. The effect of this different selection for the calibration coefficients is found to be negligible.

The run-by-run dependence of the correction coefficients is shown in Figure 2.9. The result includes the systematic uncertainty discussed in the previous paragraph, and shows that there is no run-by-run dependence on the coefficients within uncertainties. A fit to a constant shows that run-by-run averages are consistent with a constant, within uncertainties, for the whole dataset. The value of the χ^2/dof is improved when the fitted uncertainties are taken as the total uncertainty, statistical and systematic, added in quadratures.

Since the mean values $\langle \boldsymbol{q}_2^{\text{raw}} \rangle$ are found to be independent of the collision centrality, the $\langle \boldsymbol{q}_2^{\text{raw}} \rangle$ averaged over all analysed events (centrality 0 – 60%) is used.

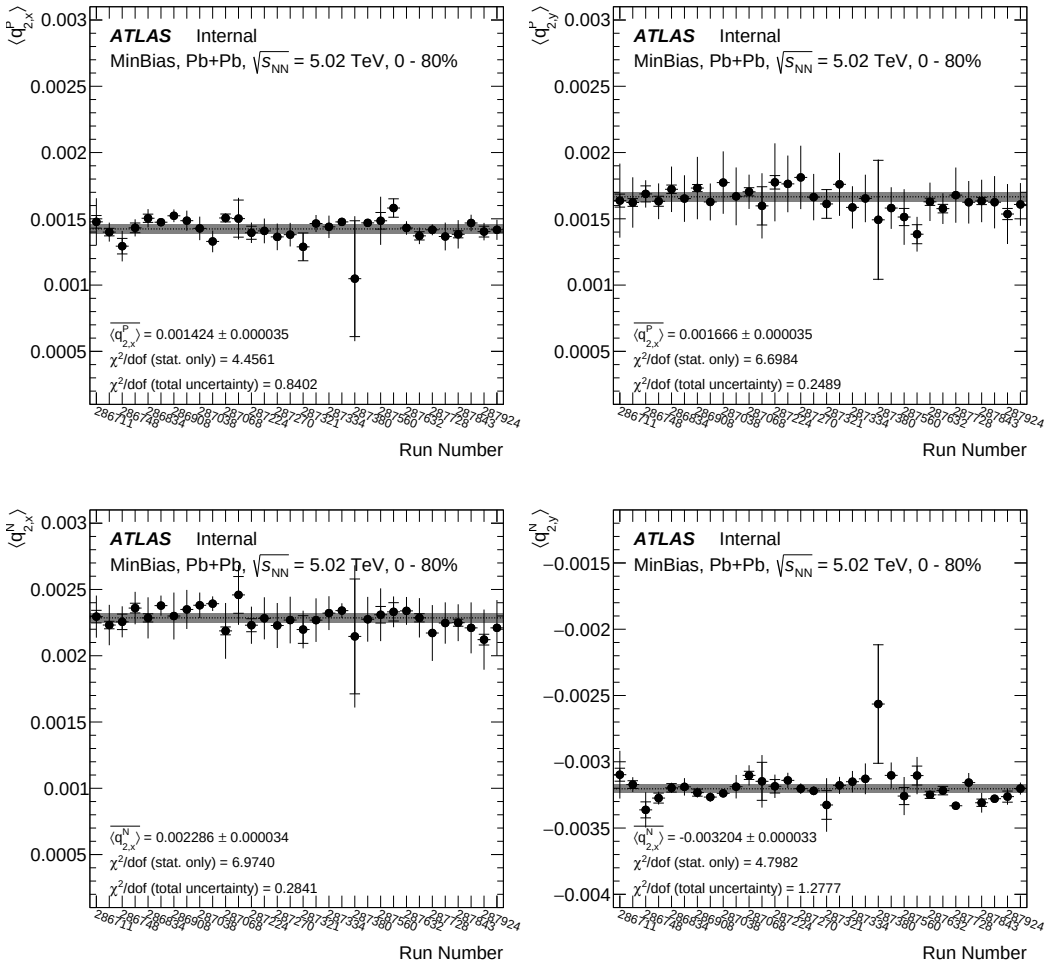

Figure 2.9.: Average value of the components of the elliptic flow vector, $\boldsymbol{q}_2$, for each run. The total uncertainty is shown as an error bar, added in quadratures the statistical error. The statistical error of each point is shown with ending error bars. A fit to a constant shows that run-by-run averages are consistent with a constant, within uncertainties, for the whole dataset. The value of the χ^2/dof is improved when the fitted uncertainties are taken as the total uncertainty (statistical + systematic), added in quadratures.

Flattening Then the remaining modulations on the event-plane angle distribution are removed by including a shift [18] to the event-plane angle calculated after recentering:

$$n\Psi_n = n\Psi_n\Big|_{\text{after recentering}} + n\delta\Psi_n. \tag{2.7}$$

The shift calculated by expanding the remaining modulations of the $n\Psi_n$ distribution using a Fourier decomposition. Therefore the shift is given by:

$$n\delta\Psi_n = \sum_{k=1}^{k_{\max}} \left[A_{nk}\cos(nk\Psi_n) + B_{nk}\sin(nk\Psi_n) \right]. \tag{2.8}$$

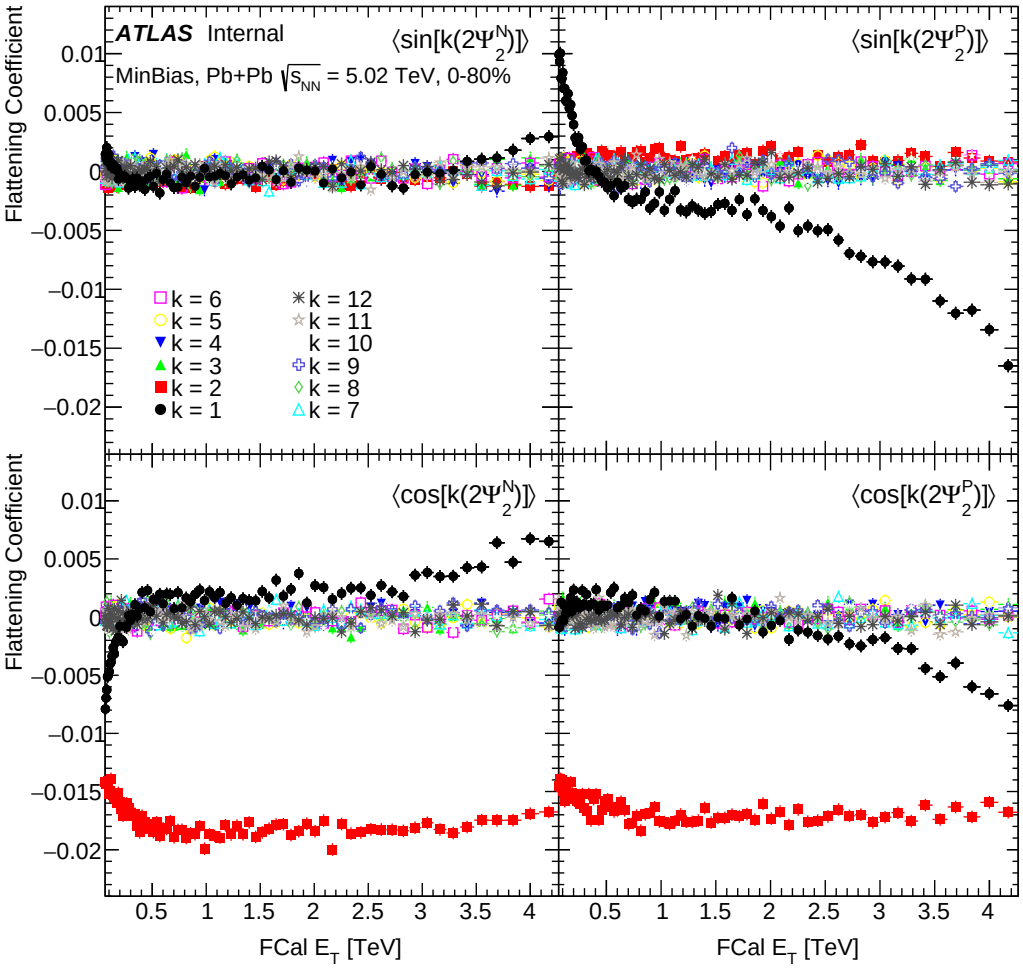

Figure 2.10.: Event-plane flattening coefficients. For $k \leq 2$ the corrections are applied E_T-dependent, while for $k \geq 3$ they are averaged over E_T. These quantities are multiplied by $2/k$ when applying the correction.

By requiring that all components with $nk > n$ vanish, the coefficients are:

$$A_{2k} = -\frac{2}{k}\langle \sin(nk\Psi_n) \rangle \tag{2.9}$$

$$B_{2k} = \frac{2}{k}\langle \cos(nk\Psi_n) \rangle. \tag{2.10}$$

These *flattening coefficients* are shown in Figure 2.10 for the case of interest $n = 2$. For $k \leq 2$ there is a strong dependence on E_T which is considered when applying the correction, while for $k \geq 3$ the average over E_T is used. Contributions from $k \geq 3$ are small and at the same time suppressed as $1/k$. For this analysis $k_{max} = 12$, a variation with $k_{max} = 4$ is used to assess systematic uncertainties and it is found to have a negligible effect on the final flattening, thus it is neglected.

The effect of the recentering procedure is depicted when looking at the distribution of Ψ_2 before and after correction, as shown in Figure 2.11. The first step, which is called recentering, reduces the modulation of Ψ_2 up to 6%, while the second step, which is called flattening, reduces the modulation up to 1%.

In Figure 2.12, the correlation between the event-plane angle on opposites sides of the detector is shown before and after corrections. It can be observed also that the event-plane recentering removes most of the differences between both sides of the detector, and the remaining modulation is removed only after flattening.

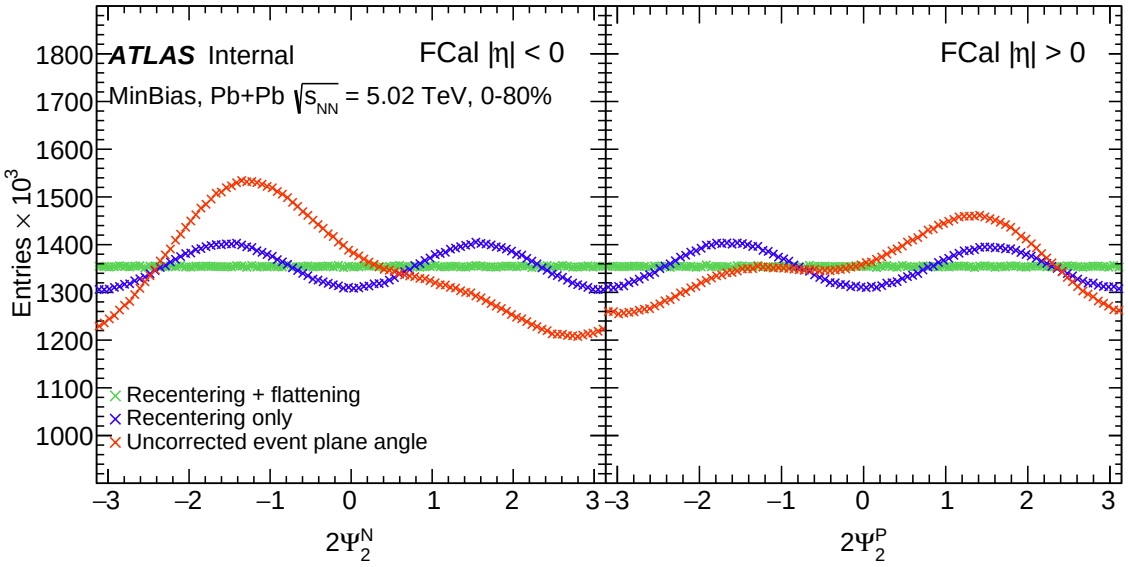

Figure 2.11.: The uncorrected event-plane angle (red), the event-plane angle after recentering (blue), and the event-plane angle after flattenning (green).

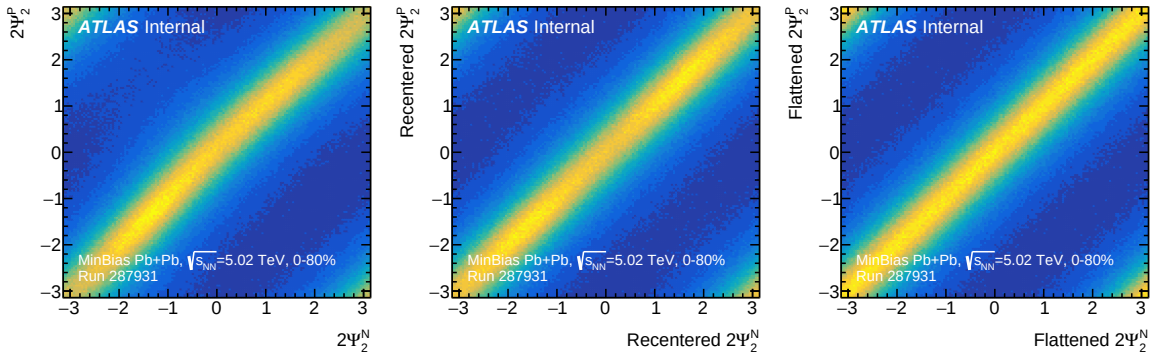

Figure 2.12.: Event-plane angle before (left) and after first (center) and second (right) corrections. The y-axis (x-axis) has the event-plane angle determined on the positive(negative)-η side of the detector. Before any correction the event-plane angle has a small difference in both sides of the detector, this is partially removed after recentering and improved after flattening.

Event-plane resolution

The event-plane angle resolution, R, is determined using the two-sub-event method [18] and the minimum-bias event sample. To evaluate systematic uncertainties the three-sub-event method [18] is used. The resulting event-plane resolution strongly depends on centrality, with worse resolution at low and high $\sum E_{\mathrm{T}}^{\mathrm{FCal}}$ and better values at mid $\sum E_{\mathrm{T}}^{\mathrm{FCal}}$. The resolution is calculated in minimum-bias events in very fine bins of transverse energy. The average value of the resolution in wider bins must account for the different $\sum E_{\mathrm{T}}^{\mathrm{FCal}}$ distribution of the sample of events containing J/ψ candidates. Thus, the event-plane resolution is weighted by the number of J/ψ candidates in a given centrality interval relative to the number of minimum-bias events in the same interval. The values of R for the centrality intervals used in this analysis are shown in Table 2.3. Details are described in the remaining part of this section.

The event-plane angle is determined for each event, and the goodness of this determination depends primarily on the number of particles used in this determination, thus the observed anisotropies are limited to the available statistics to properly resolve the event-plane angle. The flow signal needs to be corrected to obtain its true value as:

$$v_n^{\mathrm{true}} = v_n^{\mathrm{fit}}/R_n, \tag{2.11}$$

where v_n^{fit} is the determined value of v_n from data, and R_n is the n-order event-plane resolution for a given centrality class [18].

The event-plane resolution can be calculated using the event-plane angle determined in different sub-events, separated in η or in different η-windows. The two-subevent method uses the event-plane angle determined on the positive and negative side of the FCal, its value is given by:

$$R_n = \sqrt{\langle \cos(n\Delta\Psi_n)\rangle}, \tag{2.12}$$

where $\Delta\Psi_2$ is the difference between the values of Ψ_2 computed using the FCal modules in the positive and negative η-region of the detector. Equivalently:

$$R_n = \sqrt{\langle \cos(n[\Psi_n^{\mathrm{A}} - \Psi_n^{\mathrm{-A}}])\rangle}. \tag{2.13}$$

Centrality	$\langle N_{\mathrm{part}}\rangle$	R
0 – 20%	311.4 ± 2.6	0.759 ± 0.011
20 – 40%	160.3 ± 2.7	0.871 ± 0.004
40 – 60%	70.5 ± 2.2	0.766 ± 0.006
0 – 60%	135.6 ± 2.0	0.794 ± 0.032

Table 2.3.: The average number of participating nucleons, $\langle N_{\mathrm{part}}\rangle$, and the event-plane resolution, R, values with their total uncertainties in each centrality interval.

Since the FCal is not the only detector systems available to detect the energy deposited by particles, the electromagnetic and hadronic calorimeters can also be used as event-plane detectors and provide a reference to determine the event-plane resolution. The method is referred to as three-subevent method and is defined as:

$$R_n = \sqrt{\frac{\langle \cos(n[\Psi_n^{\mathrm{A}} - \Psi_n^{\mathrm{B}}]) \rangle \langle \cos(n[\Psi_n^{\mathrm{A}} - \Psi_n^{\mathrm{C}}]) \rangle}{\langle \cos(n[\Psi_n^{\mathrm{B}} - \Psi_n^{\mathrm{C}}]) \rangle}} \tag{2.14}$$

The baseline definition of the sub-event A is one of the FCal hemispheres, in the positive and negative rapidity regions (which is where one investigates the event-plane resolution), while B and C are defined in different η-windows as shown in Table 2.4 and illustrated in Figure 2.13.

The event-plane angle measured in each sub-event must be recentered and flattened independently and follows the same procedures as described for the event-plane calibration with the recentering and flattening procedures.

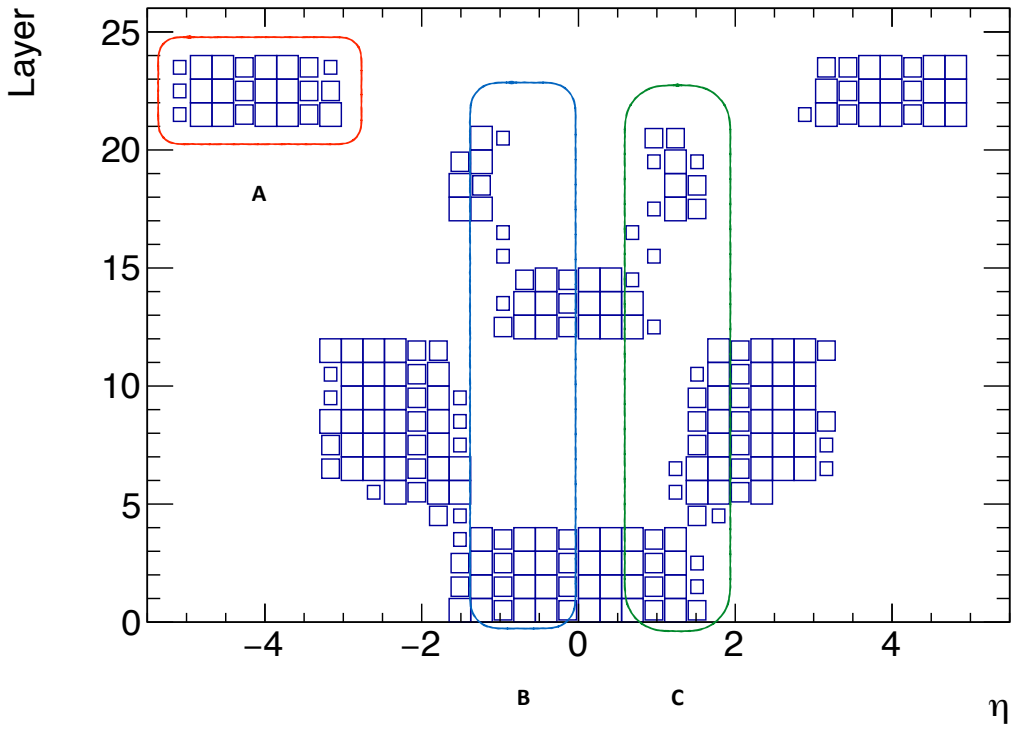

Figure 2.13.: Illustration of the definition of the η-windows for the calculation of the event-plane resolution using the three-subevent method.

While the two-subevent method gives a single value for the event-plane resolution, the three-subevent method returns a value for the event-plane resolution on each FCal (in the negative and positive η-regions). For this reason, the event-plane resolution is taken from the two-subevent method, and the three-subevent method is left for assessing systematic variations and cross-check of the results.

Sub-event	FCal ($\eta > 0$)		FCal ($\eta < 0$)	
	$\eta_{\min}$	$\eta_{\max}$	$\eta_{\min}$	$\eta_{\max}$
A	3.2		-3.2	
B	0.5	2	-2	-0.5
C	-1.5	0	0	1.5

Table 2.4.: Definition of the η-windows used for the three-subevent method for the calculation of the event-plane resolution. An η-separation is introduced between subevents to avoid potential biases in the determination of the event-plane angle.

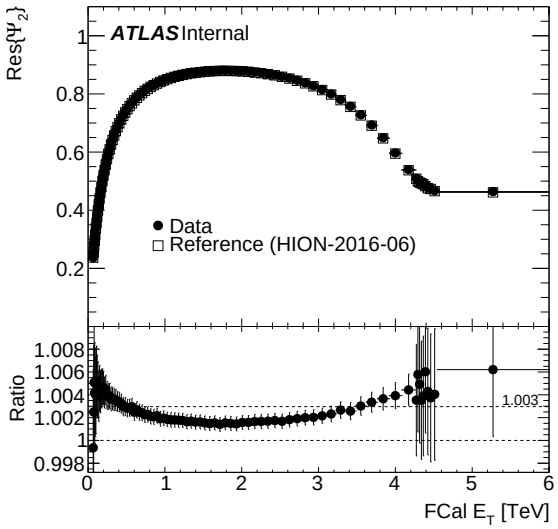

Figure 2.14.: Event-plane resolution as a function of FCal E_{T} in fine centrality intervals. The result obtained for this analysis is compared with the one calculated for HION-2016-06 independently. The ratio indicates a difference up to 0.6%.

The measurement of the event-plane resolution is performed as a function of FCal E_{T} to account for the collision geometry dependence of this quantity. In Figure 2.14 the result of the event-plane resolution for the two-subevent method is shown and compared with the same calculation performed for other analysis (See Int. Note of HION-2016-06). Both results are in great agreement and represent an excellent cross-check for the analysis procedure. The small difference spotted between the two analysis can be neglected; the sources of this difference can include binning conventions, histogram profiling, run-by-run event-plane flattening and event selection.

In Figure 2.15 the result of the tree-subevent method is presented and reveals a great consistency with the results for the event-plane resolution with the two-subevent method with differences up to 1.5%. In this case, the difference between both methods for calculating the event-plane resolution is assigned as a systematic uncertainty. Also in Figure 2.15, a different set of centrality selection is shown. This consist of small variations on the cut definitions for each

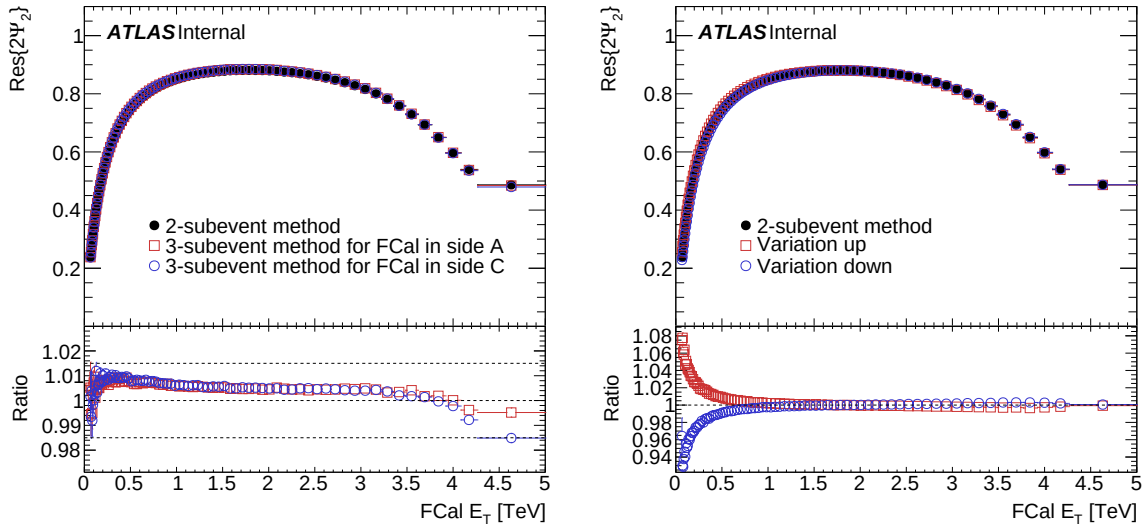

Figure 2.15.: (Right) Event-plane resolution with the two-subevent and the three-subevent method; the ratio indicates a difference up to 1.5%. (Left) Event-plane resolution with the two-subevent method for different centrality classes definitions. The centroids in the up/down variations are shifted to match the nominal bins.

centrality class (see Table 2.2). For example, the centrality class $40-60\%$ is defined as:

$$0.289595^{+0.013231}_{-0.013135} < E_{\mathrm{T}} < 0.875410^{+0.019492}_{-0.019619}\ \mathrm{TeV},$$

where the subscripts and superscripts define systematic variations on the centrality cuts definitions. This changes are computed for the two-subevent method and it is observed that the differences are again subtle and only sums up to 8% in very peripheral collisions. The difference is also assigned as a systematic uncertainty on the event-plane resolution.

Event-plane resolution weighting Since the event-plane angle is reconstructed using the azimuthal distribution of the transverse energy deposited in the calorimeters, the event-plane resolution relies on the energy sampling that the calorimeters have. The corrections are always computed using minimum bias events, but the J/ψ analysis is performed using a data stream with a reduced amount of events at low-E_{T} (HardProbes stream), with a different the E_{T} sampling. The effect is depicted in Figure 2.16.

The measurement is performed in wide centrality classes, thus the resolution must include the distribution of events as recorded in the HardProbes stream that also reflect the E_{T}-distribution of J/ψ events. The HardProbes resolution is calculated averaging the MinBias resolution weighted by the number of HardProbes events in that centrality class relative to the number of MinBias events in the same centrality class. The value of the event-plane resolution for a given

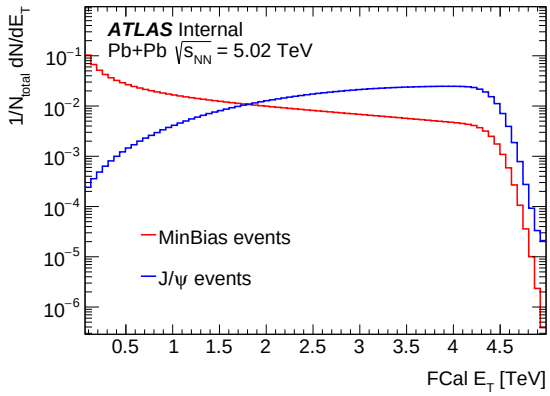

Figure 2.16.: FCal E_T distributions is MinBias and HardProbes events normalized to the total number of events in each data stream.

centrality class will be given by:

$$R_2(\Delta E_T)^{\text{HardProbes}} = \sum_{\text{events}} \frac{N(\text{HardProbes events in } \Delta E_T)}{N(\text{MinBias events in } \Delta E_T)} R_2(E_T)^{\text{MinBias}} \tag{2.15}$$

The result of this procedure is shown in Figure 2.17 for 10% wide centrality classes (in E_T units) and it shows the difference between the event-plane resolution computed in Minbias and Hardprobes events, and in Minbias events weighted to Hardprobes E_T-distribution. As expected, the biggest difference is present at low-E_T, where both distributions are more different. The difference between Hardprobes and Minbias weighted resolution is assigned as a systematic uncertainty.

The average value of the event-plane resolution, integrated over the whole centrality range of this analysis, is:

$$R_2(0-60\%) = 0.7938 \pm 0.0002 \text{ (statistical)} \pm 0.0318 \text{ (systematic)}.$$

In Figure 2.17 the results for the event-plane resolution in bins of 20% width is shown together with the systematic uncertainties associated with its value.

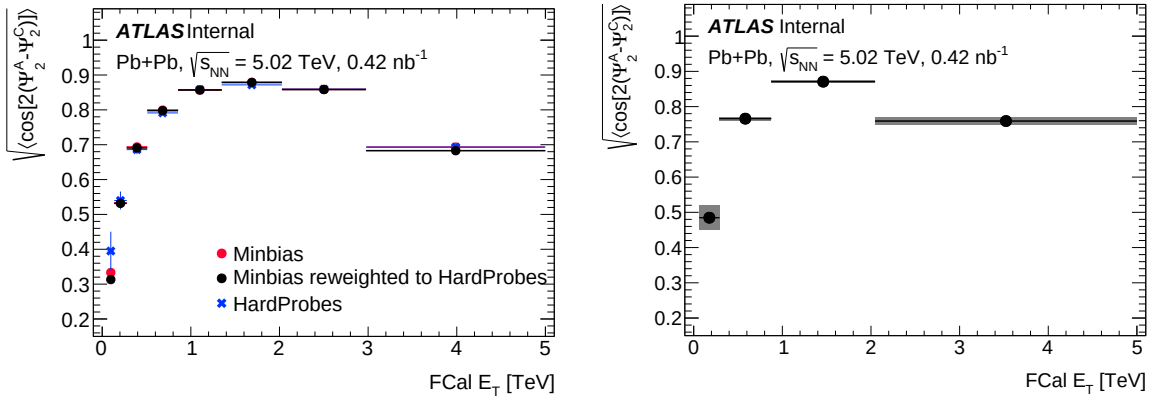

Figure 2.17.: (Left) Event-plane resolution computed in MinBias and Hardprobes events, and in Minbias weighted to Hardprobes E_T-distribution. (Right) Centrality dependence of the event-plane resolution in centrality bins of width 20%, from 80% to 0% (left to right) shown as a function of FCal E_T. Statistical uncertainties are shown with error bars (smaller than the plotting symbol) and systematic uncertainties with shaded boxes.

2.5.2. Detector performance

To account for the detector effects, each muon pair is corrected for trigger efficiency, ϵ_{trig}, reconstruction efficiency, ϵ_{reco}, and detector acceptance, A. These three quantities form a per-dimuon weight:

$$w^{-1} = A \times \epsilon_{\text{trig}} \times \epsilon_{\text{reco}}. \tag{2.16}$$

Trigger and reconstruction efficiencies are studied using the tag-and-probe method [35] in data and in MC simulation as a function of the muon p_{T}^{μ} and η^{μ}. Reconstruction efficiency increases from low to high p_{T}^{μ} and decreases from central to forward pseudorapidity, becoming constant at $p_{\text{T}}^{\mu} > 6$ GeV with a maximum efficiency of about 90%. Trigger efficiency increases from low to high p_{T}^{μ} and from central to forward pseudorapidity, increasing from 50% to 85% between the lowest and highest p_{T}^{μ}. The acceptance is studied from MC simulations. It is defined as the probability that the J/ψ decay products fall within the fiducial volume $p_{\text{T}}^{\mu} > 4$ GeV and $|\eta^{\mu}| < 2.4$ and assumes unpolarised J/ψ production [36, 37, 38]. The weight given in Eq. 2.16 is shown in Fig. 2.18 as a function of the transverse momentum of the muon pair p_{T} and rapidity. A detailed description of the performance studies are presented in Ref. [2].

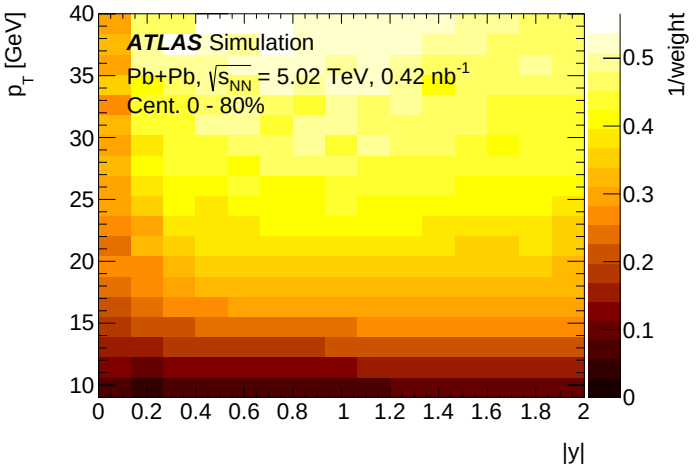

Figure 2.18.: Inverse total weight binned in the dimuon transverse momentum and rapidity for integrated centrality as estimated in MC simulation and corrected for differences between efficiencies in MC and experimental data. Decreases in efficiency at very central rapidity correspond to the $|\eta| < 0.1$ region not covered by the muon detectors. The weight is dominated by the acceptance correction. [2].

2.5.3. Signal extraction

The separation of the prompt and non-prompt J/ψ signals is performed using the pseudo-proper decay time of the J/ψ candidate:

$$\tau_{\mu\mu} = \frac{L_{xy} m_{J/\psi}}{p_{\mathrm{T}}}, \tag{2.17}$$

where L_{xy} is the distance between the position of the dimuon vertex and the primary vertex projected onto the transverse plane, $m_{J/\psi} = 3.096$ GeV is the value of the J/ψ mass [39], and p_{T} is the transverse momentum of the dimuon system.

The corrected two dimensional distribution of the number of events as a function of pseudo-proper time and dimuon invariant mass is used to determine the prompt and non-prompt J/ψ yields. The probability distribution function (PDF) for the fit is defined as a sum of five terms, where each term is the product of functions that depend on the dimuon invariant mass or pseudo-proper decay time. The PDF is written in a compact form as:

$$P(m_{\mu\mu}, \tau_{\mu\mu}) = \sum_{i=1}^{5} N_i f_i(m_{\mu\mu}) \cdot h_i(\tau_{\mu\mu}) \otimes g(\tau_{\mu\mu}), \tag{2.18}$$

where N_i is the normalisation factor of each component, $f_i(m_{\mu\mu})$ and $h_i(\tau_{\mu\mu})$ are distribution functions of the invariant mass, $m_{\mu\mu}$, and the pseudo-proper time, $\tau_{\mu\mu}$, respectively; $g(\tau_{\mu\mu})$ is the resolution function described with a double Gaussian; and the $\otimes$-symbol denotes a convolution. The PDF terms are defined by Crystal Ball (CB) [40], Gaussian (G), Dirac delta (δ), and exponential (E) distributions as specified in Table 2.5. The CB function, $F_{\mathrm{CB}}(m_{\mu\mu})$,

combines a Gaussian core and a power law tail with exponent n, with a parameter α defining the transition between the Gaussian and the power law functions:

$$F_{\mathrm{CB}}(m_{\mu\mu}) = \begin{cases} \dfrac{N(\alpha,n)}{\sqrt{2\pi}\sigma_{\mathrm{CB}}} \exp\left(-\dfrac{(m-m_0)^2}{2\sigma_{\mathrm{CB}}^2}\right), & \text{for } \dfrac{m-m_0}{\sigma_{\mathrm{CB}}} > -\alpha \\ \dfrac{N(\alpha,n)}{\sqrt{2\pi}\sigma_{\mathrm{CB}}} \left(\dfrac{n}{|\alpha|}\right)^n \exp\left(-\dfrac{|\alpha|}{2}\right) \left(\dfrac{n}{|\alpha|} - |\alpha| - \dfrac{m-m_0}{\sigma_{\mathrm{CB}}}\right)^{-n}, & \text{for } \dfrac{m-m_0}{\sigma_{\mathrm{CB}}} \leq -\alpha \end{cases} \tag{2.19}$$

The signal invariant mass shapes are described by the sum of a CB and a single Gaussian with a common mean (m_0). The width term in the CB function (σ_{CB}) is equal to the Gaussian standard deviation (σ_{G}) times a scaling term. The CB left-tail and height parameters (α and n) are fixed from MC studies and variations of the two parameters are considered as part of the fit model systematic uncertainties. A normalization factor $N(\alpha,n)$ [41] is required as function of the left-tail and height parameters:

$$N(\alpha,n) = \frac{\sqrt{2\pi}}{\dfrac{n}{|\alpha|}\dfrac{1}{n-1}\exp\left(-\dfrac{|\alpha|^2}{2}\right) + \sqrt{\dfrac{\pi}{2}}\left(1+\mathrm{erf}\left(\dfrac{|\alpha|}{\sqrt{2}}\right)\right)}, \tag{2.20}$$

where erf is the Gauss error function[b]. The relative fraction of the CB and Gaussian functions, ω, is free in the fit. The prompt background contribution to the invariant mass spectrum follows a nearly flat distribution, and is modeled by an exponential. The non-prompt contribution to the background requires two exponential functions.

The pseudo-proper decay time of the prompt signal is modeled with a Dirac delta function, while the non-prompt signal is described by a single sided exponential. The backgrounds are represented by the sum of one prompt component and two non-prompt components. The prompt background component is described by a Dirac delta function. One of the non-prompt background contributions is described by a single-sided decay model (for positive $\tau_{\mu\mu}$ only), and the other is described by a double-sided decay model accounting for candidates of mis-reconstructed or non-coherent muon pairs resulting from other Drell-Yan muons and combinatorial background. A double Gaussian resolution function, $g(\tau_{\mu\mu})$, is used in convolution with the background and signal terms. These resolution functions have a fixed mean at $\tau_{\mu\mu} = 0$ and free widths.

The important quantities extracted from the fit are: the number of signal candidates, N_{signal}, and fraction of signal that is non-prompt, f_{NP}. These are used to build azimuthal distributions of the prompt and non-prompt yields, as the fits are done in intervals of $2|\phi - \Psi_2|$, p_{T}, y and the collision centrality. Example plots of fit projections are shown in Figure 2.19. Table B.1 has a description of all the internal parameters of mass-lifetime fitting for the signal extraction.

[b]The Gauss error function: $\mathrm{erf}(x) = \frac{1}{\sqrt{\pi}}\int_{-x}^{x} \mathrm{e}^{-t^2}\,\mathrm{d}t$.

i	Type	Source	$f_i(m_{\mu\mu})$	$h_i(\tau_{\mu\mu})$
1	Signal	Prompt	$\omega F_{\mathrm{CB}_1}(m_{\mu\mu}) + (1-\omega)F_{\mathrm{G}_1}(m_{\mu\mu})$	$\delta(\tau_{\mu\mu})$
2	Signal	Non-prompt	$\omega F_{\mathrm{CB}_1}(m_{\mu\mu}) + (1-\omega)F_{\mathrm{G}_1}(m_{\mu\mu})$	$F_{\mathrm{E}_1}(\tau_{\mu\mu})$
3	Background	Prompt	$F_{\mathrm{E}_2}(m_{\mu\mu})$	$\delta(\tau_{\mu\mu})$
4	Background	Non-prompt	$F_{\mathrm{E}_3}(m_{\mu\mu})$	$F_{\mathrm{E}_4}(\tau_{\mu\mu})$
5	Background	Non-prompt	$F_{\mathrm{E}_5}(m_{\mu\mu})$	$F_{\mathrm{E}_6}(\lvert\tau_{\mu\mu}\rvert)$

Table 2.5.: Individual components of the PDF in the default fit model used to extract the prompt and non-prompt contribution for J/ψ signal and background. F_{CB} and F_{G} are the Crystal Ball (CB) and Gaussian (G) distribution functions respectively, ω is the relative fraction of the CB and G terms, F_{E} is an exponential (E) function, and $\delta(\tau_{\mu\mu})$ is the Dirac delta function.

2.5.4. Correlation between prompt and non-prompt yields

The prompt and non-prompt signals are obtained from the fit as:

$$N_{\text{prompt}} = N_{\text{signal}}(1 - f_{\text{NP}}), \tag{2.21}$$

$$N_{\text{non-prompt}} = N_{\text{signal}} f_{\text{NP}}. \tag{2.22}$$

While the total signal and the non-prompt fraction are weakly correlated, approximately less than 1%, an artificial correlation is introduced when transforming these variables to the prompt and non-prompt yields. The sum of both yields is constrained to the total number of signal candidates. An example of the correlation histograms constructed to extract these coefficients is shown in Figure 2.20. The plots show that the correlation between N_{signal} and f_{NP} is negligible, but the derived yields N_{prompt} and $N_{\text{non-prompt}}$ become strongly anti-correlated, due to the non-linear transformation applied.

The transformation used to obtained the prompt and non-prompt J/ψ yields is not a linear transformation, thus it is not possible to derive a transformation for the covariance matrix that outcomes from each fit to the mass and pseudo-proper time for the signal extraction. Therefore, to compute the correlation factor a toy Monte Carlo model is implemented using the same fit model and the output of the fits to data in bins of relative azimuthal angle, p_{T}, rapidity and centrality. The correlation coefficient is obtained in each kinematic bin by fitting the distribution of N_{prompt} and $N_{\text{non-prompt}}$ to a bivariate Gaussian function.

The results for the correlation coefficient as a function of relative azimuthal angle, p_{T}, rapidity and centrality are shown in Figure 2.21. The correlation varies with p_{T} from -18% to -24%; in rapidity from -22% to -16%; and is approximately constant as a function of centrality. The average correlation coefficient is -20% for all slices and azimuthal bins with a variation of about 2%. It is important to note that this correlation is merely due to the procedure used to extract the yields from the invariant mass and pseudo-proper decay time distributions.

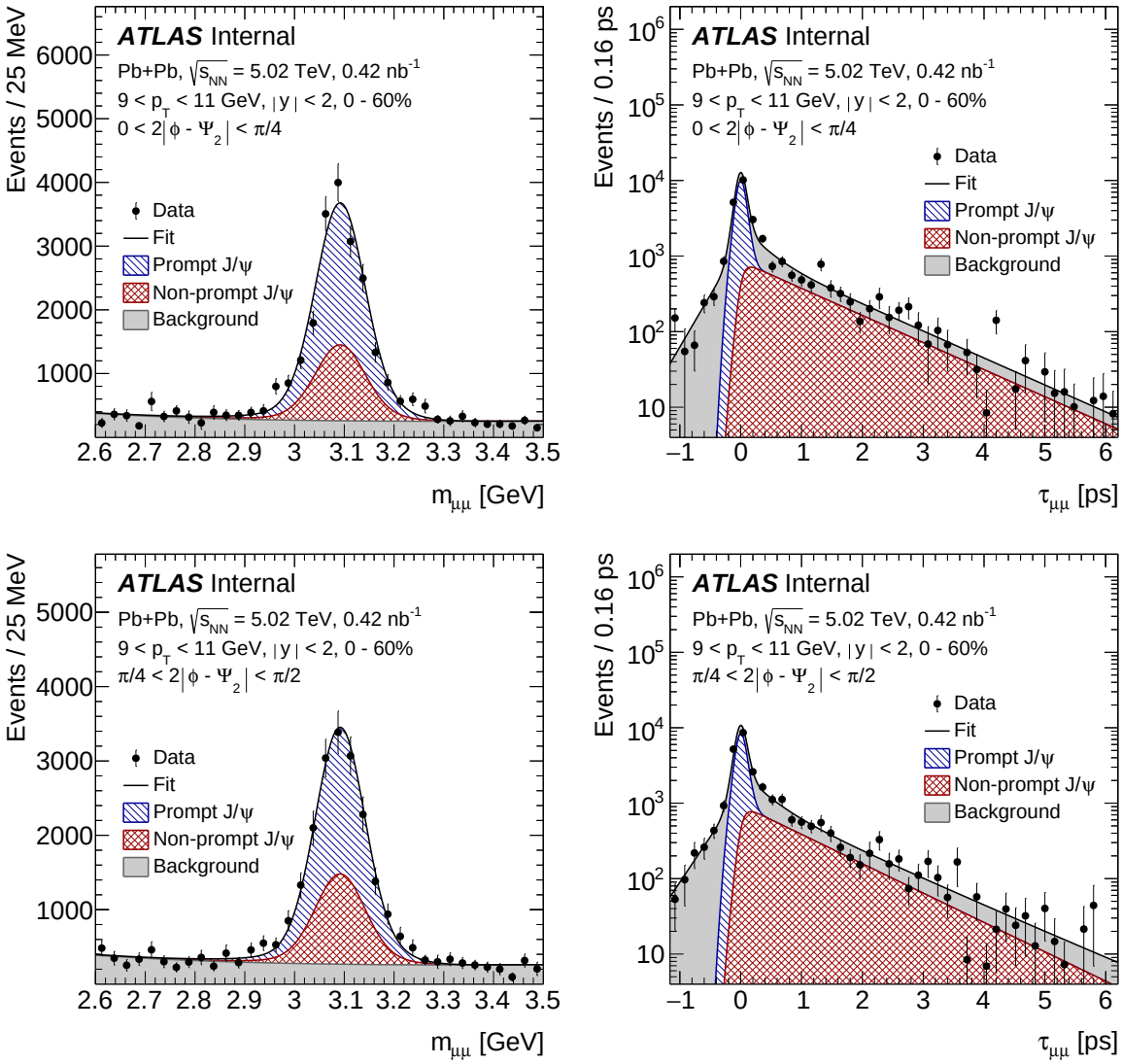

Figure 2.19.: Fit projections of the two-dimensional invariant mass ($m_{\mu\mu}$) and pseudo-proper decay time ($\tau_{\mu\mu}$) for the signal extraction for the azimuthal first azimuthal bin $0 < 2|\phi - \Psi_2| < \pi/4$ (top) and second azimuthal bin $\pi/4 < 2|\phi - \Psi_2| < \pi/2$ (bottom) in the kinematic range $9 < p_{\mathrm{T}} < 11$ GeV, $0 < |y| < 2$ and 0 - 60% centrality.

It is important to remark that the correlation obtained here is accidental; its origin is due to the procedure by which the yields are extracted from the mass and pseudo-proper decay time fit. There is no physical correlation between prompt and non-prompt J/ψ.

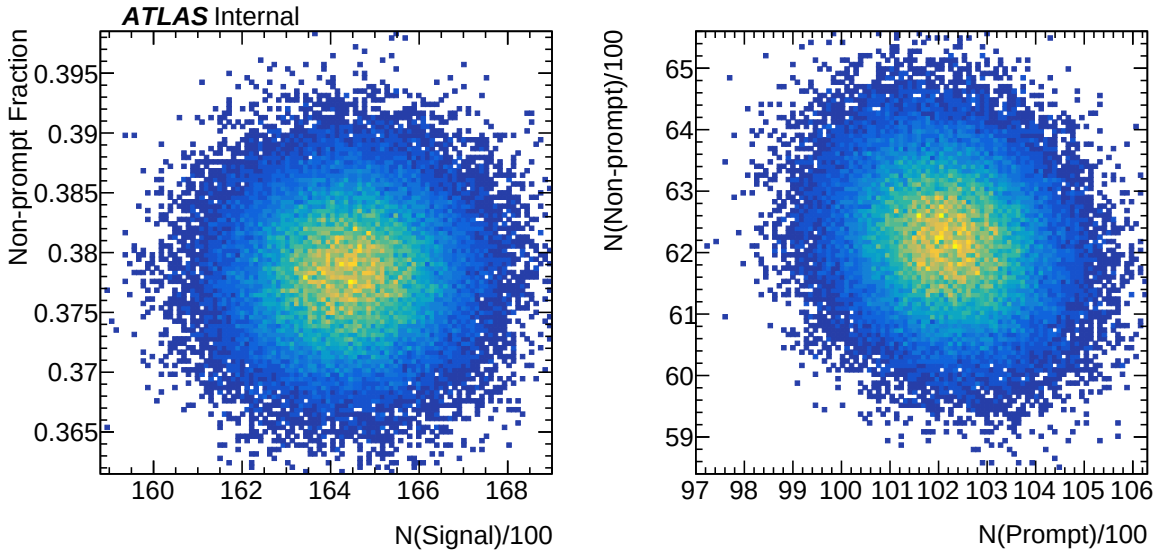

Figure 2.20.: Correlation histograms for the non-prompt fraction, f_{NP}, versus number of signal candidates, N_{signal}, (left panel) and number of prompt J/ψ signal, N_{prompt}, versus number of non-prompt J/ψ signal, $N_{\mathrm{non\text{-}prompt}}$, (right panel), for $9 < p_{\mathrm{T}} < 11$ GeV, $|y| < 2$, $0-80\%$ centrality and $0 < 2|\phi - \Psi_2| < \pi/4$. The figure on the left evidences the weak correlation between the fit variables (less than 1%), while the figure on the right shows how an anti-correlation is introduced when these variables are transformed to be used in the construction of the quantities that will be used.

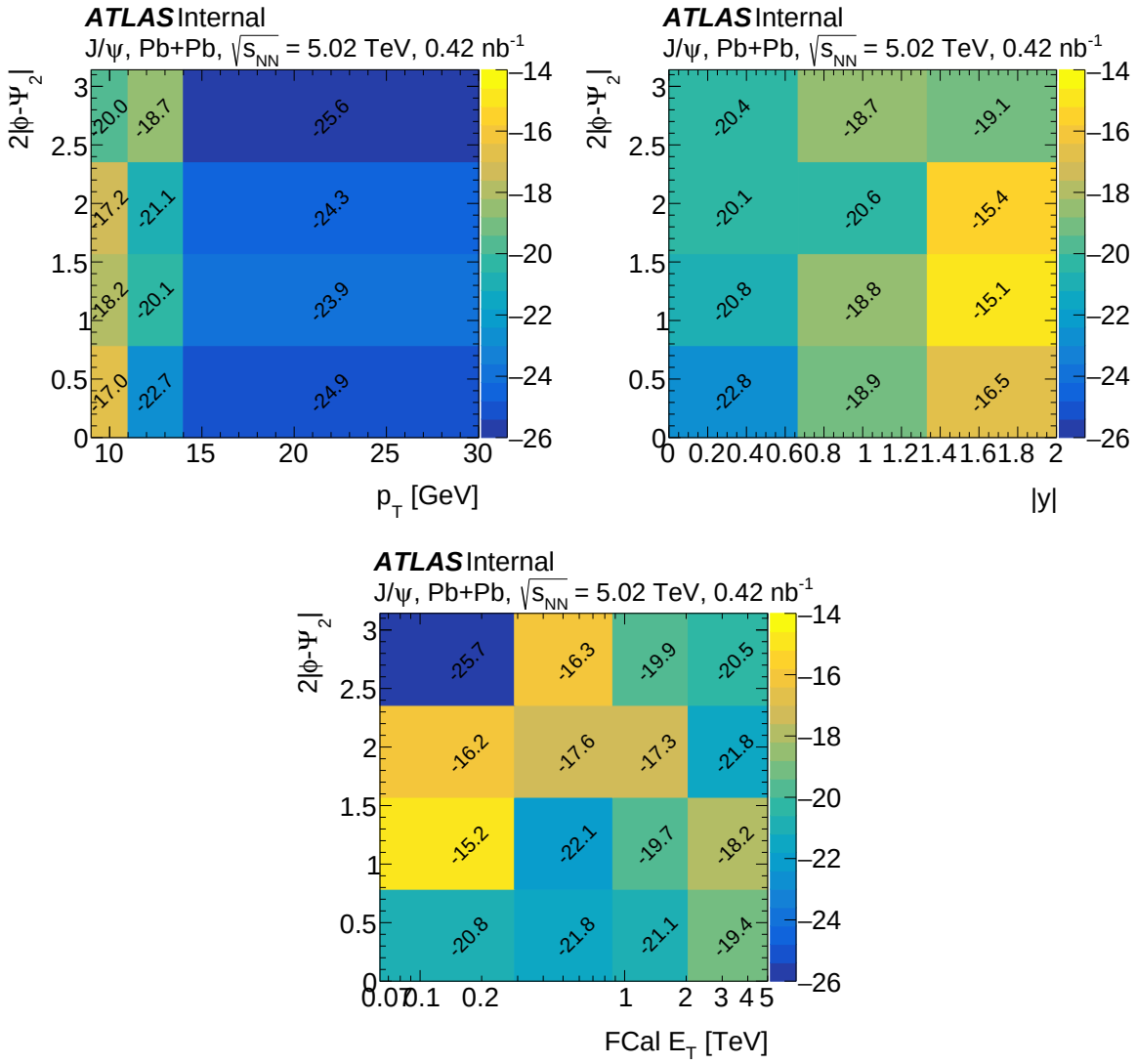

Figure 2.21.: Correlation factors between prompt and non-prompt signals for different slices of p_{T}, rapidity and centrality as a function of $2|\phi - \Psi_2|$ with $N_{\mathrm{MC}} = 50000$. Numbers are expressed in percentage of degree of correlation.

2.5.5. Elliptic flow determination

The elliptic flow coefficient is computed by fitting the prompt and non-prompt yields simultaneously to:

$$\frac{\mathrm{d}}{\mathrm{d}(2|\phi - \Psi_2|)} \begin{pmatrix} N^{\text{prompt}} \\ N^{\text{non-prompt}} \end{pmatrix} = \begin{pmatrix} N_0^{\text{prompt}} \\ N_0^{\text{non-prompt}} \end{pmatrix} \left(1 - 2 \begin{pmatrix} v_2^{\text{prompt}} \\ v_2^{\text{non-prompt}} \end{pmatrix} \cos(2|\phi - \Psi_2|) \right), \tag{2.23}$$

in order to account for the anti-correlation between both signals. This is achieved by minimising the χ^2 function:

$$\chi^2(\boldsymbol{\theta}) = (\boldsymbol{y} - \boldsymbol{\mu}(\boldsymbol{\theta}))^T V^{-1} (\boldsymbol{y} - \boldsymbol{\mu}(\boldsymbol{\theta})), \tag{2.24}$$

where $\boldsymbol{y}$ is the vector of measurements, $\boldsymbol{\mu}(\boldsymbol{\theta})$ is the vector of predicted values with parameters $\boldsymbol{\theta}$, and V is the error matrix. The elements of the vector of measurements are the prompt and non-prompt yields consecutively; the vector of predicted values is given by Eq. 2.23 with the set of free parameters $\{N_0, v_2^{\text{fit}}\}^{\text{prompt}}$ and $\{N_0, v_2^{\text{fit}}\}^{\text{non-prompt}}$ for the modeling of the prompt and non-prompt yields respectively. The elements in the diagonal of V are the yields uncertainties and the off-diagonal terms are the correlation terms between the prompt and non-prompt yields.

An example of the J/ψ yields normalized to the inclusive J/ψ yield and the projection of fit result is shown in Figure 2.22. The simultaneous fit of the prompt and non-prompt yields correctly accounts for the correlation between both signals that arose from the modeling used for the signal extraction. The correlation between the fit parameters as result of the simultaneous fit procedure is shown in Figure 2.23. In a final step, the fitted value of v_2^{fit}, is corrected for the event-plane resolution:

$$v_2 = v_2^{\text{fit}} / R_2. \tag{2.25}$$

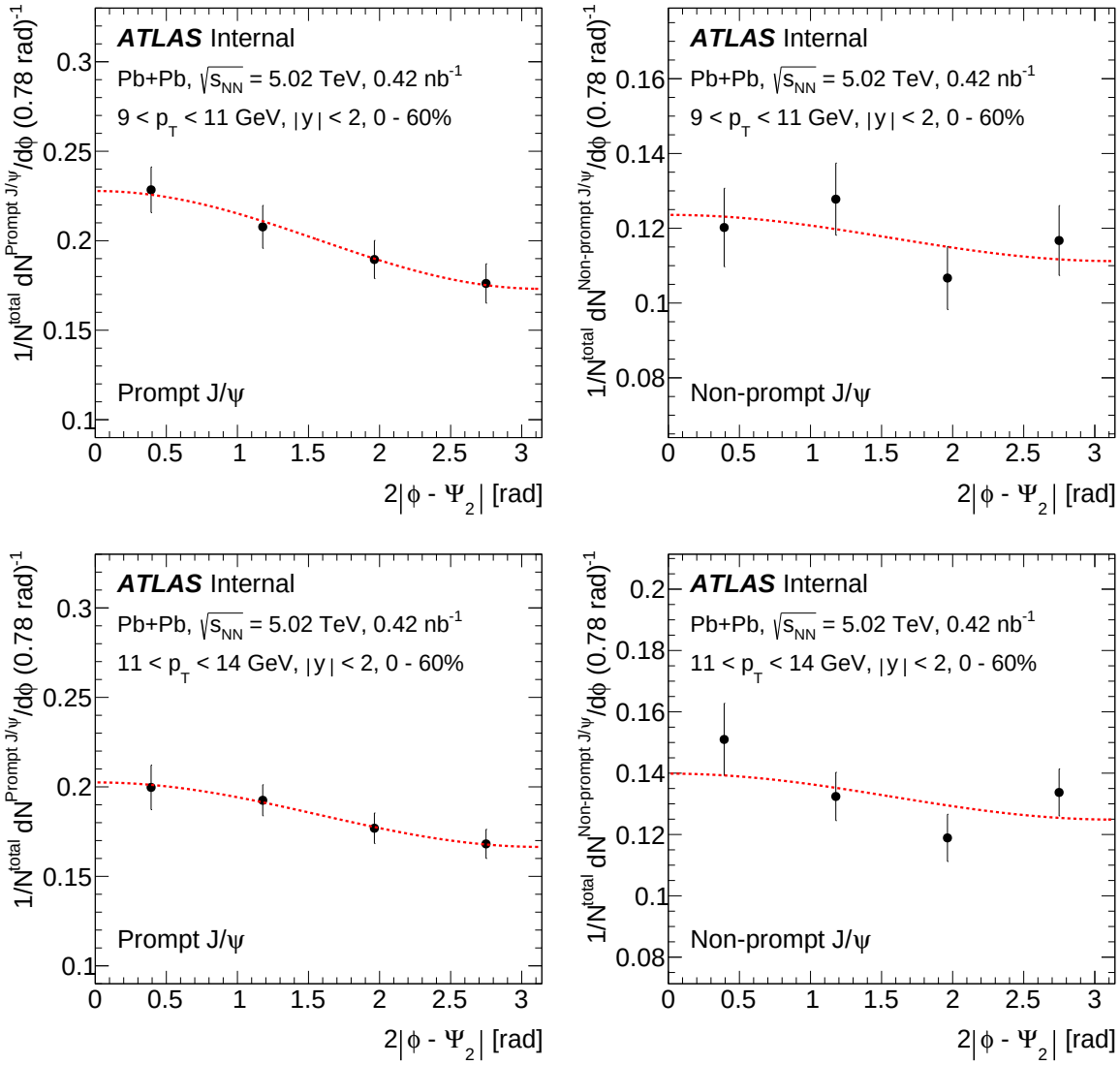

Figure 2.22.: The azimuthal distribution of prompt (left) and non-prompt (right) J/ψ yields for the first and second p_{T} bin studied. The yields are normalized to the inclusive J/ψ signal and the error bars are fit uncertainties associated to the signal extraction. The red line is the result of the simultaneous fit used to compute v_2.

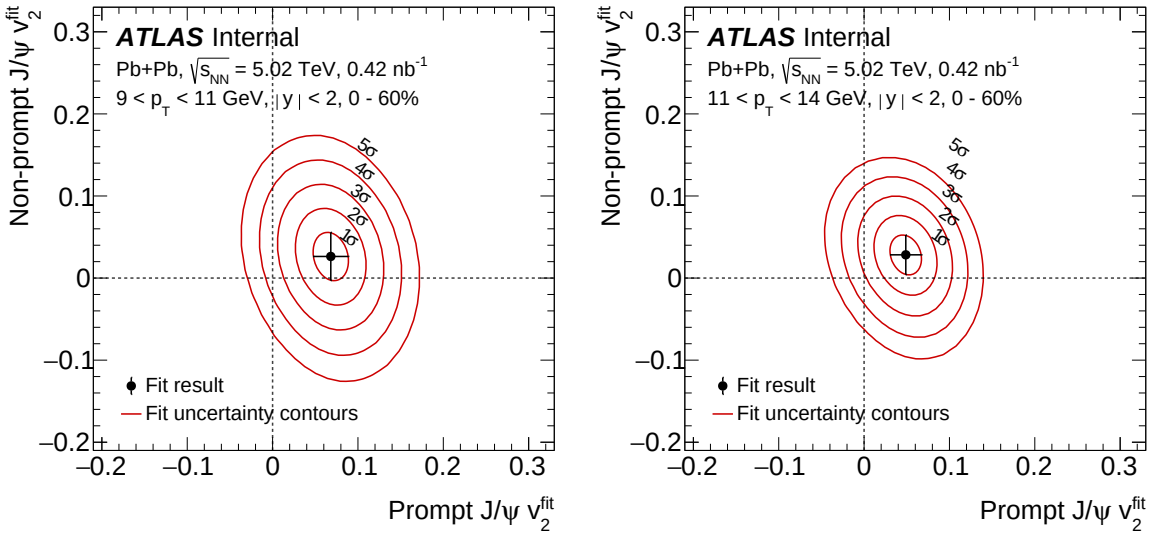

Figure 2.23.: The error analysis for the fitted values of the prompt and non-prompt J/ψ v_2 for the first and second p_{T} bins. Each contour line represents 1σ in the error definition of the fit parameters. For the first p_{T} bin, prompt J/ψ v_2 has a significance of 3σ and non-prompt J/ψ has a significance of 1σ.

2.5.6. Systematic uncertainties

The systematic uncertainties of this measurement are classified into three groups: (a) related to the centrality definition, (b) related to the estimation of the event-plane, and (c) related to the extraction of the signal. The assigned systematic uncertainty from each source is defined in each bin of p_{T}, rapidity or centrality as the root mean square of the difference between the nominal and varied values of the elliptic flow coefficient.

Related to the centrality definition

The centrality intervals are defined by values of $\sum E_{\mathrm{T}}^{\mathrm{FCal}}$. These intervals have an uncertainty associated primarily to the effect of trigger and event selection inefficiencies as well as backgrounds in the most peripheral $\sum E_{\mathrm{T}}^{\mathrm{FCal}}$ intervals [14, 33]. To test the sensitivity of the results to this uncertainty, modified centrality intervals are used, and the analysis is repeated. These changes affect the number of muon pairs entering the signal fitting procedure and thus have an impact on the final value of v_2. For the v_2 measurements as a function of p_{T} or rapidity the uncertainty is about 2% for both prompt and non-prompt J/ψ v_2, while for the centrality dependence this source contributes a 10% systematic uncertainty to both v_2 measurements. In Figure 2.24 the impact of modifying the definition of the centrality cuts are shown for the centrality dependence of prompt and non-prompt J/ψ v_2. The first bin in E_{T}, corresponding to the 60-80% centrality interval is neglected in the calculation of the RMS calculated for the value of the systematic uncertainty.

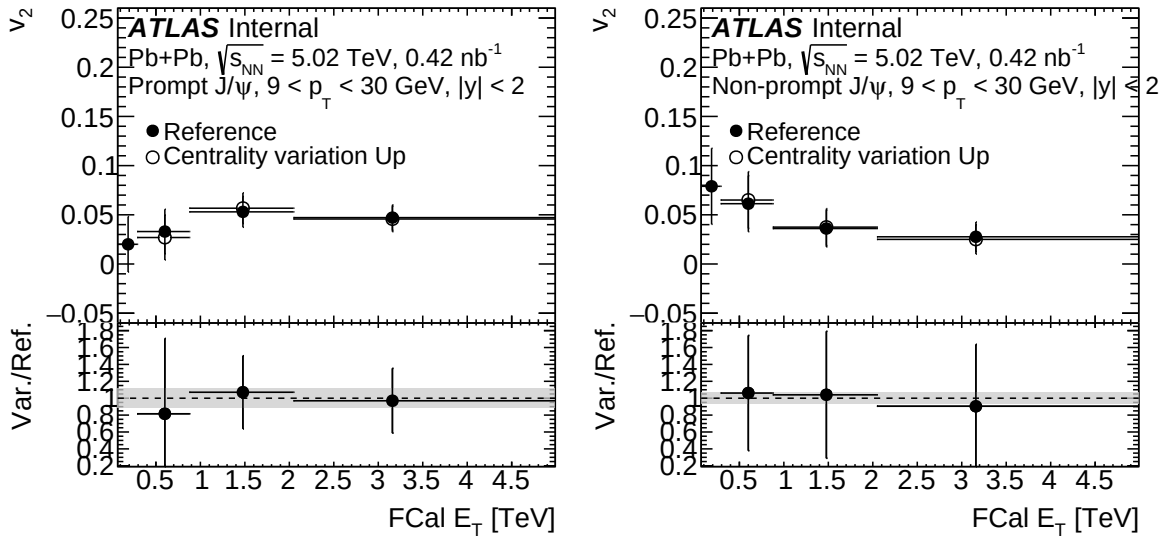

Figure 2.24.: Effect of varying the definition of the centrality classes on the centrality dependence of v_2 shown as a function of $\sum E_{\mathrm{T}}^{\mathrm{FCal}}$. The height of the shaded area is equal to the RMS of the difference between the nominal and varied value of v_2.

Related to the estimation of the event-plane

For the estimation of the event-plane angle, the calibration coefficients for the recentering of the flow vector are calculated using a narrower centrality interval (20–60%) instead of the full centrality range (0–60%). For the evaluation of $\delta\Psi_2$ the sum limit is changed to $k_{\max} = 4$. No significant differences are observed, so a systematic uncertainty is not assigned. For the event-plane resolution, the three-sub-event method [18] is used as an alternative to compute $\mathcal{R}$ for the event-plane angle calculated with FCal in $\eta < 0$ and $\eta > 0$ independently. By using the electromagnetic and hadronic calorimeters, the event-plane angle is calibrated and determined in two different sections with $0.5 < \eta < 2$ and $-1.5 < \eta < 0$ and compared with event-plane angle as measured in the FCal in $\eta < 0$ to obtain its resolution. For the resolution of the FCal in the opposite side ($\eta > 0$) a reflection of this selection is performed. Both the two-sub-event and three-sub-event methods give consistent results for collisions in the 0–60% centrality interval. To account for the different $\sum E_{\mathrm{T}}^{\mathrm{FCal}}$ distributions in minimum-bias and J/ψ triggered events, the difference between the resolutions computed in the two datasets is assigned as a systematic uncertainty and it is the dominant source of uncertainty. The total uncertainty for the average event-plane resolution adds a 4% correlated uncertainty to the measurements integrated over centrality, while for the centrality dependence each point has an approximate 1.5% uncertainty due to resolution. In the centrality interval considered in this analysis (0–60%), it is found that the uncertainty related to the centrality definition has no effect on the event-plane resolution.

Details of the systematic uncertainties related to the event-plane resolution are described in Section 2.5.1.

Related to the extraction of the signal

Variations to the PDF defined for the signal extraction are studied as well. Many modifications are considered, with the most important being: the release of the fixed parameters of the CB function [40], the substitution of the Gaussian + CB function by a single CB function, and variations of the Gaussian standard deviation and CB width scaling parameter; while for the time dependence a single exponential function is replaced by short and long lifetime exponential decays, and one Gaussian function instead of two is considered for time resolution. Among all of these variations the biggest contribution is the release of the parameters of the CB function, which contributes between 10% and 15% uncertainty for the p_{T} and rapidity dependence of v_2 and up to 20% for the centrality dependence. Deviations from the case of unpolarized J/ψ production are studied for different spin-alignment cases and are covered by a theoretical uncertainty of 3% in v_2 for prompt J/ψ and 4% for non-prompt J/ψ.

The breakdown of the variations of the PDF are shown in Figure 2.25. In Figure 2.26 the dominant systematic variation, the release of the CB α-parameter is shown for the results of prompt and non-prompt J/ψ v_2 as a function of p_{T}.

The choice of mass window used for the study is changed to analyze potential biases from the mass peak of the $\psi(2S)$. At high rapidity its width increases and the fit response for the background estimation changes. The mass window range is narrowed to $2.7 < m_{\mu\mu} < 3.4$ GeV

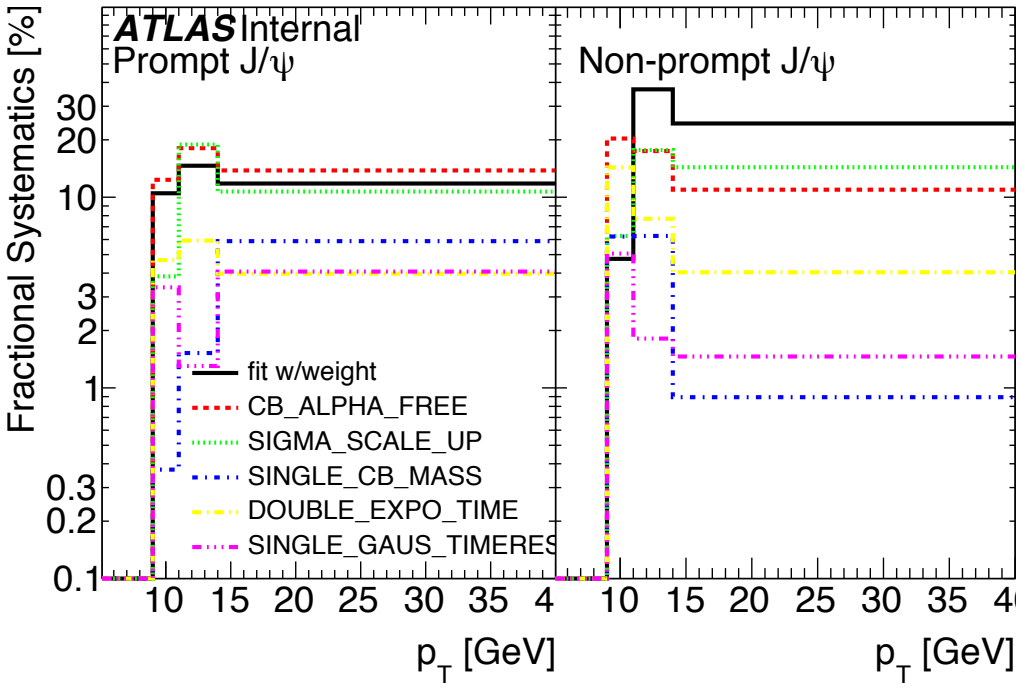

Figure 2.25.: Breakdown of the systematic uncertainties associated to variations in the signal PDF. The dominant source is the release of the α-parameter of the Crystal Ball function.

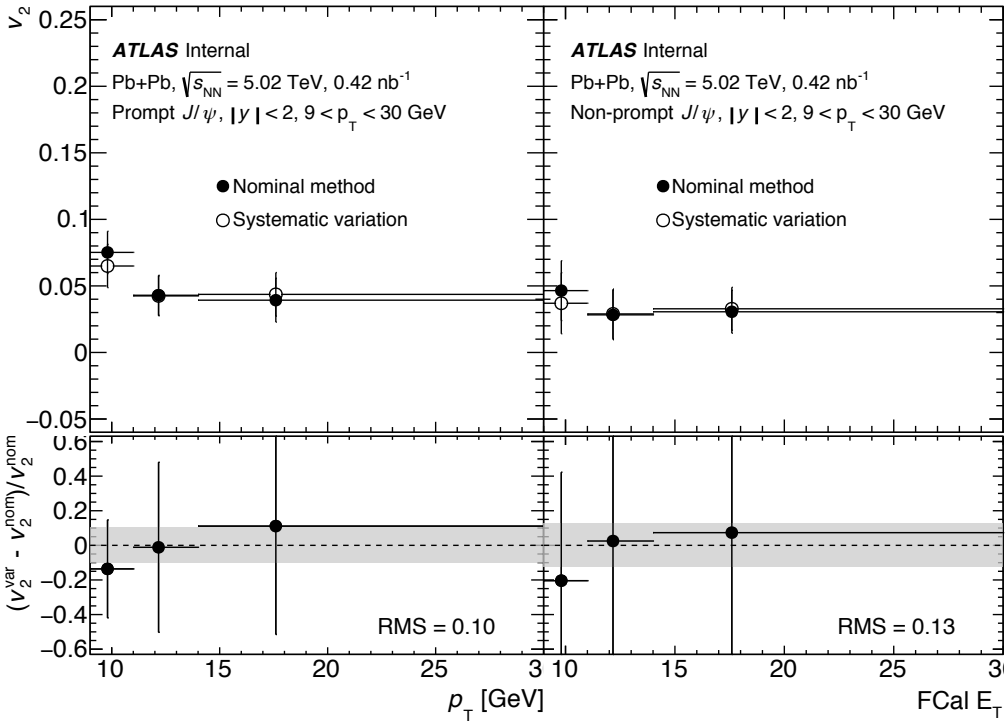

Figure 2.26.: Add a caption this figure please.

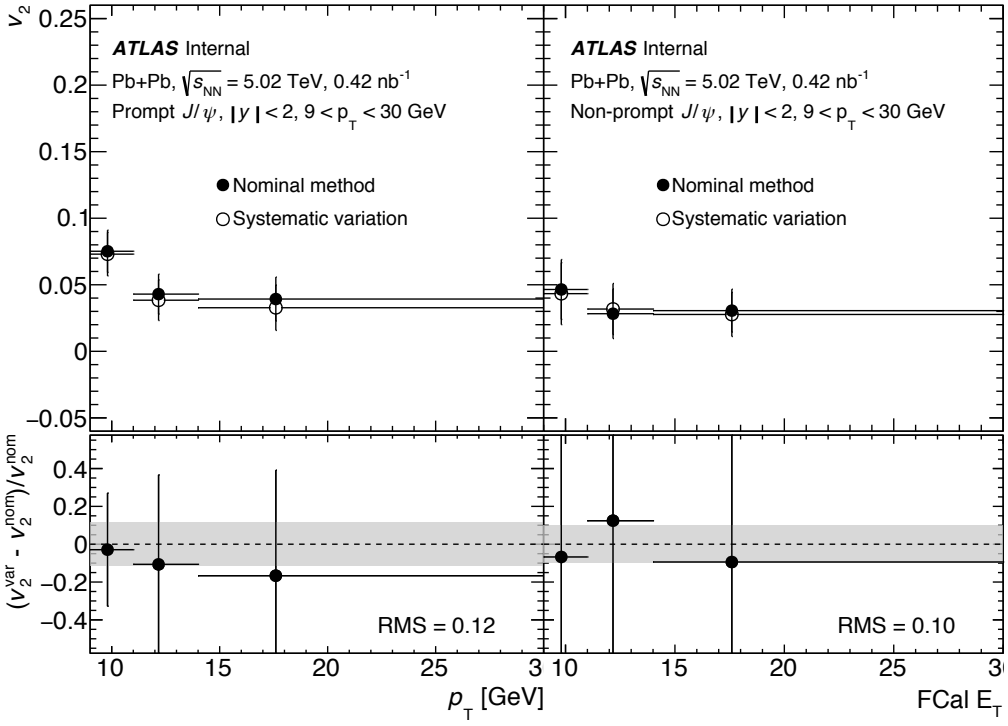

Figure 2.27.: Add a caption this figure please.

and its impact is between 5% and 10% for the p_T, rapidity and centrality dependencies. The impact of this variation is shown in Figure 2.27.

The correlation between the prompt and non-prompt yields is also studied. It is either doubled or neglected, and shows a minor impact of 1% for all presented results.

2.6. Results

Results of v_2 for prompt and non-prompt J/ψ are shown as a function of p_{T} in Figure 2.28, for three p_{T} intervals. The centroid of each p_{T} bin is determined by the average p_{T} of the muon pairs in the corresponding bin. The horizontal error bars correspond to the bin width reflecting the kinematic range of the measurement. The vertical error bars are the fit errors, which account for statistical uncertainties, and the shaded boxes are the systematic uncertainty. The data is consistent with a non-zero flow signal in the full kinematic range studied ($9 < p_{\mathrm{T}} < 30$ GeV) for both prompt and non-prompt J/ψ. Prompt J/ψ exhibit a decreasing trend with a maximum value of v_2 close to 0.09 that decreases by nearly a factor of two over the whole studied kinematic range. The results for non-prompt J/ψ indicate a non-zero value with limited statistical significance. These are consistent with a constant along p_{T} and compatible within uncertainties with the v_2 values of prompt J/ψ particularly at the highest p_{T}.

The rapidity dependence of v_2 is shown in Figure 2.29 and the centrality dependence in Figure 2.30 for both prompt and non-prompt J/ψ. Neither mode shows significant rapidity or centrality dependence. The prompt J/ψ v_2 is larger than the non-prompt, in agreement with the larger values observed in the p_{T} dependence integrated over rapidity and centrality. The measured value of v_2 for prompt J/ψ is the same in central collisions as in non-central collisions within uncertainties, in agreement with the observation of Ref. [6]. The case is similar with that of non-prompt J/ψ where no evident centrality dependence is observed within the uncertainties. This feature is in disagreement with the expected hydrodynamic behaviour for charm quarks and may manifest a transition at mid p_{T} where different effects influencing the J/ψ production are supposed to take place [7, 9, 8, 10, 11].

In Figure 2.31 the available results for inclusive J/ψ ($p_{\mathrm{T}} < 12$ GeV) from the ALICE experiment [5] and prompt J/ψ ($4 < p_{\mathrm{T}} < 30$ GeV) from the CMS experiment [6] are compared with the results obtained in this analysis for prompt J/ψ ($9 < p_{\mathrm{T}} < 30$ GeV) as a function of the J/ψ

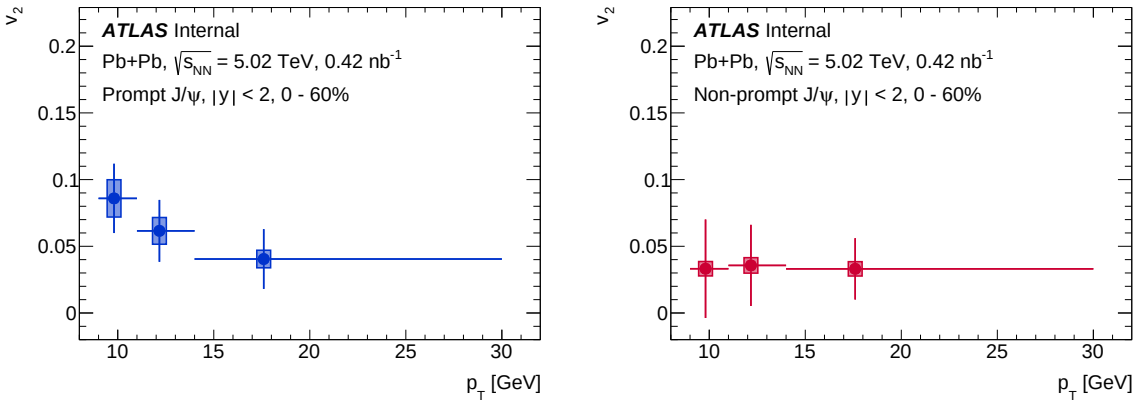

Figure 2.28.: Prompt J/ψ v_2 (left) and non-prompt J/ψ v_2 (right) as a function of transverse momentum for the rapidity interval $|y| < 2$ and centrality $0-60\%$. The statistical and systematic uncertainties are shown using error bars and boxes respectively. The horizontal error bars represent the kinematic range of the measurement for each bin.

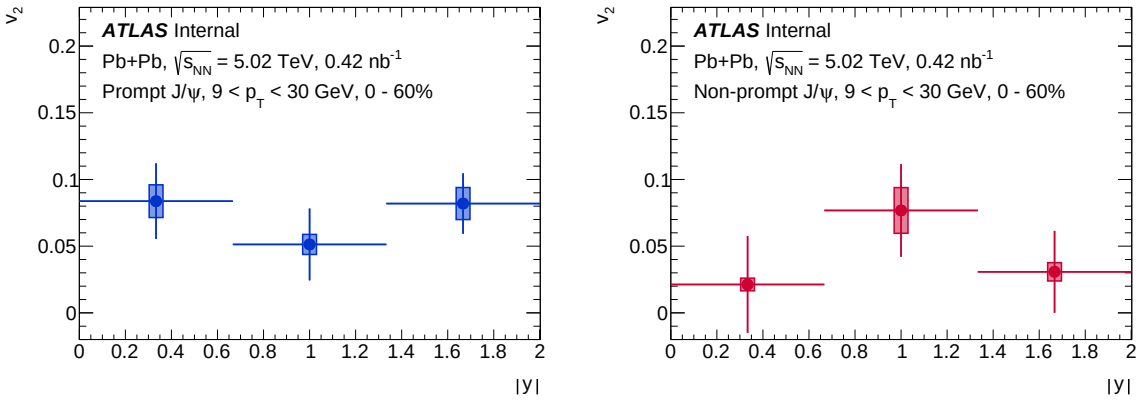

Figure 2.29.: Prompt J/ψ v_2 (left) and non-prompt J/ψ v_2 (right) as a function of rapidity for transverse momentum in the range $9 < p_{\mathrm{T}} < 30$ GeV and centrality $0 - 60\%$. The statistical and systematic uncertainties are shown using error bars and boxes respectively. The horizontal error bars represent the kinematic range of the measurement for each bin.

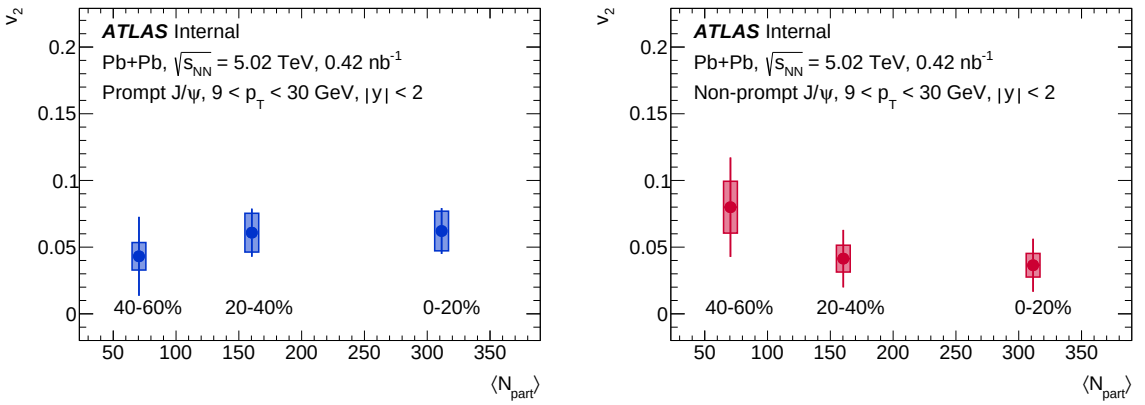

Figure 2.30.: Prompt J/ψ v_2 (left) and non-prompt J/ψ v_2 (right) as a function of average number of nucleons participating in the collision for transverse momentum in the range $9 < p_{\mathrm{T}} < 30$ GeV and rapidity $|y| < 2$. The statistical and systematic uncertainties are shown using error bars and boxes respectively.

candidate transverse momentum. Despite different rapidity selections, the magnitudes of the elliptic flow coefficients are compatible with each other. Two features can be observed: first, the hydrodynamic peak observed for charged particles at low p_{T} [13, 14, 15, 16, 17] is shifted to higher p_{T} values. This effect can be described qualitatively by thermalisation of charm quarks in the QGP medium with J/ψ regeneration playing a dominant role in the flow formation [7, 8]. The second feature is that v_2 has a substantial magnitude at high p_{T}. This can be connected with the suppression of J/ψ production due to mechanisms involving interactions with the medium such as absorption and melting [11] as shown in Figure 2.32, or energy loss [42, 43].

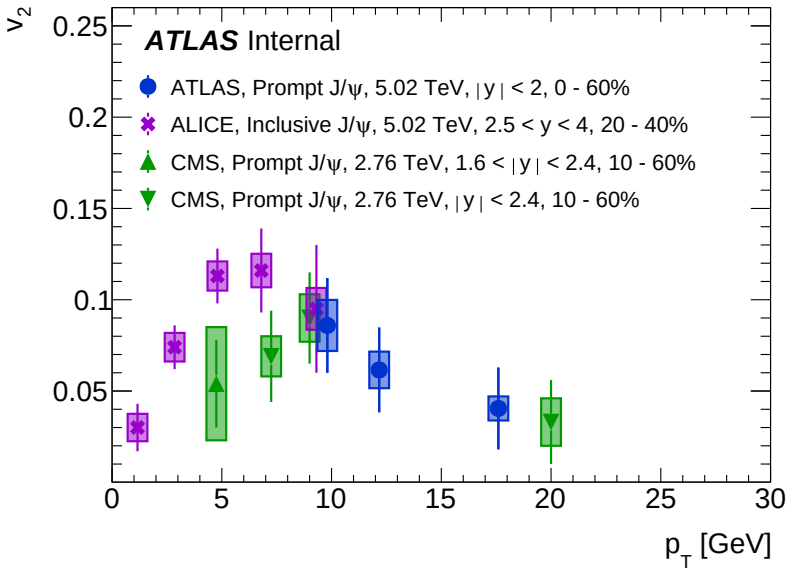

Figure 2.31.: Results for the v_2 as a function of the transverse momentum of prompt J/ψ as measured by ATLAS in this analysis compared with inclusive J/ψ at $p_{\mathrm{T}} < 12$ GeV, as measured by ALICE at 5.02 TeV [5], and prompt J/ψ at $4 < p_{\mathrm{T}} < 30$ GeV, by CMS at 2.76 TeV [6]. The statistical and systematic uncertainties are shown using error bars and boxes respectively.

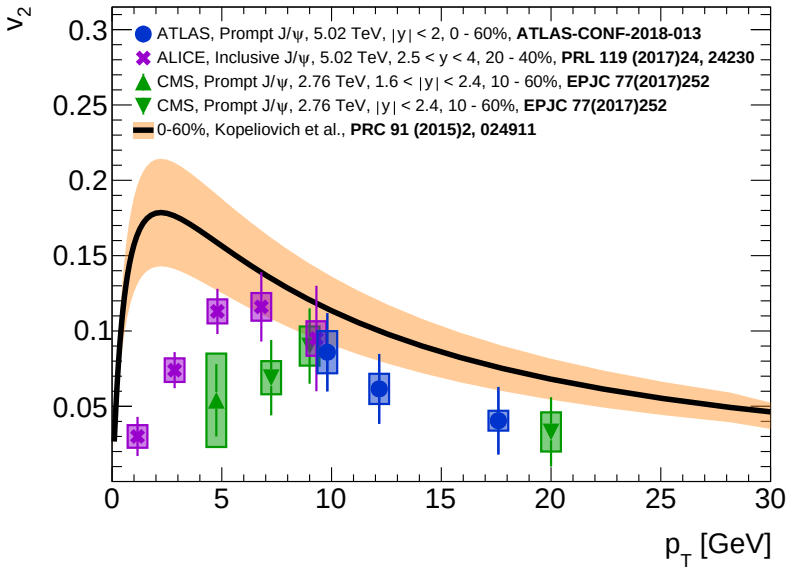

Figure 2.32.: Comparison of theoretical predictions and multiple measurements of inclusive ($p_{\mathrm{T}} < 12$) and prompt ($p_{\mathrm{T}} > 9$) J/ψ v_2 as a function of p_{T}.

2.7. Summary

This chapter presents measurements of the elliptic flow harmonic coefficients for J/ψ particles in the dimuon decay channel in Pb+Pb collisions recorded at $\sqrt{s_{\mathrm{NN}}} = 5.02$ TeV with the ATLAS detector. Results are presented for prompt and non-prompt J/ψ as a function of transverse momentum, rapidity and centrality. The measurement is performed in the kinematic range $9 < p_{\mathrm{T}} < 30$ GeV, $|y| < 2$, and $0 - 60\%$ centrality. The pseudo-proper time of the secondary vertex is used to separate the prompt and non-prompt components of J/ψ production and both yields are analysed simultaneously to properly assess the correlation between the two contributions.

A significant flow signal is observed for prompt J/ψ, which decreases with increasing p_{T}. At high p_{T} both prompt and non-prompt J/ψ v_2 are compatible within the uncertainties. This suggests a similar underlying process describing the propagation of sufficiently high p_{T} charm and bottom quarks through the medium. The idea is supported by the recent observation of the J/ψ yield suppression in Pb+Pb collisions [2, 3], where a similar suppression pattern for both prompt and non-prompt J/ψ is observed at high p_{T}.

References

[1] B. Z. Kopeliovich et al. "Novel scenario for production of heavy flavored mesons in heavy ion collisions". ***EPJ Web Conf.*** 164 (2017), p. 01018. DOI: 10.1051/epjconf/201716401018. arXiv: 1701.07121 [hep-ph].

[2] ATLAS Collaboration. "Prompt and non-prompt J/ψ and ψ(2S) suppression at high transverse momentum in 5.02 TeV Pb+Pb collisions with the ATLAS experiment" (2018). arXiv: 1805.04077 [nucl-ex].

[3] Jorge Andrés López López. "Measurement of charmonium production in heavy-ion collisions with the ATLAS detector". ***Nuclear Physics A*** 967 (2017), pp. 584–587. ISSN: 0375-9474. DOI: https://doi.org/10.1016/j.nuclphysa.2017.05.085. URL: http://www.sciencedirect.com/science/article/pii/S0375947417302105.

[4] ALICE Collaboration. "J/ψ Elliptic Flow in Pb-Pb Collisions at $\sqrt{s_{\mathrm{NN}}}$ = 2.76 TeV". ***Phys. Rev. Lett.*** 111 (2013), p. 162301. DOI: 10.1103/PhysRevLett.111.162301. arXiv: 1303.5880 [nucl-ex].

[5] ALICE Collaboration. "J/ψ Elliptic Flow in Pb-Pb Collisions at $\sqrt{s_{\mathrm{NN}}}$ = 5.02 TeV". ***Phys. Rev. Lett.*** 119.24 (2017), p. 242301. DOI: 10.1103/PhysRevLett.119.242301. arXiv: 1709.05260 [nucl-ex].

[6] CMS Collaboration. "Suppression and azimuthal anisotropy of prompt and nonprompt J/ψ production in PbPb collisions at $\sqrt{s_{\mathrm{NN}}}$ = 2.76 TeV". ***Eur. Phys. J. C*** 77.4 (2017), p. 252. DOI: 10.1140/epjc/s10052-017-4781-1. arXiv: 1610.00613 [nucl-ex].

[7] Kai Zhou et al. "Medium effects on charmonium production at ultrarelativistic energies available at the CERN Large Hadron Collider". ***Phys. Rev. C*** 89.5 (2014), p. 054911. DOI: 10.1103/PhysRevC.89.054911. arXiv: 1401.5845 [nucl-th].

[8] Li Yan, Pengfei Zhuang, and Nu Xu. "J/ψ Production in Quark-Gluon Plasma". ***Phys. Rev. Lett.*** 97 (2006), p. 232301. DOI: 10.1103/PhysRevLett.97.232301. arXiv: nucl-th/0608010 [nucl-th].

[9] Jiechen Xu, Jinfeng Liao, and Miklos Gyulassy. "Bridging Soft-Hard Transport Properties of Quark-Gluon Plasmas with CUJET3.0". ***JHEP*** 02 (2016), p. 169. DOI: 10.1007/JHEP02(2016)169. arXiv: 1508.00552 [hep-ph].

[10] E. G. Ferreiro. "Charmonium dissociation and recombination at LHC: Revisiting comovers". ***Phys. Lett. B*** 731 (2014), pp. 57–63. DOI: 10.1016/j.physletb.2014.02.011. arXiv: 1210.3209 [hep-ph].

[11] B. Z. Kopeliovich et al. "Survival of charmonia in a hot environment". ***Phys. Rev. C*** 91.2 (2015), p. 024911. DOI: 10.1103/PhysRevC.91.024911. arXiv: 1409.5147 [hep-ph].

[12] Hanlin Li, Zi-Wei Lin, and Fuqiang Wang. "Charm quarks are more hydrodynamic than light quarks in elliptic flow" (2018). arXiv: 1804.02681 [hep-ph].

[13] ATLAS Collaboration. "Measurement of the azimuthal anisotropy for charged particle production in $\sqrt{s_{\mathrm{NN}}}$ = 2.76 TeV lead–lead collisions with the ATLAS detector". ***Phys. Rev. C*** 86 (2012), p. 014907. DOI: 10.1103/PhysRevC.86.014907. arXiv: 1203.3087 [hep-ex].

[14] ATLAS Collaboration. "Measurement of the centrality and pseudorapidity dependence of the integrated elliptic flow in lead–lead collisions at $\sqrt{s_{\mathrm{NN}}}$ = 2.76 TeV with the ATLAS detector". ***Eur. Phys. J. C*** 74 (2014), p. 2982. DOI: 10.1140/epjc/s10052-014-2982-4. arXiv: 1405.3936 [hep-ex].

[15] CMS Collaboration. "Azimuthal anisotropy of charged particles at high transverse momenta in PbPb collisions at $\sqrt{s_{\mathrm{NN}}}$ = 2.76 TeV". ***Phys. Rev. Lett.*** 109 (2012), p. 022301. DOI: 10.1103/PhysRevLett.109.022301. arXiv: 1204.1850 [hep-ex].

[16] ALICE Collaboration. "Anisotropic flow of charged hadrons, pions and (anti-)protons measured at high transverse momentum in Pb-Pb collisions at $\sqrt{s_{\mathrm{NN}}}$=2.76 TeV". ***Phys. Lett. B*** 719 (2013), pp. 18–28. DOI: 10.1016/j.physletb.2012.12.066. arXiv: 1205.5761 [nucl-ex].

[17] ALICE Collaboration. "Anisotropic flow of charged particles in Pb-Pb collisions at $\sqrt{s_{\mathrm{NN}}}$ = 5.02 TeV". ***Phys. Rev. Lett.*** 116.13 (2016), p. 132302. DOI: 10.1103/PhysRevLett.116.132302. arXiv: 1602.01119 [nucl-ex].

[18] Arthur M. Poskanzer and S. A. Voloshin. "Methods for analyzing anisotropic flow in relativistic nuclear collisions". ***Phys. Rev. C*** 58 (1998), pp. 1671–1678. DOI: 10.1103/PhysRevC.58.1671. arXiv: nucl-ex/9805001 [nucl-ex].

[19] ATLAS Collaboration. "Measurement of the Azimuthal Angle Dependence of Inclusive Jet Yields in Pb+Pb Collisions at $\sqrt{s_{\mathrm{NN}}}$ = 2.76 TeV with the ATLAS detector". ***Phys. Rev. Lett.*** 111 (2013), p. 152301. DOI: 10.1103/PhysRevLett.111.152301. arXiv: 1306.6469 [hep-ex].

[20] CMS Collaboration. "Measurement of prompt D^0 meson azimuthal anisotropy in Pb-Pb collisions at $\sqrt{s_{\mathrm{NN}}}$ = 5.02 TeV". ***Phys. Rev. Lett.*** 120.20 (2018), p. 202301. DOI: 10.1103/PhysRevLett.120.202301. arXiv: 1708.03497 [nucl-ex].

[21] ATLAS Collaboration. "The ATLAS Experiment at the CERN Large Hadron Collider". ***JINST*** 3 (2008), S08003. DOI: 10.1088/1748-0221/3/08/S08003.

[22] ATLAS Collaboration. "Performance of the ATLAS Trigger System in 2015". ***Eur. Phys. J. C*** 77 (2017), p. 317. DOI: 10.1140/epjc/s10052-017-4852-3. arXiv: 1611.09661 [hep-ex].

[23] ATLAS Collaboration. "Muon reconstruction performance of the ATLAS detector in proton–proton collision data at $\sqrt{s}$ = 13 TeV". ***Eur. Phys. J. C*** 76 (2016), p. 292. DOI: 10.1140/epjc/s10052-016-4120-y. arXiv: 1603.05598 [hep-ex].

[24] Torbjörn Sjöstrand et al. "An Introduction to PYTHIA 8.2". ***Comput. Phys. Commun.*** 191 (2015), pp. 159–177. DOI: 10.1016/j.cpc.2015.01.024. arXiv: 1410.3012 [hep-ph].

[25] Elisabetta Barberio, Bob van Eijk, and Zbigniew Was. "PHOTOS: A Universal Monte Carlo for QED radiative corrections in decays". ***Comput. Phys. Commun.*** 66 (1991), pp. 115–128. DOI: 10.1016/0010-4655(91)90012-A.

[26] ATLAS Collaboration. ***ATLAS Pythia 8 tunes to 7 TeV data***. ATL-PHYS-PUB-2014-021. 2014. URL: https://cdsweb.cern.ch/record/1966419.

[27] J. Pumplin et al. "New generation of parton distributions with uncertainties from global QCD analysis". ***JHEP*** 07 (2002), p. 012. DOI: 10.1088/1126-6708/2002/07/012. arXiv: hep-ph/0201195 [hep-ph].

[28] ATLAS Collaboration. "The ATLAS Simulation Infrastructure". ***Eur. Phys. J. C*** 70 (2010), p. 823. DOI: 10.1140/epjc/s10052-010-1429-9. arXiv: 1005.4568 [physics.ins-det].

[29] S. Agostinelli et al. "Geant4 – a simulation toolkit". ***Nucl. Instr. Meth. Phys. Res. A*** 506.3 (2003), pp. 250–303. DOI: https://doi.org/10.1016/S0168-9002(03)01368-8.

[30] Miklos Gyulassy and Xin-Nian Wang. "HIJING 1.0: A Monte Carlo program for parton and particle production in high-energy hadronic and nuclear collisions". ***Comput. Phys. Commun.*** 83 (1994), p. 307. DOI: 10.1016/0010-4655(94)90057-4. arXiv: nucl-th/9502021 [nucl-th].

[31] Michael L. Miller et al. "Glauber modeling in high energy nuclear collisions". ***Ann. Rev. Nucl. Part. Sci.*** 57 (2007), pp. 205–243. DOI: 10.1146/annurev.nucl.57.090506.123020. arXiv: nucl-ex/0701025 [nucl-ex].

[32] B. Alver et al. "The PHOBOS Glauber Monte Carlo" (2008). arXiv: 0805.4411 [nucl-ex].

[33] ATLAS Collaboration. "Study of photon-jet momentum correlations in Pb+Pb and pp collisions at $\sqrt{s_{\mathrm{NN}}}$ = 5.02 TeV with ATLAS". ATLAS-CONF-2016-110 (Sept. 2016). URL: https://cds.cern.ch/record/2220772.

[34] ATLAS Collaboration. "Measurement of event-plane correlations in $\sqrt{s_{\mathrm{NN}}}$ = 2.76 TeV lead–lead collisions with the ATLAS detector". ***Phys. Rev. C*** 90 (2014), p. 024905. DOI: 10.1103/PhysRevC.90.024905. arXiv: 1403.0489 [hep-ex].

[35] Olaf Behnke et al. ***Data analysis in high energy physics: a practical guide to statistical methods***. Weinheim: Wiley-VCH, 2013. DOI: 10.1002/9783527653416.

[36] LHCb Collaboration. "Measurement of J/ψ polarization in pp collisions at $\sqrt{s}$ = 7 TeV". ***Eur. Phys. J. C*** 73.11 (2013), p. 2631. DOI: 10.1140/epjc/s10052-013-2631-3. arXiv: 1307.6379 [hep-ex].

[37] ALICE Collaboration. "J/ψ polarization in pp collisions at $\sqrt{s}$ = 7 TeV". ***Phys. Rev. Lett.*** 108 (2012), p. 082001. DOI: 10.1103/PhysRevLett.108.082001. arXiv: 1111.1630 [hep-ex].

[38] CMS Collaboration. "Measurement of the prompt J/ψ and ψ(2S) polarizations in pp collisions at $\sqrt{s}$ = 7 TeV". ***Phys. Lett. B*** 727 (2013), pp. 381–402. DOI: 10.1016/j.physletb.2013.10.055. arXiv: 1307.6070 [hep-ex].

[39] C. Patrignani et al. "Review of Particle Physics". ***Chin. Phys. C*** 40.10 (2016), p. 100001. DOI: 10.1088/1674-1137/40/10/100001.

[40] M. Oreglia. "A Study of the Reactions $\psi' \to \gamma\gamma\psi$". ***Ph.D. Thesis, Stanford University, SLAC-236*** (1980).

[41] T. Skwarnicki. "A study of the radiative CASCADE transitions between the Υ' and Υ resonances". ***Ph.D Thesis, DESY F31-86-02*** (1986).

[42] François Arleo. "Quenching of Hadron Spectra in Heavy Ion Collisions at the LHC". ***Phys. Rev. Lett.*** 119.6 (2017), p. 062302. DOI: 10.1103/PhysRevLett.119.062302. arXiv: 1703.10852 [hep-ph].

[43] Martin Spousta. "On similarity of jet quenching and charmonia suppression". ***Phys. Lett. B*** 767 (2017), pp. 10–15. DOI: 10.1016/j.physletb.2017.01.041. arXiv: 1606.00903 [hep-ph].

Chapter 3.

Final Outlook

Two different analysis were presented in this doctoral dissertation. First, the first time extraction of the production length and transport coefficient from semi-inclusive deep inelastic scattering data. Second, the measurement of the J/ψ elliptic flow coefficient in Pb+Pb collisions using the ATLAS detector at the LHC.

Both analyses are based in different lines of research, but both are probing the propagation of quarks in medium. In each case the nuclear medium works as a tool to test the propagation quarks through the space, filled with nucleons in the first case and deconfined colored matter in the second case. The nuclear medium modifies the production of final state particles, which are detectable, and this allows to test fundamental QCD properties: the propagation of color charges and its neutralization, and finally the reinforcement of color confinement.

For the first time, the color lifetime or production length has been extracted for positive charged pions produced in electron-nucleus deep inelastic scattering. The measurement of the elliptic flow of prompt and non-prompt J/ψ has been performed, giving insights into the propagation of c- and b-quarks inside the QGP in a novel p_{T} range which complements previous measurements. The potential links to color propagation for the former study are evident, while for the latter, the connections are less obvious but unavoidable since J/ψ v_2 can be understood as an effect of path length dependent effects.

Appendix A.

Supporting Notes for the Space-Time Analysis of siDIS

A.1. Derivation of production length formula

We start from the proton and photon 4-vectors:

$$p = (M_P, 0, 0, 0) \tag{A.1}$$
$$q = (E_\gamma, 0, 0, p_z) \tag{A.2}$$

Imposing that $q^2 = -Q^2$, we can write:

$$p_z^2 = E_\gamma^2 + Q^2 \tag{A.3}$$

We will choose the positive solution of the square root of p_z, and assume that $Q^2/E_\gamma^2 << 1$:

$$p_z = \sqrt{E_\gamma^2 + Q^2} = E_\gamma \sqrt{1 + Q^2/E_\gamma^2} \approx E_\gamma \tag{A.4}$$

Light cone cordinates:

$$p^\pm = E \pm p_z \tag{A.5}$$

The total amount of momenta is:

$$\begin{aligned} (p_P^+ + q_\gamma^+) &= p^+ = M_P + E_\gamma + (0 + E_\gamma) = M_P + 2E_\gamma \\ (p_P^- + q_\gamma^-) &= p^- = M_P + E_\gamma - (0 + E_\gamma) = M_P \end{aligned}$$

We will use this later:

$$p^+ = M_P + 2E_\gamma \tag{A.6}$$
$$p^- = M_P \tag{A.7}$$

Something I found useful, but that won't be used here, related to the transverse mass is:

$$m_\perp^2 = m^2 + p_\perp^2 = E^2 - p_z^2 = p^+ p^- \tag{A.8}$$

The following comes from assuming Torbjörn Sjöstrand's notes:

$$p_h^+ = z p^+ \tag{A.9}$$

$$p_h^- = \frac{m_\perp^2}{z p^+} \tag{A.10}$$

And:

$$p_v^+ = (1-z) p^+ \tag{A.11}$$

$$p_v^- = \frac{m_\perp^2}{z p^+} \tag{A.12}$$

The factor κ is the ratio of light-cone momentum to light-cone position:

$$p_v^\pm = \kappa x_v^\pm \tag{A.13}$$

where $x^\pm = \tau \pm l$ is the light-cone position [a]. Provided that we can write:

$$p_v^+ = \kappa(\tau + l) = (1-z) p^+$$

$$p_v^- = \kappa(\tau - l) = \frac{m_\perp^2}{z p^+}$$

Where we have used Eqs. (A.11,A.12,A.13). We end with the following system of equations for the production time τ and length l:

$$\kappa(\tau + l) = (1-z) p^+ \tag{A.14}$$

$$\kappa(\tau - l) = \frac{m_\perp^2}{z p^+} \tag{A.15}$$

Adding and subtracting this equations gives the equations we already know:

$$2\kappa\tau = (1-z) p^+ + \frac{m_\perp^2}{z p^+} \tag{A.16}$$

$$2\kappa l = (1-z) p^+ - \frac{m_\perp^2}{z p^+} \tag{A.17}$$

$$\tag{A.18}$$

[a] I have used $x^\mu = (\tau, 0, 0, l)$

We also have the energy of the hadron expressed in terms of other quantities:

$$E_h = \frac{1}{2}\left(zp^+ + \frac{m_\perp^2}{zp^+}\right) \tag{A.19}$$

This comes from the fact that we can express the energy from the positive and negative components of light cone momenta:

$$E = \frac{1}{2}(p^+ + p^-)$$

Now let's solve. From Eq. (A.19) we can write:

$$\frac{m_\perp^2}{zp^+} = 2E_h - zp^+ \tag{A.20}$$

Plug this into Eq. (A.17) and we have:

$$\begin{aligned} 2\kappa l &= (1-z)p^+ - (2E_h - zp^+) \\ 2\kappa l &= (1-z)p^+ - 2E_h + zp^+ \\ 2\kappa l &= p^+ - 2E_h \end{aligned}$$

Make use Eq. (A.6) and to substitute p^+:

$$\begin{aligned} 2\kappa l &= (M_P + 2E_\gamma) - 2E_h \\ \kappa l &= \frac{M_P}{2} + E_\gamma - E_h \\ \kappa l &= \frac{M_P}{2} + E_\gamma - E_\gamma\frac{E_h}{E_\gamma} \\ \kappa l &= \frac{M_P}{2} + E_\gamma\left(1 - \frac{E_h}{E_\gamma}\right) \end{aligned}$$

Changing the same of the variables to $E_\gamma = \nu$ and $z_h = E_h/\nu$. We finally have:

$$\kappa l = \frac{M_P}{2} + \nu(1 - z_h) \tag{A.21}$$

If we do not want to do the very first approximation we have:

$$\kappa l = \frac{M_P}{2} + \nu(1 - z_h) + \frac{1}{2}\nu\left(\sqrt{1 + \frac{Q^2}{\nu^2}} - 1\right) \tag{A.22}$$

A.2. Model uncertainties

The model computes the transverse momentum broadening and the multiplicity ratio, defined as:

$$P_{\mathrm{T}}^2 = \left\langle q_0 \int_{z_0}^{u(L)} \rho(x_0, y_0, z)\mathrm{d}z \right\rangle_{\mathrm{MC}} \tag{A.23}$$

$$R_{\mathrm{M}} = \left\langle \exp\left(-\sigma_{\mathrm{hn}} \int_{u(L)}^{r_A} \rho(x_0, y_0, z)\mathrm{d}z\right) \right\rangle_{\mathrm{MC}} \tag{A.24}$$

Where MC stands for Monte Carlo average, and the free parameters of the model are the transport coefficient density q_0, the production length L, and the *pre*hadron-nucleon cross-section σ_{hn}. The integral limit $u(L)$ is defined as:

$$u(L) = (z_0 + L)\Theta(R^* - (z_0 + L)) + R^*\Theta(z_0 + L - R) \tag{A.25}$$

Where:

$$R^* = \sqrt{R^2 - x_0^2 - y_0^2} \tag{A.26}$$

The MC average is computed by throwing an interaction point (x_0, y_0, z_0) within a sphere is radius r_A, using a uniform distribution weighted by the nuclear density at that point, $\rho(x_0, y_0, z_0)$. The parameters are adjusted to data by minimizing the combined sum of squares:

$$S^2(q_0, L, \sigma) = \sum_{i=1}^{n} \left(\frac{\Delta\langle p_{\mathrm{T}}^2\rangle_i - P_{\mathrm{T}}^2(q_0, L)}{\epsilon_i} \right)^2 + \sum_{i=1}^{n} \left(\frac{R_{\mathrm{M}i} - R_{\mathrm{M}}(\sigma_{\mathrm{hn}}, L)}{\epsilon_i} \right)^2 \tag{A.27}$$

The integrals defined in Eq. A.23 and A.24 are computed using standard numerical integration routines available in `GSL`, and the minimization of Eq. A.27 is performed using the `Minuit` framework. The error analysis is performed and provided as output of the minimization procedure for the set free parameters, including their uncertainties and correlations.
As the form of S^2 does not depends on explicitely on P_{T}^2 or R_M, the uncertainties on this quantities is not available as direct output from `Miniut` and must be included as part of `ColorFitter`. The derivation of those uncertainties is presented in the next section.

It follows that for any non-linear differentiable function $f(a, b)$, its variance is approximated by:

$$\sigma_f^2 = \left|\frac{\partial f}{\partial a}\right|^2 \sigma_a^2 + \left|\frac{\partial f}{\partial b}\right|^2 \sigma_b^2 + 2\frac{\partial f}{\partial a}\frac{\partial f}{\partial b}\sigma_{a,b} \tag{A.28}$$

Hence, the variance of the momentum broadening will be given by:

$$\sigma_{P_{\mathrm{T}}^2}^2 = \left|\frac{\partial P_{\mathrm{T}}^2}{\partial q_0}\right|^2 \sigma_{q_0}^2 + \left|\frac{\partial P_{\mathrm{T}}^2}{\partial L}\right|^2 \sigma_L^2 + 2\frac{\partial P_{\mathrm{T}}^2}{\partial q_0}\frac{\partial P_{\mathrm{T}}^2}{\partial L}\sigma_{q_0,L} \tag{A.29}$$

And for the multiplicity ratio:

$$\sigma^2_{R_\mathrm{M}} = \left|\frac{\partial R_\mathrm{M}}{\partial \sigma_\mathrm{hn}}\right|^2 \sigma^2_{\sigma_\mathrm{hn}} + \left|\frac{\partial R_\mathrm{M}}{\partial L}\right|^2 \sigma^2_L + 2\frac{\partial R_\mathrm{M}}{\partial \sigma_\mathrm{hn}}\frac{\partial P^2_\mathrm{T}}{\partial L}\sigma_{\sigma_{\sigma_\mathrm{hn}},L} \tag{A.30}$$

Using the fact that:

$$\frac{\partial}{\partial x}\int_{g(x)}^{f(x)} h(t)\mathrm{d}t = g(f(x))f'(x) - h(g(x))g'(x) \tag{A.31}$$

The derivates are:

$$\frac{\partial P^2_\mathrm{T}}{\partial q_0} = \left\langle \int_{z_0}^{u(L)} \rho(x_0, y_0, z)\mathrm{d}z \right\rangle_\mathrm{MC} = \frac{P^2_\mathrm{T}}{q_0} \tag{A.32}$$

$$\frac{\partial P^2_\mathrm{T}}{\partial L} = \left\langle q_0 \rho(x_0, y_0, z_0 + L) \right\rangle_\mathrm{MC} \quad , (z_0 + L) < R^* \tag{A.33}$$

$$\frac{\partial R_\mathrm{M}}{\partial \sigma_\mathrm{hn}} = -\left\langle \exp\left(-\sigma_\mathrm{hn}\int_{u(L)}^{R^*} \rho(x_0, y_0, z)\mathrm{d}z\right)\int_{u(L)}^{R^*} \rho(x_0, y_0, z)\mathrm{d}z \right\rangle_\mathrm{MC} \tag{A.34}$$

$$\frac{\partial R_\mathrm{M}}{\partial L} = \left\langle \exp\left(-\sigma_\mathrm{hn}\int_{u(L)}^{R^*} \rho(x_0, y_0, z)\mathrm{d}z\right)\sigma_\mathrm{hn}\rho(x_0, y_0, z_0 + L) \right\rangle_\mathrm{MC} \quad , (z_0 + L) < R^* \tag{A.35}$$

So, we have:

$$\sigma^2_{P^2_\mathrm{T}} = \left(\frac{P^2_\mathrm{T}}{q_0}\right)^2 \sigma^2_{q_0} + {q_0}^2 \left\langle \rho(x_0, y_0, z_0 + L) \right\rangle^2_\mathrm{MC} \sigma^2_L + 2P^2_\mathrm{T} \left\langle \rho(x_0, y_0, z_0 + L) \right\rangle_\mathrm{MC} \sigma_{q_0,L} \tag{A.36}$$

Appendix B.

Supporting Notes for the Measurement of the J/ψ Elliptic Flow

B.1. Fourier expansion of the particle yield

The general Fourier expansion of the azimuthal distribution of particles is:

$$2\pi\frac{\mathrm{d}N}{\mathrm{d}\phi} = 1 + \sum_{n=1}^{\infty} 2v_n \cos[n(\phi - \Psi_n)] \tag{B.1}$$

Show that:

$$\langle \cos[n(\phi - \Psi_n)] \rangle \quad = \quad v_n \tag{B.2}$$

B.2. Signal fit parameters

Parameter	Descrition	State
`Bkgd_Exp_MisID`	Background of misidentified candidates	Free
`Bkgd_Exp_NonPrompt`	Background of non-prompt candidates	Free
`Bkgd_Exp_Prompt`	Background of prompt candidates	Free
`Life_NP_1S`	Tail of the decay time signal candidates	Free
`Life_NP_B1`	tail of the decay time of background candidates	Free
`Life_NP_MisID`	Double-tail of the decay time of misidentified candidates	Free
`Mass_Mean_1S`	Mean of the mass of the signal candidates, for the CB and G	Fixed
`Mass_Sigma_1S_G`	Width of the mass of the signal candidates for the G	Fixed
`N_1S`	Total number of signal candidates	Free
`N_B`	Total number of background candidates	Free
`Tau_ResoFrac`	Width fraction of the decay time resolutions	Fixed
`Tau_Sigma1`	Width of the decay time resolution	Free
`f_NP_1S`	Fraction of the signal that is non-prompt	Free
`f_NP_B`	Fraction of the prompt and non-prompt background	Free
`f_NP_B_MisID`	Fraction of the two non-prompt backgrounds	Free

Table B.1.: List of the parameters of the mass and decay-time fitting procedure for the signal extraction. Those parameters which is fixed are determined in a first fit-step using the whole slice of data for given p_{T}, rapidity or centrality interval; the free parameters are determined in a second fit-step for each azimuthal bin.